Ultrafast Control of the Dynamics of Diatomic Molecules

Daniel Walter Pinkham

B.S., University of Virginia, 2002

A Dissertation presented to the Graduate Faculty of the University of Virginia in Candidacy for the Degree of Doctor of Philosophy

Department of Physics

University of Virginia

May, 2008

In loving memory of Timothy H. Pinkham,

a brilliant scholar and a wonderful father

Abstract

Samples of gaseous diatomic molecules are excited into rotational wavepackets by ultrashort laser pulses, and the resultant dynamics are probed in the time-domain. The preparation of non-isotropic rotational distributions of molecules in field-free conditions enables a number of strong-field physics experiments to be performed. This process, known as transient alignment, serves as the central tool for most of the work described here. First, the angle-dependent ionization rates are measured for samples of room-temperature CO. Next, the polarizability anisotropy $\Delta\alpha$ - a quantity indicating how easily the electronic cloud is distorted by an applied electric field - is extracted for HBr molecules at $\sim$30 K, by observing the transient alignment efficiency in comparison to that of a reference molecule, N_2. In a follow-up experiment, a feedback-optimized algorithm is used to improve the transient alignment process by phase-shaping the pump laser pulses, and principal control analysis is used to search for pulse-shaping parameter "knobs" that most effectively control the alignment process. We observe that a rigid-rotor model with a constant $\Delta\alpha$ is sufficient to describe the alignment dynamics. In the final section, we explore asymmetric dissociation of multiply charged ions produced by intense laser ionization in a 2-color field. By combining 800 nm and 400 nm laser pulses we produce an oscillating electric field with a controllable, periodic "up-down" asymmetry in the lab frame. This asymmetry can be used to control the relative yields of ion fragments ejected in different directions. In contrast to previous studies with 2-color fields, we utilize an independent, symmetric, ionization pulse to determine that the observed dissociation is the result of an induced directionality in the field-dressed molecules rather than transient orientation of the molecule. This asymmetry is found to be an effect of enhanced molecular ionization at a critical internuclear distance ($R_C > R_{eq}$). This fact is further illustrated by our observation of an asymmetry in the dissociation of symmetric molecules (e.g. $N_2^{3+} \rightarrow N^{2+} + N^+$). We conclude with an analysis of transient molecular orientation in 2-color fields and describe preliminary attempts to observe it.

Contents

List of Figures

List of Tables

Acknowledgements

I would first like to thank my family for all the support they've shown me in the past 27 years. I would not be here without all their encouragement. Thank you, Mom and Dad, for giving me the best upbringing I could imagine. I am so fortunate to have grown up in your household. Becky, I will be joining you in the ranks of the family doctors, even if I will be a different sort of doctor. Good luck finishing up your residency. I am excited to see where your career will take you.

So much of my progress has been possible with the constant encouragement of my girlfiend (and future wife) Alden Purdy. You've put up with all my idiosyncrasies, and that alone deserves a medal. Thank you for always being cheerful and supportive through both the easy and tough times. I have been blessed to know you, and I am so thankful that our paths first converged on the Rotunda steps 3 years ago. I look forward to spending the rest of my life with you.

I wish the best of luck to all my physics classmates in completing their degrees. It was a fun two years together in the graduate office. Ed and Danny, congratulations on finishing your degrees this past year.

Thank you, Chris Floyd, for being such a terrific resource. You've removed an entire source of stress from my graduate life by providing efficient service with all of my requests, even with the difficult companies. Shawn and Brian, thank you for answering all of my hardware and software computing questions. A big thanks also goes out to Suzie, Tammie, Dawn, Pam, Beth, Faye, Gwen and everyone else in the accounting office and main departmental office. The atmosphere is always pleasant when I stop by over there.

Thank you Supriya, Jason, and Santosh for helping me get started with labwork as an undergraduate. Thank you Michael, Merrick, Yehudi, Hyun, Pam, Kevin, Kurt, Gordon, Tish, Greg, Kristy, Jeremy and everyone else who helped me out while in the Chemistry lab. I would also like to express my thanks to Dr. Brooks Pate and his lab for letting me frequently borrow and use their tools, electronics, and optics. Tearing down the wall between our labs was a good idea. Thank you, Eric, for all your advice on getting the detector and electronics properly set-up. You were a great source of information for Brett and me, and I am sure all your future graduate students will think similarly. Russell, it was fun having you over in Chemistry for a year, and I was glad to learn a little about cricket and other British things. Congratulations to you and Katherine on your baby Hannah. I also want to thank Thibault, Mary, and Xiangdong for helping me out while I worked over in the physics lab. I finally got accustomed to working with the blinking 15

Hz after being spoiled with 1 kHz light for so many years!

Brett, it has been a pleasure working in the laser lab with you over these past years. You have helped me out frequently with innumerable lab issues. I wish you the best of luck finishing up your work here, and in getting situated back on the west coast with Nicole.

Kelsie, thanks for being such an energetic helper in the lab, and good luck on developing your first research project. You have some cool lasers at your disposal, and I'm sure there are many possible research pathways available to you in the Chemistry lab.

None of this work could have been accomplished without the guidance of my advisor, Dr. Robert Jones. Thank you Dr. Jones, for providing me so much support throughout the years. The uniform and energetic interest you show towards all your grad students' projects is very encouraging, and you have helped us learn to accept only the most convincing experimental results. It was a tremendous opportunity to work with so many laser systems, and I hope that some of my results prove to be useful to you and your future graduate students.

This research has been supported by the DOE Basic Energy Sciences, UVA FEST, and NSF.

Chapter 1

Introduction

1.1 Motivations

Ultrafast laser technology has had a profound impact on experimental atomic physics. Laser pulses with durations less than a few hundred femtoseconds (fsec) have enabled researchers in the last decade to explore dynamics on the time scale of molecular and electronic motion. The intensities achieved by focused ultrafast pulses are comparable to electronic binding energies and can remove electrons from tightly-bound orbitals, such as the Helium $1s$ shell. Additionally, by appropriate tuning of the pulse's temporal and spectral profiles, atomic and molecular targets can be selectively prepared into desired electronic, vibrational, or rotational states. We examine the interaction of intense non-resonant light fields with a variety of diatomic molecules in order to probe their inherent properties. There are numerous uncertainties in the degree to which randomly-aligned molecules react to fields established along a fixed spatial axis. We therefore direct our focus to confining the angular alignment of gaseous molecular samples, both at room temperature and around 20 K.

Preparing a volume of non-isotropically aligned molecules allows a wide range of experiments to be performed. Aspects of the molecular electronic structure can be mapped out with increasing precision as the degree of alignment is improved. For instance, a number of researchers have studied molecular ionization rate anisotropies to help resolve long-standing discrepancies between theory and experiment [1–7]. The alignment process also indicates how easily the molecular orbitals themselves distort from applied fields along various directions (the anisotropic polarizability). Researchers have also been able to extract snapshots of the molecular orbitals by pulling off electrons and then rescattering them from the aligned molecular ion core [8].

Light-induced alignment not only provides information about the molecular structure, but it can further influence laser fields which traverse the aligned sample. When an electron, which is ionized and then driven by a strong oscillating laser field, recollides with its parent molecular ion, it can recombine with the ion by emitting a highly energetic photon whose frequency is a multiple of the ionizing radiation's frequency. This high-order harmonic generation (HHG) process can be enhanced when the molecules have been pre-aligned, as has been demonstrated in various experimental geometries [9–11]. Recent calculations and experiments have also demonstrated the ability to modify the spectral content of ultrashort pulses with aligned molecules, leading to pulse compression [12, 13].

Alignment has been shown to be useful in a wide variety of molecular physics contexts. For example, Friedrich and Herschbach demonstrate the possibility of spatial trapping from the induced dipole interaction from intense lasers [14]. This is useful because current techniques for trapping atomic species (laser cooling) don't translate well to molecular species due to their complicated internal energy distribution. Finally, the angular fixing of molecules gives researchers the ability to control the distribution and excitation of photodissociation products, as shown by Larsen et al [15].

1.2 Atoms and Diatomic Molecules in Laser Fields

For the most part, the interactions of electromagnetic fields with atoms have been well characterized. In addition to the quantum transitions accessible from the absorption/emission of resonant photons, atoms can absorb multiple photons simultaneously and can undergo nonresonant phenomena such as electron tunneling in the presence of a strong, quasistatic applied field. Molecules exhibit similar behavior, but because they have added vibrational and rotational degrees of freedom, the interactions can be significantly more complex. For instance, photons may inelastically scatter off of molecules, exchanging energy with both vibrational and rotational energy levels.

1.2.1 Field Ionization

The most elementary way for an electron to be removed from an atom is via single photon ($\hbar\omega > IP$) quantum excitation into the continuum. If a single photon's energy is too small to put the electron into the continuum, the electron can still be ionized by a combination of two or more such photons, provided that the flux of photons is sufficiently high [16]. When an atom is exposed to a nonresonant laser field with a frequency much lower than the electron Kepler frequency and an intensity significantly greater than 1×10^{13} W/cm^2, atomic ionization can be treated more semiclassically as a Coulomb potential under the influence of a laser field potential, rather than as a multiphoton process. It can therefore be viewed as an electron tunneling through a field-suppressed potential barrier (as in Fig. 1.1), or (if the intensity is sufficiently strong) uninhibited over-the-barrier ionization.

The tunneling ionization rates have been fairly accurately characterized for atoms. A model presented by Ammosov, Delone, and Krainov obtained a tunnel ionization rate equation which depends solely on the laser field strength and the ionization energies of

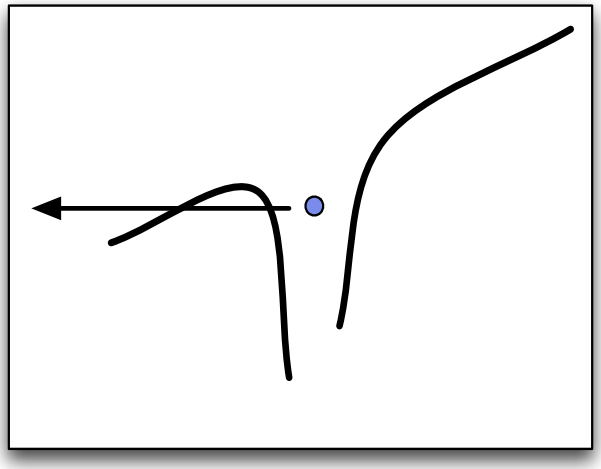

Figure 1.1: Quasistatic model of field ionization, where an electron may tunnel out of the suppressed potential barrier.

the atom in question [17, 18],

$$\langle \omega \rangle = \left(\frac{e}{\pi}\right)^{3/2} \sqrt{3} \frac{Z^2}{(n^*)^{4.5}} \left(\frac{4eZ^2}{(n^*)^4 F}\right)^{2n*-1.5} \exp\left(\frac{-2Z^3}{3(n^*)^3 F}\right) \tag{1.1}$$

where Z is the charge of the ionized atom, F is the applied field strength, and $n^* = Z/\sqrt{2E_n}$ is the effective principal quantum number. Equation 1.1, known as ADK tunneling ionization theory, has successfully predicted experimental ionization rates in atoms, particularly for the noble gases.

The ionization process becomes significantly more complex for molecules, even with the simplest case, the H_2^+ ion. Both the internuclear separation and the relative angle between the applied field polarization and the molecular axis are important parameters. If the field is oriented perpendicular to the molecular axis, the interaction is comparable to the atomic case [19]. However, if there is a significant field component along the molecular axis, the electron now can tunnel out of both Coulombic wells (see Fig. 1.2)[20]. It

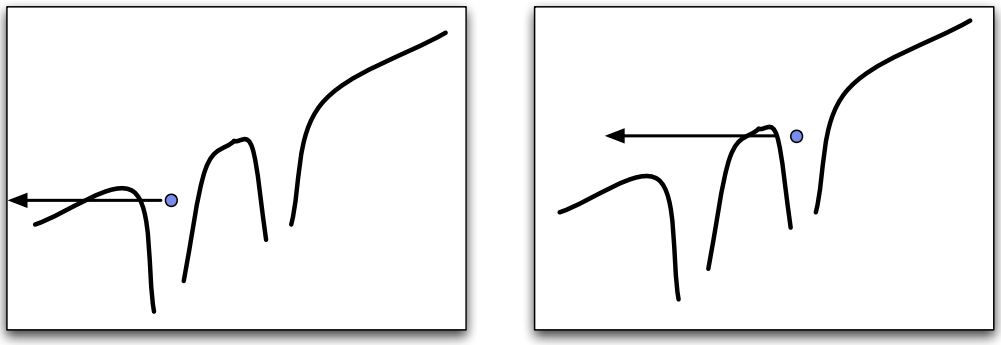

Figure 1.2: Field ionization of a molecule along its internuclear axis. At small internuclear distances, the internal potential barrier is suppressed, and field ionization progresses similar to the atomic case [20].

presents a significant challenge to determine from which nucleus an electron originates. Current diatomic ionization models are based on either a modified version of the ADK tunneling theory [3, 21, 22] or by an all-electron time-dependent density functional theory [4]. Both methods have characterized a wide variety of molecules successfully, yet they have failed to provide a completely general picture.

1.2.2 Multi-Electron Dissociative Ionization

When multiple electrons are removed from a molecule by the field, there is less charge shielding the nuclei, and the molecular bonding breaks down. The dissociation process has been interpreted in numerous ways. First, the molecule can be driven onto a dissociative potential energy curve via single or multiphoton absorption. The molecule in this case could separate into two neutral atoms or an atom and an ion. In another basic interpretation, an intense laser field tears off more than 2 electrons nearly simultaneously, leaving two positively-charged cores still separated by the original molecular equilibrium bond length. These ions experience a strong repulsive force from the Coulomb potential,

and they consequently repel each other, gaining substantive kinetic energy [23] in a process hereafter known as Coulomb explosion. Once researchers had developed lasers capable of multiply ionizing these molecules, though, they soon discovered that the detected fragment kinetic energies almost always were less than those predicted by this basic model, suggesting that more complex dynamical processes were at play in the dissociation.

A slightly more sophisticated theoretical model was developed to describe this relaxation process. According to the model, ionization occurs in two main steps: (1) several electrons are removed in rapid succession while the molecule is at its equilibrium bond length, followed by an initial expansion to some critical internuclear distance R_C, and (2) several more electrons are further removed once the molecule has neared R_c [24]. The presence of R_C has been experimentally verified [25] but the two-step picture is only approximate, as some results have shown that a molecule continually grows as each successive electron is removed [26]. These discrepancies indicate that much more work is needed to fully characterize the strong-field dissociation of diatomics.

1.2.3 Other Processes

When studying the field-molecule interaction, it is useful to consider the effect of the light on the molecular energy levels. Due to the time dependence of molecule-plus-field interaction, energy is not conserved in the molecular system by itself. In the molecule-with-field system as a whole, however, quasi-stationary states exist which depend critically on the intensity of the radiation. These "dressed states" can result in significant changes in the molecular potential energy curves, particularly near curve crossings.

Bucksbaum *et al.* observed evidence for the field-dressed molecular potentials when studying the dissociation of H_2^+ [27]. They considered the situation when two potential energy curves corresponding to electronic states of opposite parity are separated by an

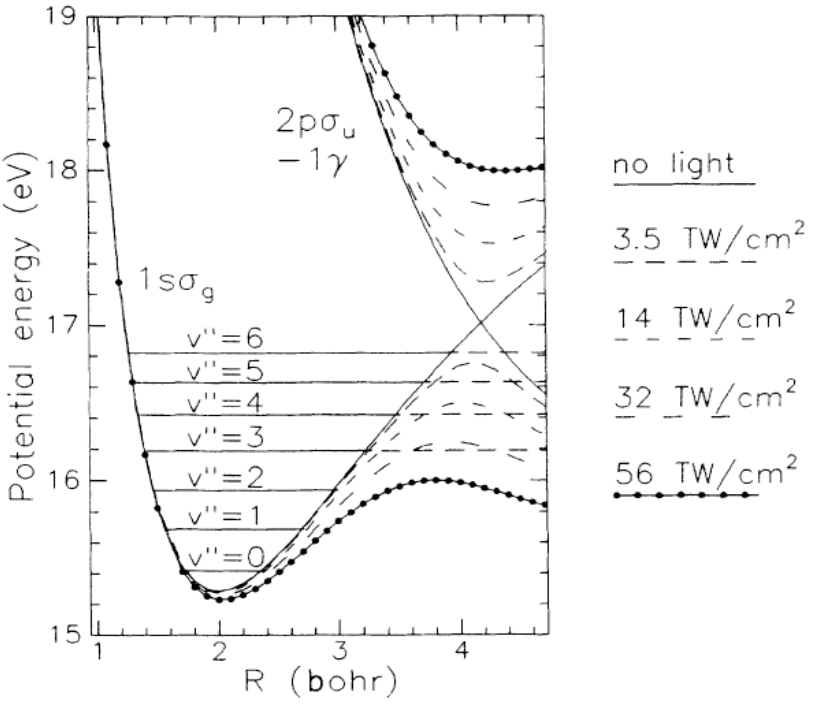

Figure 1.3: Bond softening mechanism as seen in the H_2^+ ion. The degeneracy of two potential curves is lifted by the incorporation of the intense laser field. Trapped vibrational states become clearly unbound as the intensity and the avoided crossing gap increase [27].

odd number of photons at some internuclear separation, R_0. In this case, the strong single or multi-photon coupling between the electron levels creates an avoided crossing of the levels as a function of internuclear separation, centered about R_0. The splitting is the result of the breaking of the degeneracy of the curve crossing with an applied field. The span of this gap (illustrated in Fig. 1.3) depends on the strength of the coupling between the electronic levels and, therefore, increases with intensity. Interestingly, bound vibrational states of the lower curve can become unstable as the gap widens, giving rise to a process known as "bond softening." Although this has been primarily studied and observed with the smallest diatomic ions (H_2^+ and D_2^+), there are predictions that this

phenomenon should apply to more complicated, multielectron diatomics [28].

Additionally, it is possible for bound vibrational states to be created above avoided crossing gaps, as the field-altered energy curves can form local potential wells at internuclear distances noticeably larger than the ground state separation. This process has also been experimentally verified and is known as light-induced vibrational trapping [29] or "bond hardening."

1.3 Molecular Alignment

There are several notable methods for restricting the angular spread of diatomic molecules, most of which are summarized by Stapelfeldt and Seideman [30]. One method employs an inhomogeneous static field to filter out all but one $|J, M\rangle$ state from a molecular beam. This has been shown to isolate single rotational states well [31], but this state's angular spread cannot be very sharply defined. Another technique involves applying a strong DC electric field to torque the molecule via the the permanent dipole interaction, $V_\mu = -\vec{\mu_0} \cdot \vec{E_0}$, which accomplishes "head-over-tail" orientation. Known as the "brute force" method, when the field is turned on (or as the molecules flow through the field), the eigenstates of the field-free molecular Hamiltonian (H_0) adiabatically evolve into the eigenstates of the new Hamiltonian, given by

$$H_{eff} = H_0 + V_\mu \tag{1.2}$$

The downside to this method, is that it frequently requires very high static fields (dozens of kV/cm) or very low rotational temperatures to produce a reasonable angular focusing of the molecules. It is also limited to molecules with large permanent dipole moments. Although decent angular focusing is achievable by this method, the alignment and orien-

tation is only realized in the presence of the field.

1.3.1 Adiabatic Alignment

If a continuous-wave laser field, $E(t) = E_0 \cos(2\pi\nu t)$ acts upon the molecule instead, the field-free eigenstates are now determined by the Hamiltonian [14],

$$H_{eff} = H_0 + V_\mu + V_\alpha \tag{1.3}$$

where

$$V_\alpha = -\frac{1}{2}E^2(t)(\Delta\alpha \cos^2\theta + \alpha_\perp) \tag{1.4}$$

is the induced dipole interaction potential, θ is the angle between the field polarization and molecular axis, and $\Delta\alpha = \alpha_\parallel - \alpha_\perp$. When the laser frequency is significantly larger than the inverse of the pulse duration (i.e. $\nu \gg \tau^{-1}$), taking a time average of the interaction will eliminate the permanant dipole term (depends on $\cos(2\pi\nu t)$), and can be done since the laser field switches back and forth too rapidly for the molecule to directly follow it. This produces an averaged value of $V \sim -\frac{E_0^2}{4}\Delta\alpha\cos^2\theta$ for the induced dipole term. The field-molecule interaction is further enhanced if the laser is pulsed with a duration significantly longer than the field oscillations. In this case, the induced dipole interaction still dominates, and higher field intensities (which scale as E_0^2) are more easily obtained. Similar to the static voltage case, the field-free eigenstates adiabatically evolve to eigenstates of the Hamiltonian, provided that the laser intensity is slowly increased on a time scale much larger than the fundamental rotational period of the molecule. These states are called "pendular" states, and they result in the molecules librating about the applied field axis [32]. This process does not require the presence of a permanent dipole moment, and it only needs the anisotropic polarizability ($\Delta\alpha$) to be nonzero [33], which

is true for all diatomic molecules. Unfortunately, alignment from these pendular states only exists during the presence of the intense laser field. Consequently, experiments which require the precise probing of angle-dependent phenomena (such as strong-field ionization anisotropies) or electron spectroscopy measurements cannot be performed during the aligning pulse.

1.3.2 Transient "Field-Free" Alignment

Transient alignment provides a solution for the aforementioned problem, and its basic mechanism is well understood [5, 34–36]. When the laser pulse has a duration significantly less than the fundamental rotational period of the molecule, then a coherent superposition of rotational states can be populated from a single, initial rotational level via a series of Raman excitations and deexcitations. The superposition is called a rotational wavepacket, and it has the form,

$$\Psi(t) = \sum_J a_J e^{-iE_J t} |J, M\rangle \tag{1.5}$$

where E_J are the rotational energy levels of the molecule. The stimulated Raman processes can be viewed as inelastic photon scattering off a virtual state, resulting in $\Delta J = 0, \pm 2$ transitions. The ultrashort pulse duration also ensures that the intensity, and therefore the induced dipole interaction, is sufficiently large to excite rotational dynamics. Immediately following their exposure to a short "alignment pulse," molecules will undergo an initial alignment. Classically, this alignment is possible from an initial isotropically aligned population because all molecules are torqued toward the laser polarization axis; those at larger angles receive a larger angular impulse from the aligning field. Because of the distribution of rotational kinetic energies within a molecular sample, the initial alignment is rapidly lost. In an ensemble of classical rotors with a continuous energy distribution,

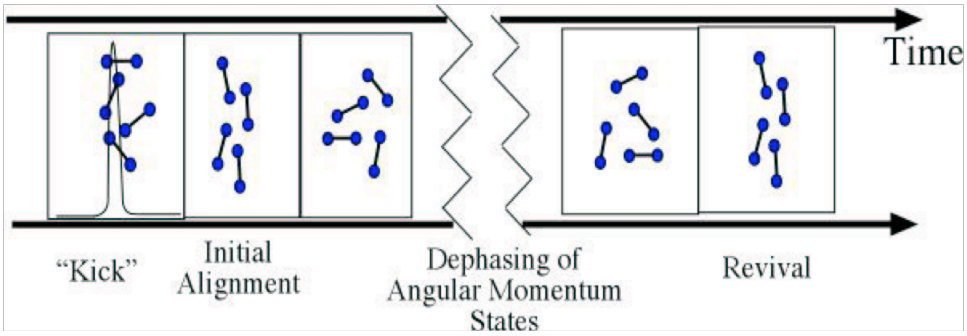

Figure 1.4: Timing diagram of the transient alignment process for diatomics. The laser interaction is immediately followed by an initial molecular alignment and subsequent dephasing of the angular momentum states. Knowledge of the molecule's bond length determines the moment of inertia, and the revival time can be accurately predicted in terms of the rotational constant, $\tau = \pi/B_0$

no additional alignment would be observed. However, for a quantum rigid rotor, all the states within the wavepacket acquire phase at integer multiples of the fundamental angular frequency, so realignment occurs at a predictable time later, as delineated in the cartoon in Fig. 1.4. This alignment "revival" occurs at a time which is commensurate with the ground state rotational period of the molecule. It occurs in the absence of external fields, providing a clean environment for further experiments.

In a perfectly cold initial molecular sample, the $|J\rangle$ state population (normally given by the Boltzmann distribution) would be entirely localized in the J=0 state. Subsequent Raman excitations will populate higher $|J\rangle$ states, while leaving the m value at 0. The resulting high-J, low-m rotational wavefunction is shaped like a narrow cigar along the aligning laser polarization. When a molecule begins with a finite temperature, however, there are higher $|J\rangle$ states initially populated, with m values evenly distributed for each J value. Higher aligning intensities are therefore required to attain comparable angular distributions of the rotational wavefunction. Reduction of the molecule's rotational temperature plays an important role in achieving good alignment and has been thoroughly

studied [37].

1.4 Summary

This dissertation details the findings of several experiments involving the transient alignment dynamics of diatomic molecules. It is grouped into four main parts. In the first part, Chapters 2 and 3 describe in detail the experimental setup and methods for detecting molecular dynamics. Chapter 2 sorts all the relevant laboratory hardware into laser pulse production and diagnostics, ultrahigh vacuum (UHV) hardware and pressure detection, and the hardware and software for molecular ion/fragment detection. Chapter 3 details our techniques for observing transient alignment; we not only use the conventional method of momentum imaging with the two-dimensional position-and-time sensitive TOF spectrometer, but we also employ a much more convenient qualitative detection scheme for rapid feedback and good signal-to-noise.

For the second portion of this dissertation, Chapters 4 and 5 show how preparing an aligned ensemble of diatomic molecules allows us to study the properties of the electron cloud surrounding the two nuclei. Chapter 4 describes a method to measure the ionization rate anisotropy inherent to diatomics, using a ratiometric comparison with closely related atoms. Chapter 5, similarly, shows how field-free alignment can be used to determine the polarizability anisotropy, which is a measure of how deformable the molecular orbitals are under external electric fields applied along different axes.

In the third main section, Chapter 6 illustrates a technique we employed to optimize the level of field-free alignment attainable in a room temperature ensemble of CO molecules. A genetic algorithm directs the experimental (and simulated) phase-shaping of laser pulses which experimentally (and numerically) align molecules. Principal Control

Analysis is then introduced as a method to pinpoint the most significant parameters for the optimization process.

Lastly, Chapter 7 reports a directionality seen in the dissociated fragments when a two-color laser field interacts with a diatomic molecule, in an attempt to create a rotational wavepacket without definite parity. This asymmetry is seen in both heteronuclear (CO, HBr) and homonuclear (N_2) diatomics, and can be attributed to electron localization and enhanced ionization during the strong field dissociation process. In spite of this dissociation asymmetry, and the pump beams proven ability to separately populate rotational wavepackets, we do not detect the presence of transient "head-over-tail" orientation in the heteronuclear samples. A simulation described in Chapter 8 finds a strong temperature dependence in the field-free orientation process.

Chapter 2

Experimental Setup

2.1 Introduction

Data collected for these experiments is generated from one of two ultrahigh vacuum (UHV) systems in conjunction with one of several available laser systems. The vacuum systems are located in laser labs in Chemistry Rm. 204 and in Physics Rm. 168. This chapter focuses on the three primary categories of lab equipment used in these experiments: laser sources and diagnostics, vacuum hardware, and ion/fragment detection components. Both research labs have quite a few hardware commonalities, so this chapter will detail the available hardware, and the experimental methods for the separate experiments will be detailed in the subsequent chapters. The table on page 43 summarizes the laser, vacuum, and electronics equipment in both labs.

2.2 Ultrashort Laser Pulse Production

There were a few ultrafast laser systems available for use in the experiments. They all contain the same basic elements: a high-bandwidth mode-locked oscillator is optically

pumped by a 532 nm CW laser; individual pulses are sliced from the resultant pulse train, stretched temporally, amplified in an optically-pumped laser cavity, and then compressed to durations as short as 30 fsec.

2.2.1 Millennia Vs

The Millennia Vs is a diode-pumped solid-state laser which serves as an optical pump for the various femtosecond oscillators in the lab [38]. Two laser diodes in the Millenia power supply provide up to 13 W of narrow-bandwidth light in the near-infrared regime. This light is coupled through fiber-optic bundles into a laser cavity containing a yttrium vanadate crystal doped with neodymium ions (Nd:YVO_4) . The spectrum of this light overlaps directly with a sharp peak in the Nd absorption spectrum. Population inversion is attained in this medium via a four-level transition scheme, in which photons at 1064 nm are produced by stimulated emission. This 1064 nm light is then frequency-doubled via second-harmonic generation in a lithium triborate crystal (LBO), producing a 532 nm output beam with CW power greater than 4 Watts. The frequency doubling is non-critically phase-matched, so the conversion efficiency is controlled by tuning the temperature of the doubling crystal.

2.2.2 Nd:YLF Pump laser

The Evolution-30 is another diode-pumped solid-state laser which optically pumps the Ti:Sapphire crystals in the ultrafast amplifiers. In this laser, an array of AlGaAs laser diodes pumps a Nd:YLF laser rod. The cavity is acousto-optically Q-switched by an external 1 kHz TTL trigger from a DG535 Digital Delay/Pulse Generator, resulting in 1053 nm, 200 nsec pulses. Similar to the Millennia Vs, frequency doubling is performed inside the cavity with a non-critically phase-matched LBO crystal. This second-harmonic

light passes through a dichroic mirror, exiting the cavity with a final energy up to 20 mJ per pulse. [39]

2.2.3 Ti:Sapphire Oscillator

A Model MTS Mini Ti:Sapphire Laser Kit from Kapteyn-Murnane Labs [40] generates the ultrashort seed pulse light to be subsequently amplified. The kit consists of a cavity oscillator with an end-mirror separation $d \sim 162$ cm and a corresponding longitudinal mode spacing of $\Delta\nu_{sep} = c/2d \sim 92$ MHz. When a large number ($\sim 10^5$) of these modes frequencies are excited, but with random phases, the result is a combination of random constructive and destructive interferences that result in a stable (CW) average value. If, however, all the modes are set in phase, the combination of the fields produces a time-dependent field [41],

$$I(t) \propto \frac{\sin^2(N\Delta\omega t/2)}{\sin^2(\Delta\omega t/2)} \tag{2.1}$$

where N is the number of modes excited in the cavity and $\Delta\omega$ is the difference in angular frequency between adjacent modes. This produces a train of pulses separated by $\Delta t_{sep} = 2d/c$. This set of modes can be attained by dithering the cavity path length, or by physically jolting the system.

The oscillator cavity uses the Kerr lens mode-locking technique to ensure that the phase-locked modes are preferentially amplified in the cavity. This grouping of modes produces pulses with significantly higher intensities than in CW operation, and therefore the modelocked beam experiences nonlinear optical effects such as self-phase modulation and self-focusing in the gain medium, while the CW light remains unchanged. By making the 532 nm pump focal diameter small in comparison to the CW cavity mode, it preferentially puts gain into the phase-locked modes. The output coupler transmits a small

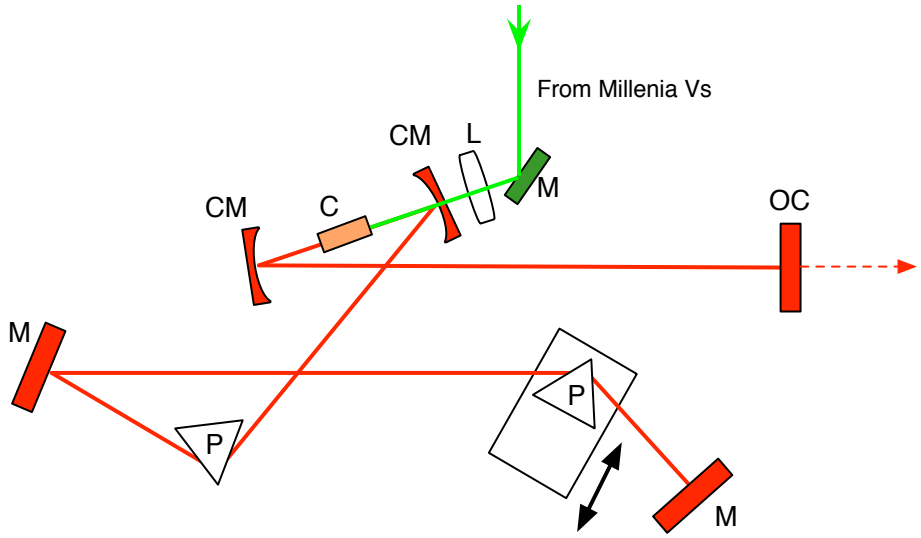

Figure 2.1: Basic layout of the ultrafast Ti:Sapphire oscillator. Roughly 4 Watts of CW 532 nm light focuses into the Ti:Sapphire crystal (C). This crystal has a large gain bandwidth, allowing a large number of longitudinal modes to resonate in the cavity. An output coupler (OC) leaks out the pulse train. The large bandwidth of the light pulses creates significant group velocity dispersion; therefore, a prism pair (P) helps to compensate for the GVD accrued during transmission through the crystal and the output coupler [42].

fraction of the pulse train outside the cavity, producing a train of 30 fsec pulses centered at 780 nm. The layout of the oscillator cavity is shown in Figure 2.1.

The resultant femtosecond mode-locked pulse train propagates into a dual stage amplifier. The crystal is unable to amplify such a short pulse because of its damage threshold, so the pulse is stretched out via group velocity dispersion (GVD) in a grating expander, before being amplified. After the amplification, the pulse duration is shortened with a grating compressor. This layout is known as chirped pulse amplification (CPA) and is frequently employed for ultrafast laser amplification.

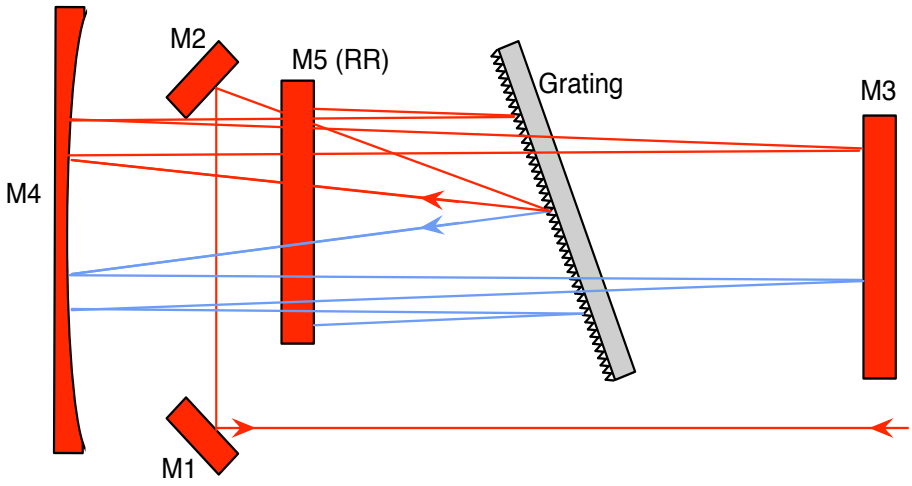

Figure 2.2: Pulse stretcher diagram (view from top) from KMLabs [40]. The output beam is slightly vertically diverted and is then picked off for amplification. Note: lines directly overlapping mirrors (M) and grating pass over, and not through, the optics.

2.2.4 Grating Stretcher

The grating expander makes up the first portion of the CPA scheme and is shown in Figure 2.2. The grating spatially disperses the various frequencies of the ultrafast pulse, and group velocity dispersion develops from the different path lengths for the redder/bluer components. This setup linearly "chirps" the pulse duration up by several orders of magnitude, with the only difficulty being the amount of light lost from specular reflections from the gratings. Fortunately, this is not problematic because the laser pulse energy will saturate after several passes in the amplifier, without much sensitivity to the initial pulse energy.

2.2.5 Regenerative Amplifier

In the chemistry lab, one of the available laser amplifiers is a Spitfire system (see Fig. 2.3a), with a regenerative amplifier and a double-pass linear amplifier. The Spitfire box contains the aforementioned grating stretcher, as well as the final compressor. The strongly chirped pulses emerging from the stretcher are incident upon a Pockels cell, which switches them into a linear "regen" cavity when a high voltage is placed across the crystal. After several complete paths through the amplifier cavity, in which the pulses achieve gain from a Ti:Sapphire crystal pumped by the Evolution Nd:YLF, another Pockels cell switches the pulses out of the regen cavity and into the linear amplifier. Pulses exiting the regen cavity can have energies as high as 1.6 mJ. In each of the two passes through the bowtie-configuration lin-amp, the laser pulses gain $\sim$ 400 - 500 μJ, with the maximum energies of up to $\sim$ 2.5 mJ per pulse.

2.2.6 Multipass Amplifier

In both labs, the 30 fsec oscillator light is amplified with a multipass Ti:Sapphire amplifier. The amplifier crystal sits in the center of a triangular cavity, through which the oscillator "seed" light traverses 8-10 times. On each pass, the beam travels through a sequence of apertures which ensures that the center of the seed beam is cleanly amplified, while reducing the thermal beam expansion effects (for the 1 kHz laser). The setup is illustrated in Figure 2.3b.

2.2.7 Compressor

The pulse compression operates on similar principles to the expander, but the path length difference for the various frequencies now imparts negative GVD ("linear chirp") on the

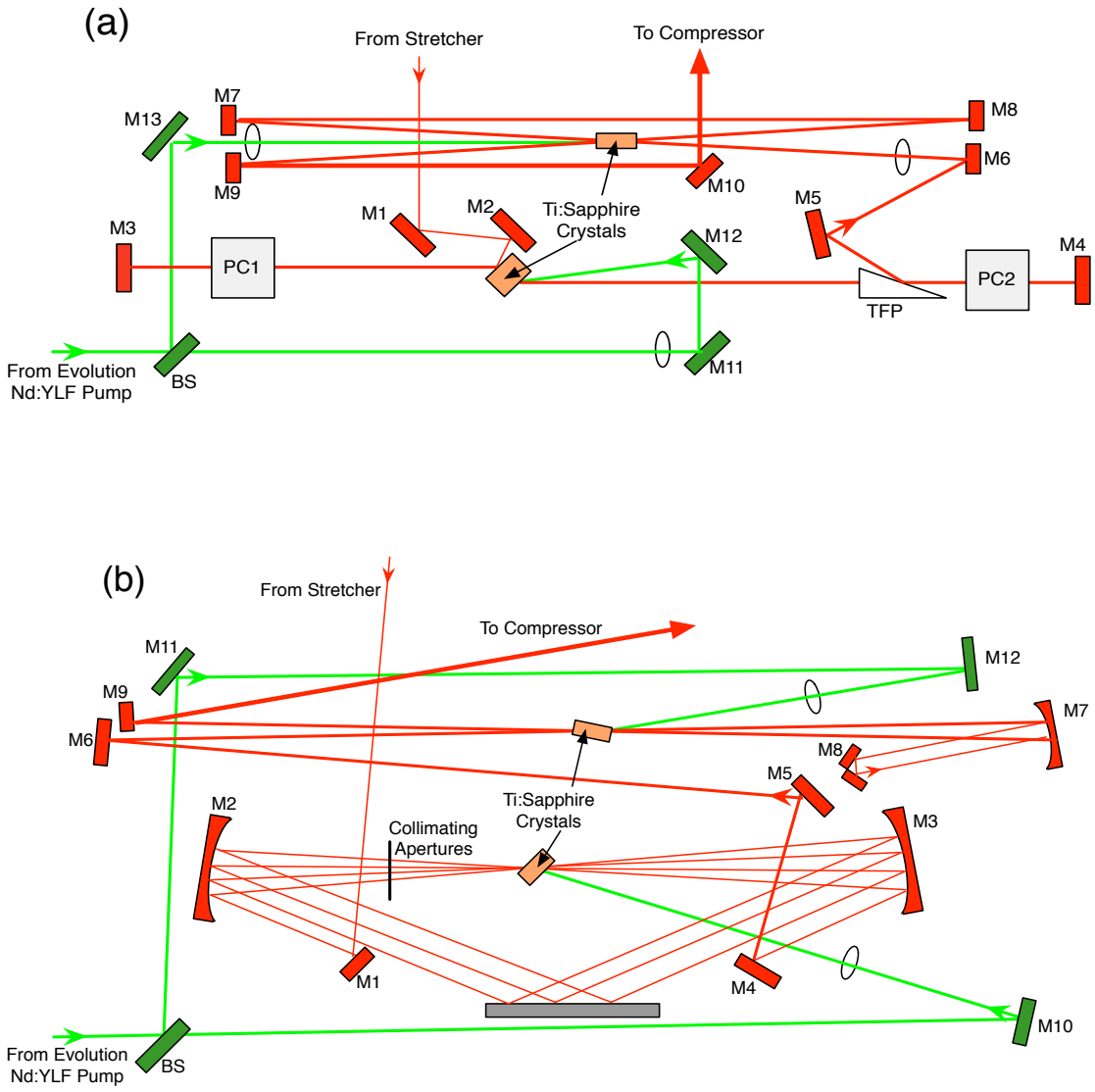

Figure 2.3: Diagrams of the two ultrafast amplifier systems, (a) the Spitfire regenerative amplifier plus bowtie linear amplifier, and (b) the multipass amplifier (also with a bowtie lin amp). In the Spitfire, the seed pulse traverses the linear cavity about 10 times before the output Pockels cell (PC2) rotates the pulses' polarization. With the multipass amplifier, the seed bounces around the 1st stage 8-10 times before being spatially picked off by M4. In both cavities, the pump light is distributed to both Ti:Sapphire crystals.

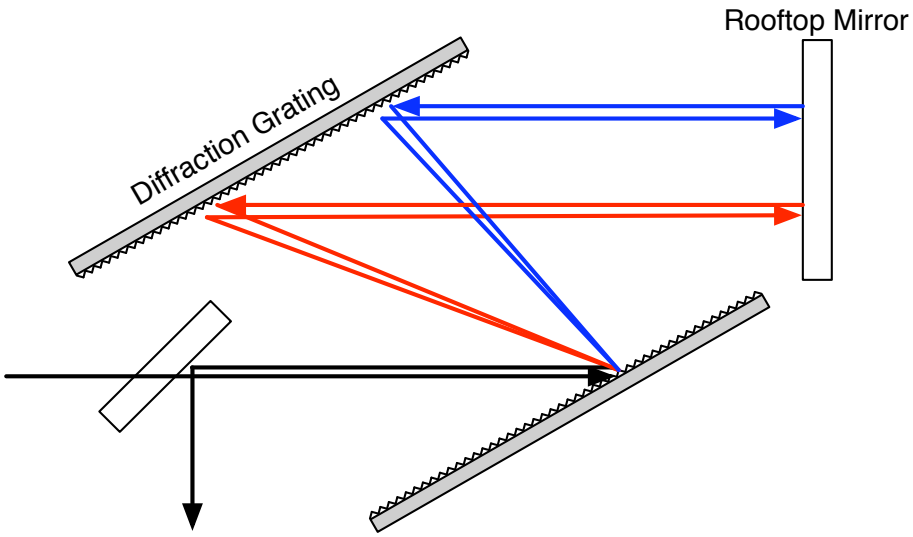

Figure 2.4: Diagram of a typical grating compressor. The relative path length between the redder and bluer frequency components is adjusted by the distance between the parallel gratings. In some instances, the compressor geometry is folded over once more, requiring the use of only one grating, and an additional rooftop mirror.

amplifier output. The compressor schematic is shown in Figure 2.4. The gratings are angle tuned to match closely with the gratings in the expander, in order to minimize the higher-order dispersion accumulated in the amplifier cavity. In this case, the specular reflections off the compressor gratings directly impact the final laser pulse energy, so care is taken to prevent too much dust from settling. Even with a perfectly clean grating, the various compressors in both labs have a peak efficiency around 65%, with typical values around 55%. With the Spitfire system, final compressed pulse durations can be short as 100 - 125 fsec. In both multipass amplifier configurations, pulse durations reach as low as 30 fsec.

2.2.8 Laser Pulse Diagnostics

With ultrashort pulse durations, pulse characterization requires a fast strobe process to sample the pulse magnitude at various delays. Since there are no manmade tools which can operate on this ultrafast timescale, the best option is to use the laser pulse itself. The following methods consist of an ultrafast laser pulse which has been split and subsequently recombined in a nonlinear optical medium.

Auto-correlation

The single-shot intensity autocorrelation is a convenient tool to rapidly display an ultrashort pulse's duration. Some of the compressed laser light is extracted, and this beam is split up and immediately recombined in a nonlinear BBO crystal which is specifically cut for non-collinear type I phase matching. Second harmonic generation (SHG) in the crystal occurs when part of each pulse is overlapped temporally and spatially. The temporal characteristics, as a result, are mapped onto the spatial axis transverse to the beams' propagation, and the width of the SHG beam (Δx) is determined by [43]

$$\Delta x = \frac{\Delta\tau_a v_g}{\sin\Phi} \tag{2.2}$$

where 2Φ is the beams' crossing angle, v_g is the pulse group velocity, and $\Delta\tau = \int_{\infty}^{\infty} I_0(t)I_0(t-\tau)dt$ is the pulse temporal autocorrelation.

FROG

The single-shot autocorrelation is convenient for rapid estimates of the laser pulse's duration, but due to the nature of the overlap signal, there is no phase information available. Trebino *et al* developed a technique which extracts both amplitude and phase informa-

tion from the laser pulse [44]. Known as Frequency Resolved Optical Gating (FROG), it generates a delay-dependent signal in single-shot mode inside a nonlinear optical medium and diffracts the spectrum along the perpendicular axis to the delay. The resulting two-dimensional spectrogram (a.k.a. FROG trace) has the form,

$$I_{FROG} = \left| \int_{-\infty}^{\infty} dt E_{sig}(t,\tau) \exp(i\omega t) \right|^2 . \tag{2.3}$$

where $E_{sig}(t,\tau)$ is the nonlinear mixing signal generated by combining the pulse with a replica of itself in the medium. It provides feedback about the pulse's temporal width, as well as variations in its spectral phase.

We utilize two distinct geometries of the FROG [45]. For the 30 fsec systems in both labs, a fraction of the output light enters an SHG FROG apparatus, which is nearly identical to the single-shot autocorrelator geometry, but with the addition of a spectrometer at the output. The SHG FROG mixing signal is just $E_{sig}(t,\tau) \propto E(t)E(t-\tau)$ which generates a FROG trace with reflection symmetry.

For the 100 fsec system, we incorporate the PG FROG geometry, which has the two beam paths cross in a nonlinear Kerr medium placed between two crossed polarizers (shown in Fig. 2.5). The PG FROG trace arises from $E_{sig}(t,\tau) \propto E(t)\left|E(t-\tau)\right|^2$, which provides more visually accessible information than the SHG version. The images from the 100 fsec PG FROG apparatus are captured by a two-dimensional CCD array and are archived with the LBA-PC software from Spiricon for use with the 100 fsec pulse-shaping in Chapter 6.

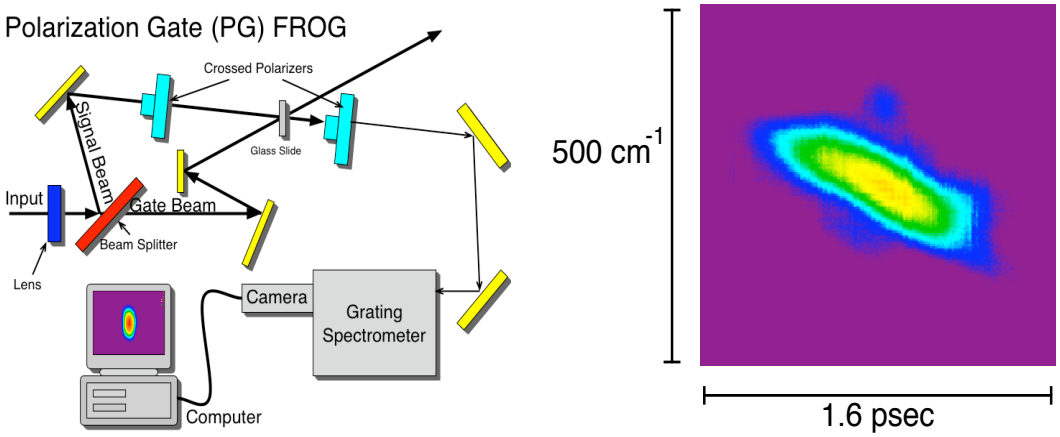

Figure 2.5: PG FROG apparatus and sample trace of a linearly chirped pulse captured by the CCD camera.

2.3 UHV chambers

The experiments are all performed under high- or ultra-high vacuum conditions within two stainless steel chambers. One of these chambers is located in Room 204 of the Chemistry Building (#1) and is illustrated in Fig. 2.6a. The primary components of this system are the gas inlet lines, the time-and-position-sensitive mass spectrometer, detector electronics, vacuum gauges, liquid-nitrogen cold trap, vacuum pumps, and laser windows. In the final months of data collection, a secondary chamber (#2) located in Room 168 of the Physics building became available, which allowed the recording of additional data with a better molecular beam geometry, and markedly better rotational cooling. This chamber is illustrated in Figure 2.6b and contains a molecular beam/skimmer apparatus, a time-of-flight mass spectrometer, vacuum gauges, a cold trap, pumps, and laser windows. Stainless steel Conflat flanges combine adjacent hardware components, and they have a sharp knife-edge which digs into a copper gasket to maintain the vacuum seal.

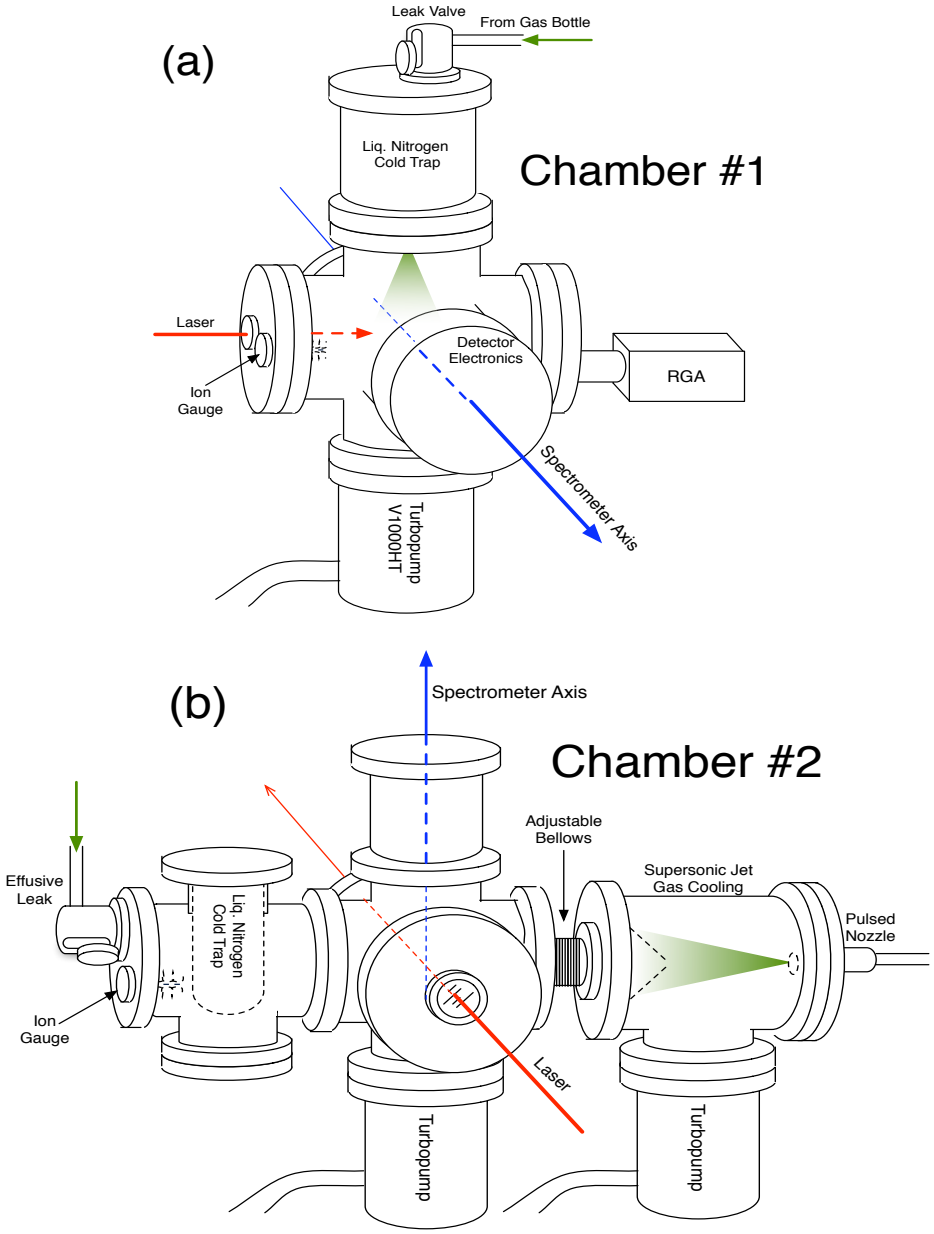

Figure 2.6: Diagrams of the two ultrahigh vacuum systems. (a) Chamber #1 resides in the chemistry lab, and (b) Chamber #2 is located in the physics lab. The laser beam, spectrometer, and gas jets are oriented along orthogonal axes. The summary of the differences between the two labs is given on page 43.

2.3.1 Pumps

Roughing pumps

Rotary vane roughing pumps are workhorse of the high vacuum experiments. The vanes guide a volume of air taken from the pump intake and force it out the exhaust line. These pumps are able to bring a chamber or gas line down to several dozen mTorr in pressure, and they are used both to clear out gas inlet lines and to pump gas out of the foreline sections of turbopumps.

Turbomolecular pumps

High vacuum pressures (or greater) are needed to perform molecular dynamics experiments. We employ a variety of Varian Turbopumps to achieve base pressures as low as 3×10^{-10} Torr. The pumps consist of a turbine with multiple stages of tilted fan blades that force unidirectional gas flow. The turbine is supported and controlled by a motor rotor embedded within lubricated ceramic ball bearings. The pump has a slowly-ramping "soft start" mode which allows the turbo to rough out the chamber directly from atmospheric pressure, before full speed operation [46]. The pumping speeds for the turbopumps ranges anywhere from 70 liters/sec in the smaller models, up to nearly 1000 liters/sec for the largest version used.

2.3.2 Gauges

We utilize a few pieces of hardware to give various measurements of background pressure inside the chamber or gas inlet lines. A Varian Sentorr gauge controller provides pressure readout for the thermocouple and ion gauges, and it activates setpoint relays to interlock them with the UHV chamber. A Residual Gas Analyzer provides total- and

partial-pressure measurements over a wide range of chamber pressures and is controlled by computer software.

Thermocouple Gauges

In order to detect roughing vacuum pressures, we use several Varian Model 531 thermocouple vacuum gauges to measure how efficiently a background gas conducts heat away from a source. In these gauges, a current runs through and heats up a wire filament. A thermocouple is in contact with this filament, measures its temperature, and outputs a voltage value corresponding to the filament's temperature. The gauge controller converts the voltage into a corresponding pressure value. When setting up the thermocouple in a new system, it must be calibrated at both 1 x 10^{-3} Torr and 760 Torr for accuracy. Because the thermocouple gauge does not measure pressures lower than rough vacuum, its main functions in this experiment are to check the backing pressures for the turbo pumps and for leak-checking the gas-inlet lines.

Nude Ion Gauge

The thermocouple gauges are unable to measure pressures below 1×10^{-3} Torr, so we employ the use of an ion gauge to measure ultrahigh vacuum pressures. Most ion gauges today are based off of the Bayard-Alpert design, where a wire grid with a positive voltage surrounds a thin collecting wire at a negative voltage. A filament just outside the grid is heated to emit electrons, which flow towards the grid. These electrons bombard any ambient gas molecules, producing positive ions that are attracted to the negative collecting wire. This experiment uses a nude ion gauge geometry, where the filament-grid-collector assembly is fully immersed into the vacuum system. The ion current is proportional to the gas pressure and is calibrated electronically within the Varian SenTorr gauge controller.

We are able to detect background pressures as low as 2×10^{-10} Torr, and we can perform controlled gas leaks with rapid gauge readouts (< 1 sec)

Residual Gas Analyzer (RGA)

In addition to knowing the total gas pressure in Chamber # 1, we occasionally need to determine the partial pressure of all the constituent gases in the chamber. An SRS RGA 200 is attached to the main portion of the UHV chamber via a Conflat flange. An electron impact ionizer protrudes into the chamber and ionizes a portion of the ambient gas molecules via 70 eV electron bombardment. The resulting ions and fragments are flown through a mass spectrometer and are separated according to their mass/charge ratio. The accompanying software enables us to obtain analog images of the mass spectrum, in addition to near realtime measurements of the individual masses [47].

2.3.3 Interlocks

Most of the turbopumps, gauges, and high voltage electronics on both chambers are connected by interlock circuitry to shut down all sensitive experimental components whenever there is a power outage or a component failure. This is accomplished by forming a series of voltage relays which control the AC power to the turbopumps, pneumatic valves, and high voltage power supplies.

2.3.4 Cooling Apparatus

Liquid Nitrogen Cold Trap

In the chemistry lab setup(#1), there is a 4 L liquid nitrogen trap directly above the interaction region, and the gas input line coils around this bath in a thin copper tube

before depositing the molecules into the spectrometer. This gas deposit method is considered effusive, because the molecular mean free path λ_0 is much greater than the tube diameter. It has served to rotationally cool the input gas molecules, as well as to freeze out background water vapor in the surrounding chamber. Mild cooling is visible both for effusively-leaked gas molecules, as well as for molecules which traverse a 2 meter length of copper tube wrapped around the cold trap. As demonstrated in Chapter 3, temperatures as low as 200 K have been detected when probing the rotations of the aligning molecules (only 200 K because the gas molecules do not have sufficient time to equilibrate with the 77K temperature of the bath). Better cooling could be accomplished in Chamber # 1 with a supersonic molecular beam expansion, but a very large pump would be need to pump an intermediate skimmer region, which is detailed in the following section. Since the hardware required to accomplish this was unavailable, we limited the scope of chamber # 1 to near-room temperature experiments.

Supersonic Molecular Beam Cooling

In order to effect more significant cooling, a supersonic gas expansion apparatus was constructed in the physics lab, with a home-built skimmer for collimation. A molecular gas is kept in the source region at a high pressure (> 50 psi), and a nozzle with a 0.8 mm diameter aperture opening to a larger region pumped by a large turbo. The ultrafast laser is pulsed at a 15 Hz rep rate in this lab, so a pulsed valve is employed.

When the mean free path length (λ_0) obeys $\lambda_0 \ll D$, with D being the nozzle aperture diameter, there are many collisions between molecules flowing out from the source region, and the gas molecules will adiabatically expand into the vacuum region [48]. This

expansion is governed by the equation,

$$\frac{T_f}{T_i} = \left(\frac{p_f}{p_i}\right)^{(\gamma-1)/\gamma} \tag{2.4}$$

where i and f refer to the initial and final conditions, T and p are the temperature and pressure, and γ is the ratio of the heat capacities (C_p/C_V) depending on the type of gas. Equation 2.4 illustrates how maintaining a large pressure differential between the source and expansion region can greatly reduce the rotational temperature of the molecules. The expansion is considered supersonic because the rapid rarefaction of the gas will make the speed of sound decrease significantly, to the point where it is less than the forward flow velocity of the molecules. This quality of the gas expansion is characterized by the Mach number, which can therefore be also used to determine the cooling capabilities of the expanding jet,

$$\frac{T_f(x)}{T_i} = \left[1 + \left(\frac{\gamma-1}{2}\right) M(x)^2\right]^{-1} \tag{2.5}$$

where the peak achievable Mach numbers are given by

$$M \propto (\sqrt{2}\sigma\rho_i D\varepsilon)^{(\gamma-1)/\gamma} \tag{2.6}$$

where ρ_i is the number density in the source, σ is the cross section, and ε is a collisional effectiveness parameter [49]. This formulation refers to gas samples with one molecular species; however, the condition that increasing the parameter $\rho_i D$ (and equivalently $p_i D$) to achieve better cooling still applies generally. In order to optimize this parameter, efficient pumping is required. The gas source nozzle is sealed by a ceramic poppet which is pulsed open for $\sim 150\mu s$ by a solenoid coil at 15 Hz, matching the physics lab laser repetition rate. A homebuilt skimmer with a 2 mm diameter aperture collimates the gas

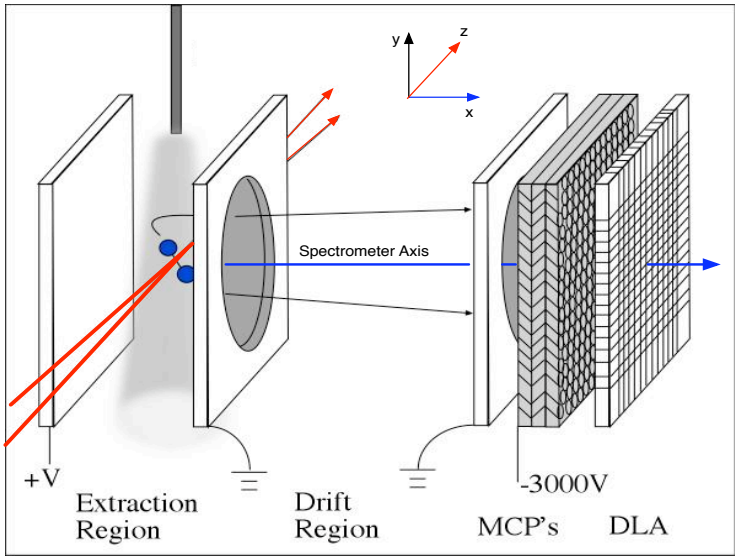

Figure 2.7: Diagram of the TOF spectrometer. Charged particles are formed in the extraction region and are accelerated along the x-axis towards the time-and-position-sensitive detectors.

jet.

2.4 Detection Hardware

2.4.1 Time-of-Flight Mass Spectrometer

The centerpiece of each chamber is a single-stage time-of-flight mass spectrometer, designed to separate charged fragments according to their mass/charge ratio (see Fig. 2.7).

The spectrometer is constructed with several square metallic plates with large central circular openings, and these are all aligned perpendicular to a common axis.

For consistency, this axis will be labeled the x-axis in further discussions of experimental geometries. The first section of the spectrometer is the ion extraction and acceleration region. The back plate in this region is given a large (> 100 V) voltage, and the forward

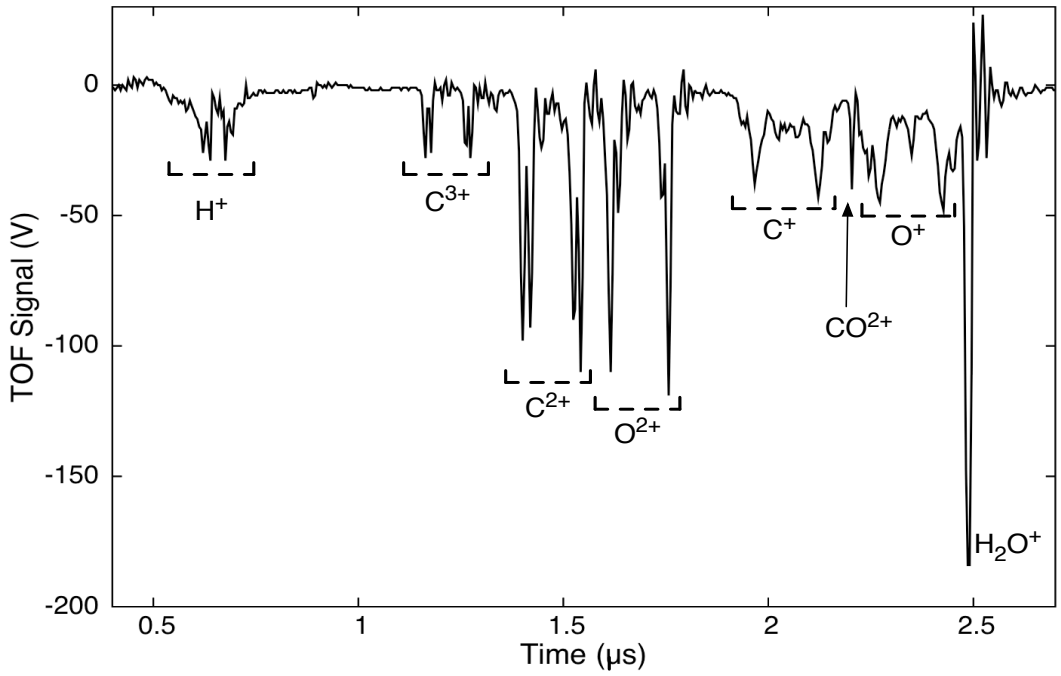

Figure 2.8: Sample time-of-flight spectrum for CO from the physics chamber. The probe is linearly polarized parallel to the spectrometer axis, and multiple dissociation channels are visible for the various charge states.

plate is grounded. If the plates' area were to extend to infinity, the electric field would be uniform ($E = V/d$); however, due to the spatial dimensions of the plates and the due to the large circular holes to allow the paths of the molecules, the field lines would have noticeable curvature at off-axis points. To correct this, several additional plates are spaced throughout the region, and the input voltage is divided down to the ground plate with a chain of resistors. The second component of the spectrometer is the field-free drift region, in which the ion flight times are further separated and isolated according to their mass/charge ratio [50], and the final signal is output as a realtime mass spectrum as in Figure 2.8.

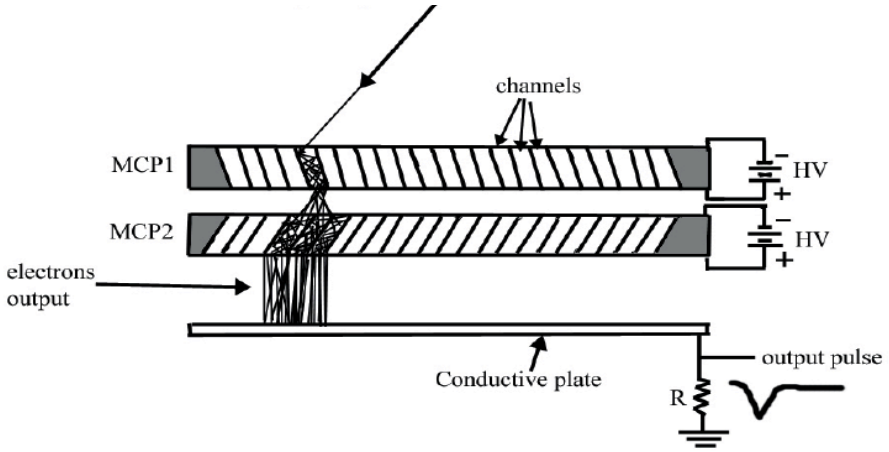

Figure 2.9: A cross section of a chevron pair of microchannel plates with the cascading electron shower that results from an ion collision at the entrance [51].

2.4.2 MCP

Microchannel plates are two-dimensional arrays of numerous electron multiplier tubes made of lead glass which are densely packed and then sliced into sheets which are a few mm thick. The tubes are all made nearly identical from a draw/multidraw technique, and they are prepared with a semiconducting wall coating in order to allow recharging from an external power supply [51, 52]. When a charged particle collides with the tubes' wall coating, a cascade of electrons propagates down the tube. The tubes are oriented with a small ($\sim 10^o$) bias angle relative to the channel plate normal. This prevents ion feedback, which arises when cascading electrons bombard ambient gas molecules near the back face of the plate and produce ions that fly back towards the front face. To further reduce this phenomenon, MCPs are frequently stacked in impedance-matched sets of 2 or 3, where neighboring plates are oriented so that adjacent tubes form the most acute angle

possible (see Fig. 2.9). For the two plates, this is known as the Chevron configuration (Chamber #2, Physics Lab), and with a third it is referred to as a Z-stack configuration (#1, Chemistry).

A bias voltage drop of $\sim$ 1 kV is needed across each plate for the separate channels to function properly as electron multipliers. We discovered that in the Chemistry lab setup, if the MCPs are bombarded to saturation with ionized fragments at 1 kHz, the channels are unable to fully replenish the electrons in the channel walls, resulting in "dead spots" which persist for indefinite periods of time. When detecting ion hits (as described in the next few sections), the channels of interest most frequently will be on the earlier end of the TOF fragment spectrum. Fragments with higher m/q ratios often dominate TOF spectra at the later times. Therefore, on every laser shot we discharge the established MCP bias voltage immediately following the target species in the TOF spectrum. This is controlled by a Behlke high voltage transistor switch which is triggered by a separate channel from the 30 fsec laser's DG535 pulse generator.

2.4.3 SR250 Fast Gated Integrator

For applications where only the fragment TOF information is important, we can perform a number of mathematical operations on just the voltage signal from the back MCP. This is done primarily with the SR250 Gated Integrator and Boxcar Averager Module from Stanford Research Systems. This module creates a fast tunable-delay gate ranging from 2 ns to 15 μs in width, and it integrates an input signal over this time window. At the output there is a DC voltage which is a moving average from 1 to 10,000 integrated samples [53]. To reduce noise fluctuations, we typically choose to average around 100 samples; therefore, we require that the TOF signal be in current mode (high enough flux of ions to produce a continuous nonzero pile-up of fragment hits). The analog voltage signals from the TOF

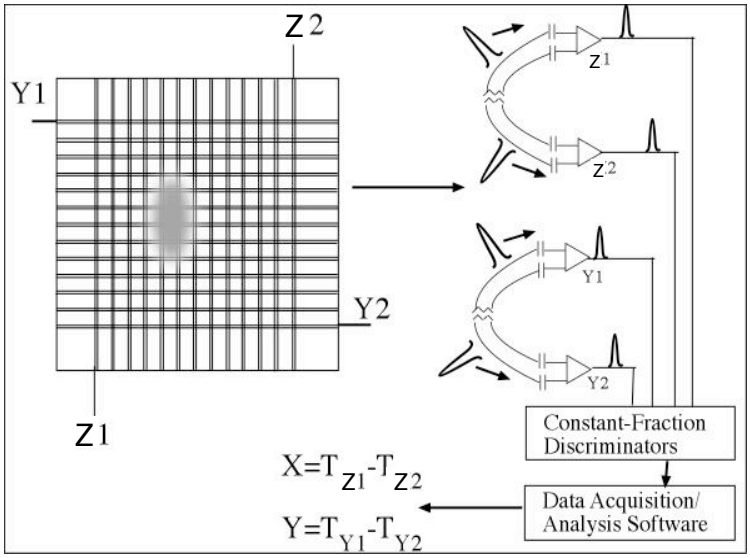

Figure 2.10: Schematic of the delay-line anode.

spectrometer are input into an SR245 Computer Interface, also from Stanford Research Systems. Arithmetic functions can be performed on multiple boxcar voltage outputs prior to the SR245, or this can be done numerically in the software.

2.4.4 DLA

The spray of electrons (originating from one charged particle colliding with the MCP) is incident upon a two-axis helical-delay-line anode (DLA) that serves as a two-dimensional position-sensitive detector (shown in Fig. 2.10). For each axis, a copper wire pair ($\sim$100 ft) is tightly spiraled around a 10 cm $\times$ 10 cm square ceramic block. The wires are connected to a +400 VDC supply, and a voltage divider ensures that each wire in the pair is given 400 V & 350 V, respectively. The wire with the higher voltage is called the Collecting (C) wire, and the electron spray will be preferentially drawn towards this one. The Non-Collecting (NC) wire serves as a reference voltage for the differential signal processing.

Once the electron spray collides with the wire grid, a voltage spike emanates from the point of collision, traversing the C wire in both directions along both axes. The difference in travel time along either axis of the anode reveals the two-dimensional location of the electron spray, and hence the location of the molecular fragment event.

2.4.5 Fast Electronics

Constant-Fraction Discriminators

The count-mode signals coming off of the C/NC wire pairs from the DLA are capacitively coupled to a series of high-speed electronics. First, the differential signal between the C and the NC wires is amplified with a Model 322 Voltage Amplifier from Analog Modules. This ensures that stray fields picked up by the anode wires are eliminated before the signals propagate any further. Each C/NC wire pair has two amplifiers - one at each end - and the amplified signal pulses enter a set of Constant Fraction Discriminators (CFD). These convert the signal pulses to steady, identical NIM pulses ($\sim$ -0.8 V), which fire at a predictable point in the risetime of the signal. Care must be taken to ensure that the detector is truly in count mode, or ion hits will be overlooked. The voltage spikes from the MCP array are capacitively coupled to another Model 322 Voltage Amplifier, and another (optional) CFD can transform them into NIM-quality signals for event consistency checking. One last CFD is utilized to convert a voltage spike from a photodiode at the laser output, for triggering purposes.

The Behlke swtich mentioned in section 2.4.2 shorts out the voltage on the channel plates at a designated time, but this generates a large field spike that is easily picked up by the anode wires on every laser shot. The wires therefore detect a large phantom pulse, which could accidentally be mistaken for a charged fragment. In order to correct

this, a Phillips Scientific Model 794 Gate/Delay Generator creates a variable NIM-size gate, which is multiplied fourfold and is positioned to overlap temporally with the desired fragments' 4-coordinate signals from the DLA. The signals and gates are combined with a Logic-AND function in a Phillips Model 752 logic unit, and the resulting signal is filtered of all temporally extraneous pulses before it is sent to the computer.

TDC8-ISA card

Once the appropriate timing signals have been converted into consistent NIM-size pulses, the signals propagate into a time-to-digital PC converter card, the TDC8-ISA. This card is able to read signals from 8 separate sources and a trigger source, but only about half of these available inputs are needed. The PC card receives a NIM input from each end of the DLA axes: Z1, Z2, Y1, and Y2. There is one optional input from the back MCP signal, and the trigger signal from the photodiode enters the COM input. For each laser shot, the card is able to store timing signals for up to 16 fragment hits over a 16 μs time range, with a minimum time separation of $\sim 30 - 50$ nsec.

2.5 Detection Software

2.5.1 TakeData

The TakeData software program is used to read the averaged voltage signals taken from the SR245 Computer Interface Module through a General Purpose Interface Bus (GPIB) connector. The software instructs the user to specify the duration of a scan, in addition to parameters for the external and internal averaging of the input signals. It can be interfaced with an external stepper motor and can send clock pulses intermittently between collected data points.

2.5.2 CoboldPC

Full characterization of fragment momenta is accomplished with the CoboldPC software developed by RoentDek Handels GmbH in Germany. Its functions include both data acquisition from the TDC card and on- or offline data analysis in list-mode format. The acquisition process runs in either a common start or common stop mode, where the trigger line in the TDC8-ISA COM port functions as a signal to begin, or finish, data collection during one laser shot (All experiments using CoboldPC in this paper are performed with the common start option). Data collection is therefore not constrained to begin at the time of ionization. By delaying the photodiode trigger with a Phillips Model 794 Delay Generator, the software can start gathering data immediately before a chosen charge-state. The data is stored in list-mode format, where the raw time and position coordinates are kept in separate bins according to the time of acquisition. This enables the data collection to be rerun indefinitely, with a different data analysis each time [54].

The raw data are plotted in a sequence of one- and two-dimensional spectra, in which the data points are binned into histograms. Boolean operators are applied to adjacent coordinate sets as a noise filtering mechanism, and numerous user-generated spectra can be plotted at run-time. In order to register an ion hit, the software requires that a voltage pulse is detected at both ends of both wire axes. Since both axes are wrapped with approximately equal lengths of copper wire, we can say for a valid ion hit,

$$t_{Z1} + t_{Z2} \simeq t_{Y1} + t_{Y2} \tag{2.7}$$

where each time is measured relative to the COM trigger and is binned into 0.5 ns channels. Fig. 2.11 illustrates the various timing labels used in the data analysis. By requiring the condition given in Eq. 2.7, only events with a detectable hit on all four coordinates are

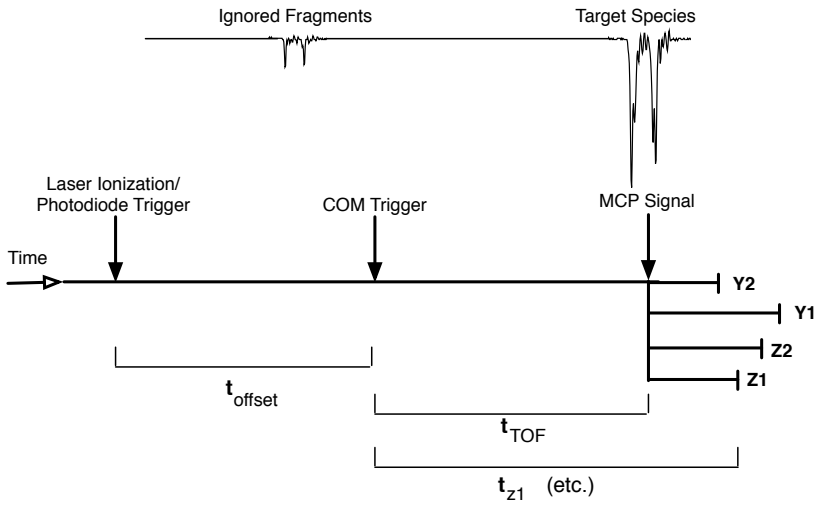

Figure 2.11: Timing diagram for CoboldPC software program

accepted. A simultaneous hit from the (optional) back MCP NIM signal can also be utilized as a count filter. These coincidence requirements are frequently employed by detectors in particle physics experiments.

Nearly all the user-programmed data analysis is contained within the TDC8-ISA.cpp file in the program workspace. First, the position data (shown on the left in Figure 2.12) is calculated:

$$\begin{aligned} z(channels) &= t_{Z1} - t_{Z2} \\ y(channels) &= t_{Y1} - t_{Y2}. \end{aligned} \tag{2.8}$$

The time-of-flight information can either be taken directly from the back MCP NIM signal, or it can be closely approximated from the position coordinates. The latter method has the advantage of good accuracy without the significant count rate reduction that accompanies

the inclusion of TOF coincidence filtering.

$$t_{TOF} \simeq \frac{t_{Z1} + t_{Z2} - 200}{2}(channels). \tag{2.9}$$

In Eq. 2.9, the calculation uses the fact that the t_{Xi} coordinates are nearly identical to the pure MCP time-of-flight, but with the addition of the time for a pulse to travel from the middle of the DLA grid to the ends of the wires (see Fig. 2.11). The initial momentum vectors which are transverse to the spectrometer axis are calculated simply by

$$p_y = \frac{m\Delta y}{t_{TOF}} = \frac{m(y - y_0)}{t_{TOF} + t_{offset}} \tag{2.10}$$

To calculate the initial momentum along the spectrometer axis, we calculate the time-of-flight for ions with an initial velocity v_0 along the x-axis, using the formulas from Appendix C. Using a quadratic least-squares fit, an expression is calculated for the x-momentum in terms of $t - t_0$, where t_0 is the time-of-flight for fragments with no initial x-velocity,

$$p_x \equiv c_1(t - t_0)^2 + c_2(t - t_0) + c_3 \tag{2.11}$$

where the c's are coefficients which depend on the fragment mass and charge, as well as the spectrometer voltage. The entire set of extracted momentum points is then displayed at the program output, shown on the right in Fig. 2.12.

2.5.3 DC (Data Collect)

The Data Collect program is used in the physics lab to read time-dependent voltage traces off of the Tektronix 2440 oscilloscope through a GPIB connection. It allows an indefinite number of user-defined gates which can be integrated over. Similar to TakeData, the

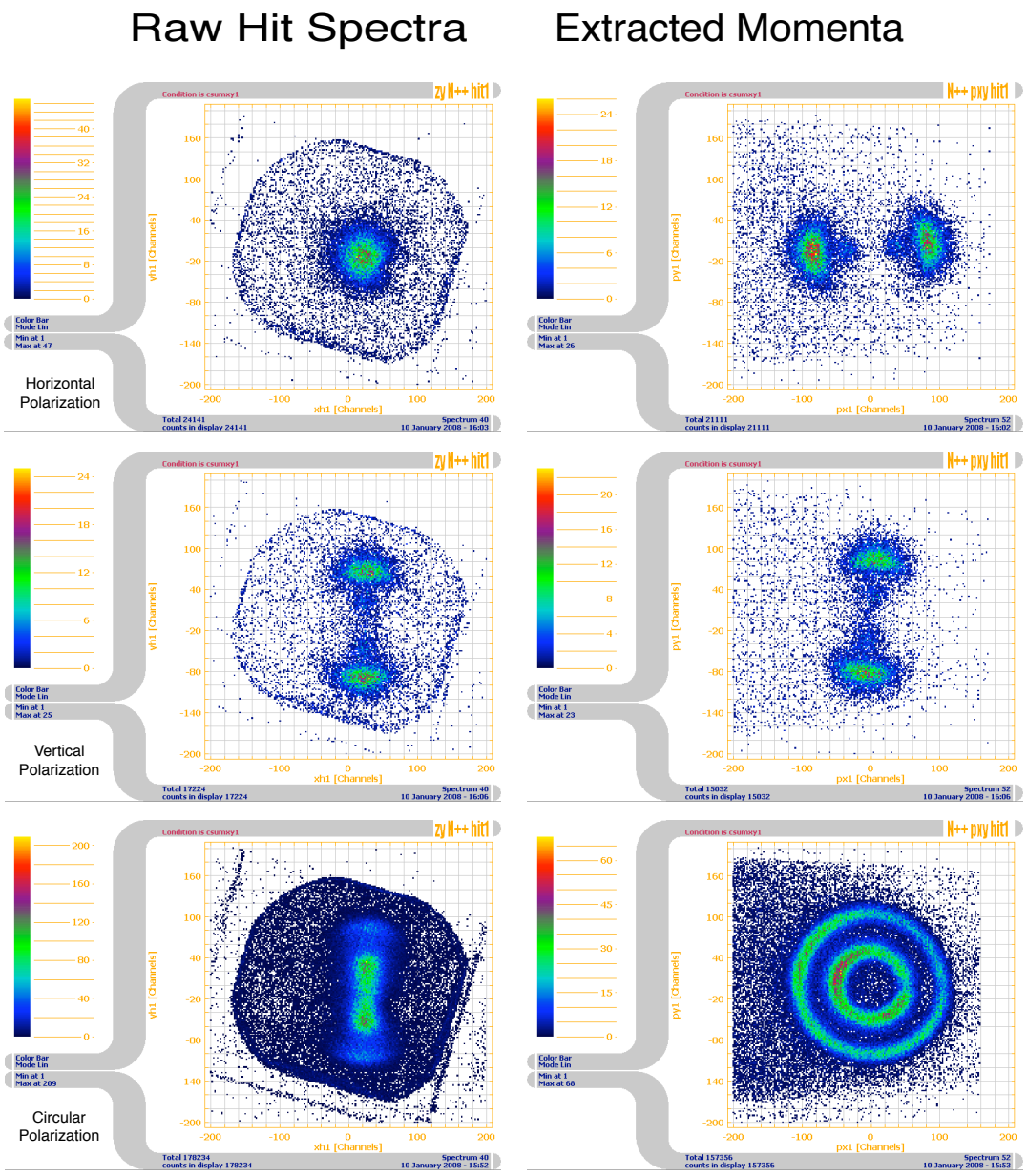

Figure 2.12: Example spectra from the CoboldPC software for a horizontally, vertically, and circularly polarized probe pulse. The fragments are N^{++} arising from the dissociation of N_2^{3+} (inner channel) and N_2^{4+} (outer channel). In the raw hit spectra (left), the noise background reveals that the delay line is tilted 16° relative to the lab frame, in order to diagnose detector problems independently from lab ones.

software also provides the option of controlling an external motor through the computer's parallel port. This feature is useful to precisely rotate the shaft of an AMS Model 6006 rotation stepper motor. Alternatively, it can control the precise position of a Burleigh Inchworm Motor stage to within 10 nm for data collection in a delayed pump-probe experiment.

Table 2.1: Laboratory equipment

	Chemistry Rm. 204 (Setup #1)	Physics Rm. 168 (Setup #2)
Laser Amplifier	Multipass Ti:Sapphire and Regen Ti:Sapphire 1 kHz	Multipass Ti:Sapphire 15 Hz
Pulse Characteristics	30 fsec @ 1.2 mJ per pulse 100 fsec @ 1.5 mJ per pulse	40 fsec @ 2.0 mJ per pulse
Pulse Diagnostics	PG FROG, SHG FROG, Single-Shot Autocorrelator	SHG FROG
Vacuum Hardware	Turbopumps, Ion Gauge, RGA	Turbopumps and Ion Gauge
Cooling	Liq. N_2 Cold Trap	Liq. N_2 Cold Trap and Molecular Beam Skimmer w/ pulsed valve
Molecules Used	N_2, O_2, CO	N_2, CO, HBr
Spectrometer	Single-stage TOF (10.2cm acceleration/18cm drift)	Single-stage TOF (5 cm acceleration/7 cm drift)
Detectors	'Z Stack' MCP and Helical Delay-Line Anode	Chevron MCP Pair
Electronics	Tektronix 2467B oscilloscope, SR250 Fast Integrator and Boxcar Averager, NIM Delay Generators and Logic Units, Time-to-Digital Converter	Tektronics 2440 oscilloscope
Software	TakeData and CoboldPC	DC (Data Collect)
Experiments	-Ionization Rate Anisotropy -Alignment Optimization -Dissociation Asymmetry	-HBr Polarizability Anisotropy -Dissociation Asymmetry

Chapter 3

Detecting Transient Alignment

3.1 Introduction

The previous chapter details the individual components used for the experiments. In order to detect the rotational behavior of diatomic molecules, many of these components must operate collectively, and the data must be filtered and interpreted before any claims about transient alignment can be made. This chapter details the two detection methods used in all the experiments for this thesis. Both methods incorporate what is known as pump-probe detection, where one laser pulse interacts with the system and loads the molecules into prepared states (in our experiments this is a wavepacket), and then a second, time-delayed probe pulse inspects the molecule over a range of time. The experimental layout is given in Figure 3.1. The first, quantitative, method uses the delay-line anode to precisely calculate the ensemble's macroscopic alignment once it has processed every fragment individually. While this can prove useful for some experiments, it can be prohibitively slow for others. It requires a small rate of fragment production, and requiring momentum coincidence between simultaneous hits further slows down the data acquisition rate. For

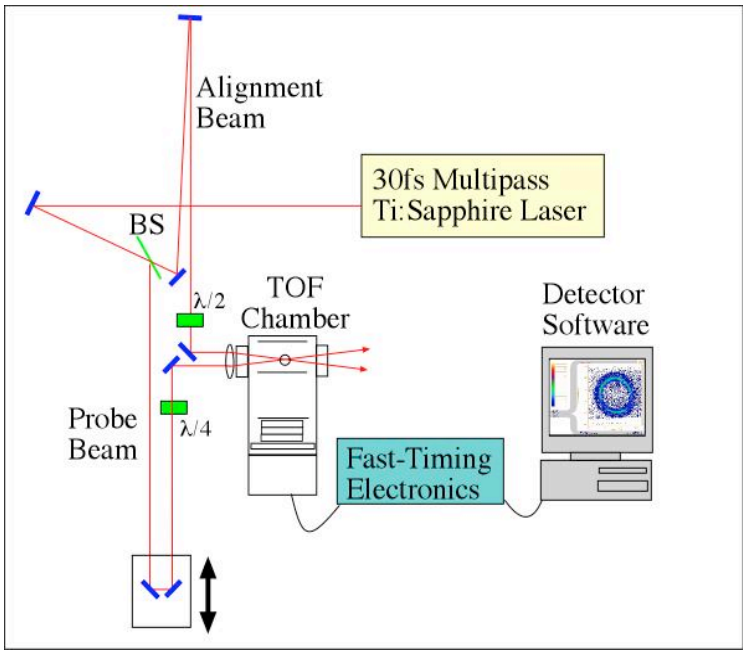

Figure 3.1: Typical experimental setup of a pump-probe alignment experiment.

applications where more rapid feedback is desired, a second qualitative method was employed to provide sufficient information to detect relative changes in molecular alignment. Following these method descriptions, the alignment degree in CO is compared to the alignment achieved by a rigid-rotor simulation with a constant anisotropic polarizability. The temperature of the ensemble is approximated by inspecting the dynamics from the coherently populated $|J\rangle$ states.

3.2 Experimental Method

3.2.1 Quantitative Detection Scheme

The position-and-time-sensitive detector allows us to explicitly determine the level of alignment in a molecular sample. We choose a circularly-polarized Coulomb-explosion pulse to

provide an unbiased probe of the field-free alignment within the polarization plane. The initial 3-dimensional momentum for every valid fragment event (the condition in Eq. 2.7) is extracted from the time-of-flight and DLA position information. From its momentum, the alignment parameter, $\cos^2\theta$, is calculated, where θ is the angle between the aligning laser's polarization and the intermolecular axis of the molecule prior to dissociation. The total alignment is evaluated from the ensemble average, $\langle\cos^2\theta\rangle$. Ensemble sizes of N > 2000 fragments are needed to have reasonable signal-to-noise.

Many experiments in the literature filter out all momentum hits which do not have a corresponding 2nd fragment with an equal and opposite momentum vector. While this significantly increases the signal-to-noise ratio, it also increases the data collection time. In order to avoid the onset of laser drift after several hours, we calculate $\langle\cos^2\theta\rangle$ from only the 1st fragment hit per laser shot (this is accomplished by inspecting only the "hit1" spectra). By adjusting the focal intensity of the exploding pulse or the gas pressure, the fragment count rate is adjusted to be approximately only one fragment detected for every 10 laser shots. The randomly detected fragment momenta for the "hit1" spectra therefore provide a good sampling of the full molecular angular distribution. By limiting data collection to only the first hits, we greatly improve the speed of data collection, but we are unable to draw any correlation between ionic fragments from the same parent molecule (because this would appear as a "hit 2" or greater within the same laser shot). To reduce noise even further, we limit our alignment evaluation to the fragments arising from a specific dissociation channel, or a single ring in the momentum space, as shown in Figure 3.2.

Inspecting the momentum "ring" in the polarization plane, we are able to adjust the laser ellipticity until it is nearly perfectly circular. A baseline data scan is taken for an unaligned sample with a large number of data points ($\sim$ 10000). Every fragment momentum is sorted into one of 360 angular bins, and this distribution is normalized to

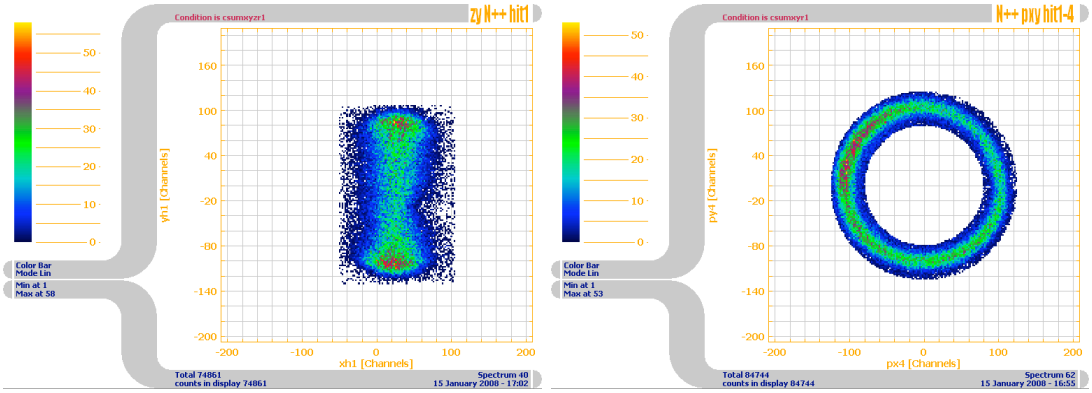

Figure 3.2: The noise filtering process when inspecting the alignment of one particular fragment species. This pair of plots illustrates the how one dissociation channel for nitrogen ($N_2^{4+} \rightarrow N^{2+} + N^{2+}$) is isolated using the Boolean operators in the CoboldPC software. The left plot contains the raw position information, and the right plot is the extracted momentum plot within the laser polarization plane.

have a value of $\langle \cos^2 \theta \rangle = 0.5$, which is the value for an isotropic distribution within the polarization plane. Delay-dependent changes in the angular distribution are measured relative to this baseline and are plotted against the probe delay. The DLA detector measures the angular distributions of N^{3+} for N_2, O^{3+} for O_2, and C^{3+} for CO. Fig. 3.3 demonstrates the form of the delay-dependent revival structures seen from this explicit method of calculating alignment.

At one of the alignment revivals, the alignment parameter typically fluctuates between two extrema. At the peak alignment, the 3-d angular probability function is distributed like a narrow cigar about the laser polarization axis. When the alignment parameter reaches its minimum, the angular distribution is a flat disc oriented along the plane perpendicular to the laser field axis. These features are visible from a measurement of the angular distribution within the polarization plane of the Coulomb explosion pulse, shown in Figure 3.4.

We also demonstrated the effect of ellipticity on the aligning pulse. A quarter-waveplate

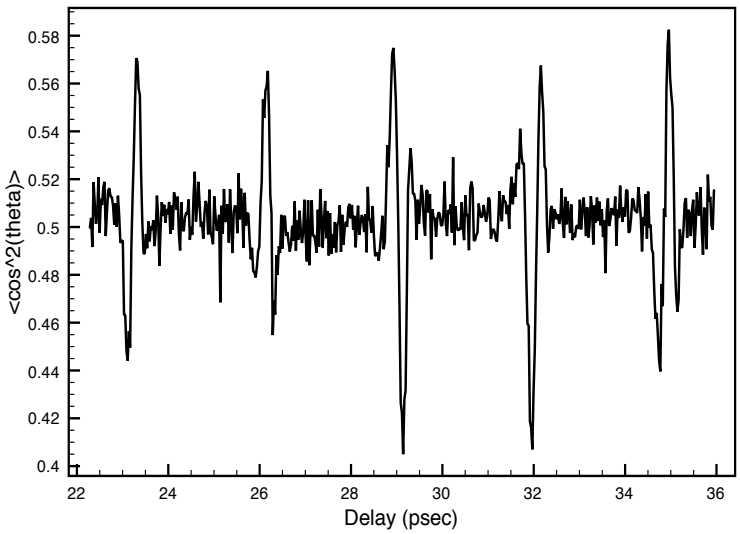

Figure 3.3: Quantitative alignment detection for one full rotational period of O_2. The fundamental rotational period, $T_1 = 11.5$ psec.

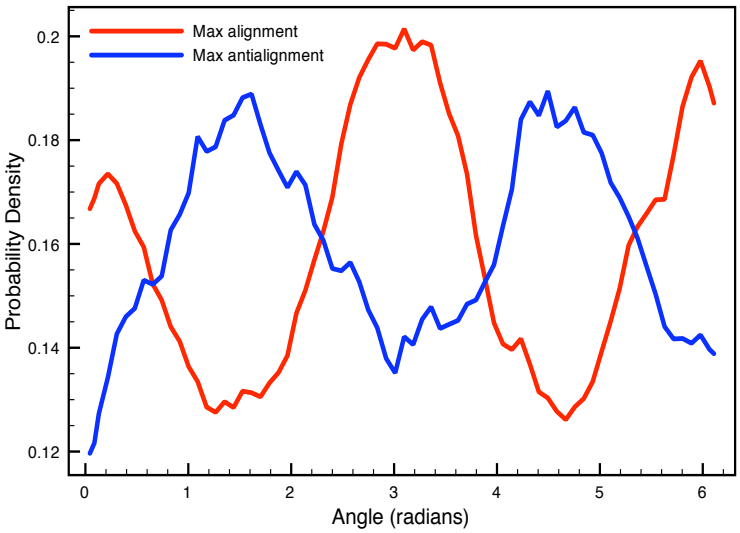

Figure 3.4: Angular distributions within the polarization plane at an alignment revival. At maximum alignment (and maximum antialignment) the molecular fragments exhibit clear alignment relative to the pump field axis.

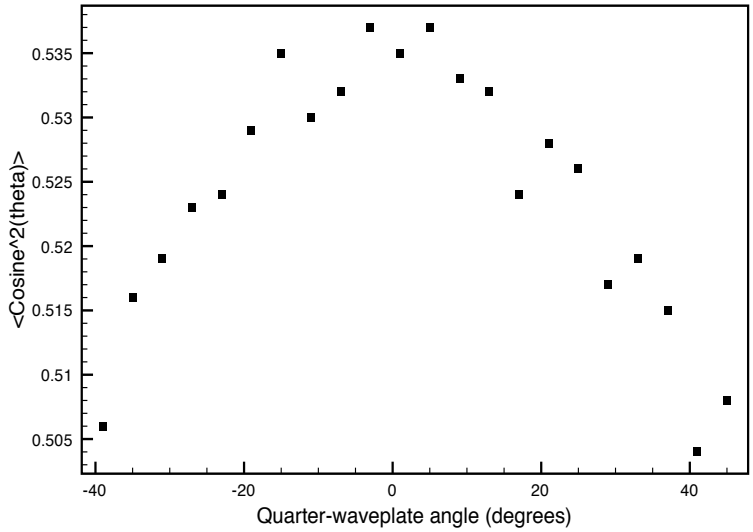

Figure 3.5: The ellipticity dependence of transient alignment. The aligning pulse traverses a quarter-waveplate, and the quantitative alignment is measured as a function of the waveplate angle. The alignment is relatively stable for a 15° total range, but then drops off rapidly as the waveplate approaches circular polarization (45°).

effected a polarization change on the pump beam, and the result is shown in Fig. 3.5. The alignment remains relatively constant over a small range of waveplate angles, but quickly drops off as the polarization becomes circular. This verifies the need to use an unbiased probe, although a small range of ellipticities about the circular polarization is acceptable for adequate alignment detection.

3.2.2 Qualitative Detection Scheme

Due to time limitations in the momentum extraction method, we employ a single-shot laser scheme to obtain a qualitative measure of alignment from the time-of-flight distribution of the ion fragments. Similar fragments (same m & q) which dissociate from molecules aligned perpendicular to the spectrometer axis have no initial velocity along the extrac-

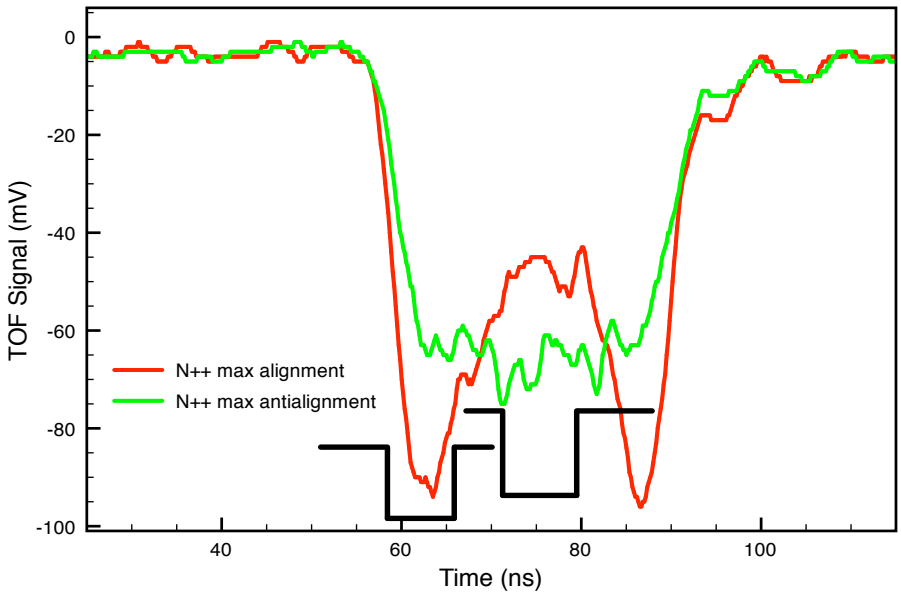

Figure 3.6: Illustration of the alignment dynamics which are visible in the time-of-flight spectrum. The gates are positioned to detect the approximate ratio of molecules parallel vs. perpendicular to the field. The two curves shown demonstrate the signal fluctuations observed at an alignment revival.

tion field. Therefore, these fragments reach the detector simultaneously and produce a single peak in the TOF spectrum. Conversely, molecules which are preferentially aligned along the spectrometer axis dissociate into ion pairs with initial velocities that are parallel and antiparallel, respectively, to the extraction field. This forward-backward velocity distribution generates a bimodal TOF feature that straddles the perpendicular alignment peak for each fragment species. Using the SRS boxcar integrator and a current-mode ion signal, we record the ratio R of the parallel dissociated ions to those ejected perpendicularly, as shown in Fig. 3.6. This method provides single-shot feedback of the macroscopic alignment in the sample with good signal to noise. The probe delay is swept over a range of several rotational periods, and the gate ratio (in Fig. 3.7) reveals the same temporal

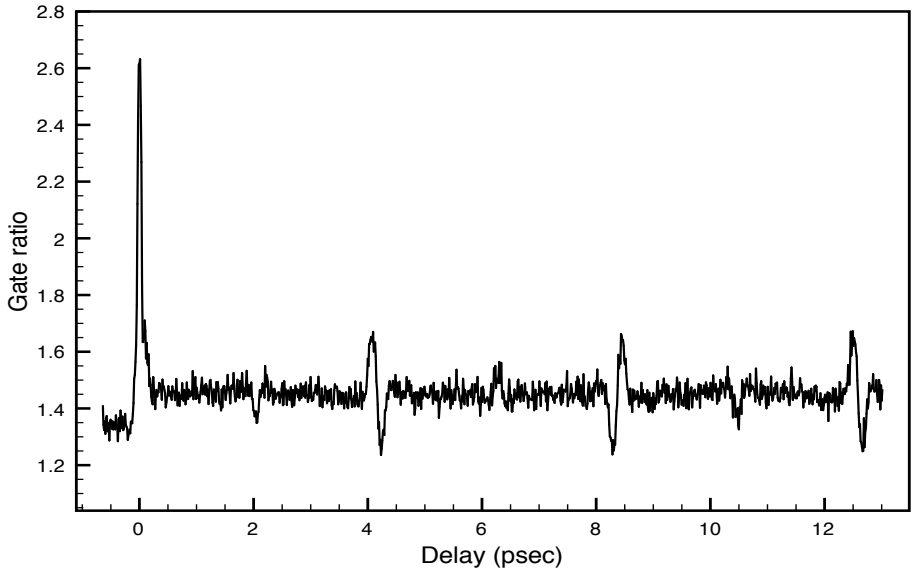

Figure 3.7: Qualitative alignment detection in N_2. The ratio provides a qualitative single-shot measure of molecular alignment as a function of time delay after the aligning laser pulses. Larger (smaller) ratios indicate preferential alignment parallel (perpendicular) to the alignment-laser polarization direction. The rotational period of nitrogen is $T_1 = 8.35$ psec, which arises as the 1st full revival. At roughly $\tau = T_1/2$ there is a half-revival present because alignment to an axis occurs twice within each full rotation of a diatomic. The baseline shift at $\tau = 0$ emerges from the time-independent incoherent alignment, which is described on page 55.

dynamics as those seen by the quantitative method on page 48.

3.2.3 Two-Pulse Alignment

With our alignment scans, we see that the degree of alignment improves as the pump intensity increases. Although it is possible to put more intensity into the aligning pulse, eventually the ionization and dissociation limits are surpassed. At this point, future experiments are performed not on the original neutral atoms, but on ions which generally have different electronic structures, as well as different equilibrium internuclear distances. It has been shown that trains of multiple ultrashort pulses can be used to maximize

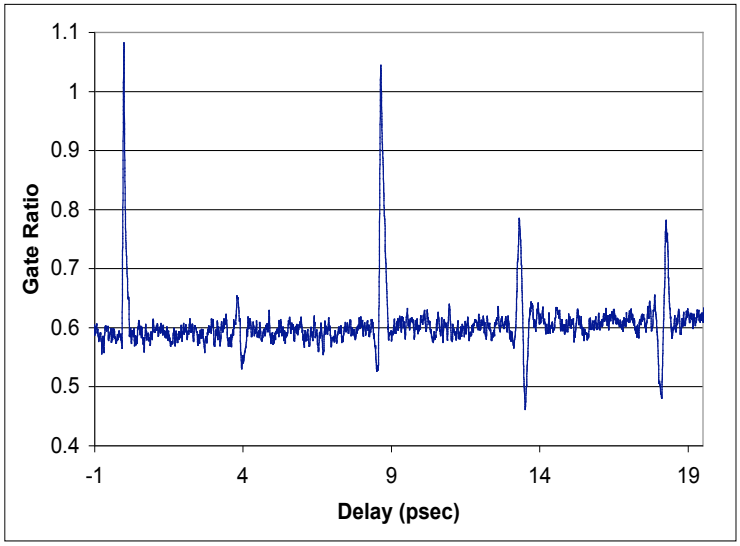

Figure 3.8: Enhancement due to a double alignment pulse kick in CO at the first full revival. The rotational period of CO is $T_1 = 8.64$ psec. Note that temporal overlap between the circularly polarized Coulomb explosion pulse and either of the alignment pulses results in enhanced ionization and a significant increase in the ion ratio.

the alignment degree while minimizing ionization [36, 55]. When subsequent laser pulses interact with the molecules near the alignment revivals, molecules which have only been weakly aligned the first time around are once again torqued to the same polarization axis, along with newly aligned molecules. The experiments performed in chamber #1 are near room temperature, and, with a single pulse, higher intensities are required to overcome the broad distribution of J-states present in the thermal ensemble. We therefore generate a double pulse for the alignment field, followed by the circularly-polarized probe pulse. The double pulse is made simply by incorporating another beamsplitter into the apparatus, so the total aligning pulse energy is roughly the same as before. The enhancement of the alignment degree is clearly visible in Figs. 3.8 and 3.9. Because the qualitative alignment detection method is so rapid, the revivals can be easily mapped out to the 30th

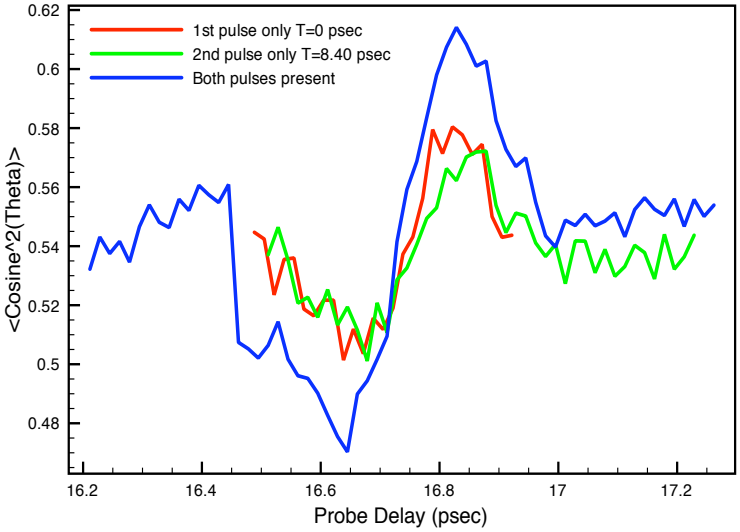

Figure 3.9: Measurement of the improved quantitative alignment with two pump "kicks".

(or greater) revival without any significant drift in the experimental conditions (see Fig. 3.10). At large delays such as this, the later revival structures exhibit extra temporal structure, arising from the centrifugal distortion of the molecule.

Focal Characterization

Immediately adjacent to the chamber, the spatial overlap of the laser beams and precise temporal delay between the three pulses is characterized by diverting the focusing laser beams through a 100-μ-thick β-barium borate (BBO) crystal. Sum frequency generation in the crystal is used to measure the cross correlations of the three laser pulses at their mutual focus. By translating the BBO crystal along the beam propagation direction we find that the longitudinal overlap region of the three beams is approximately 1/3 of the confocal parameter of the ionizing beam, as shown in Fig. 3.11. However, due to the highly nonlinear intensity dependence of ionization and/or dissociation rates for the molecules

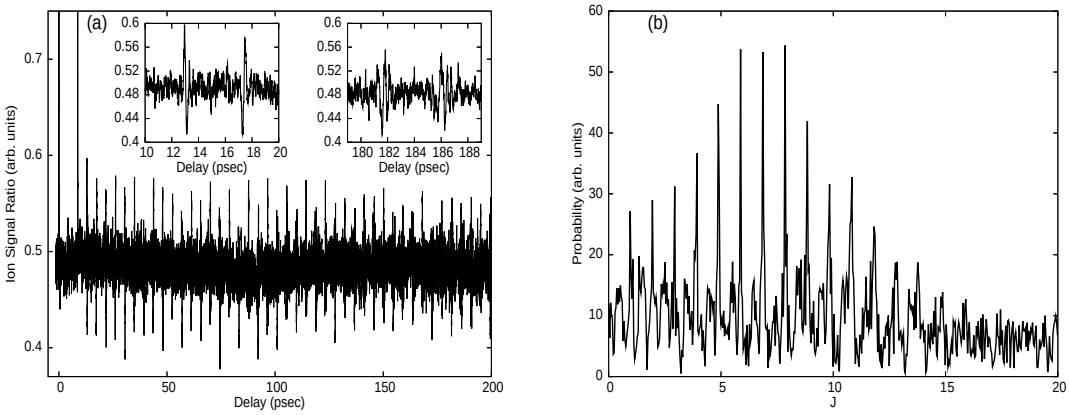

Figure 3.10: (a) Ratio of C^{3+} fragments traveling parallel vs. perpendicular to the TOF spectrometer axis following Coulomb explosion of laser-aligned CO molecules. The molecules are exposed to two 70 fsec, 10^{13}W/cm^2 alignment pulses that are linearly polarized along the spectrometer axis at t=0 and 8.664 psec, respectively. The insets show magnified views of the alignment-dependent ion ratio near the first and 20th half and full revivals following the second alignment pulse. The higher-order revivals are imperfect replicas of the first due to centrifugal distortion of the molecule. Comparison of the signal variations during the first half revivals immediately following each of the two alignment pulses again shows the significant improvement in alignment that is achieved by the addition of the second alignment pulses. (b) The squared Fourier transform of the revival structure in (a) identifies the J-states contributing to the rotational wave packet. The horizontal axis has been scaled from energy to J-value using the rigid-rotor energy differences.

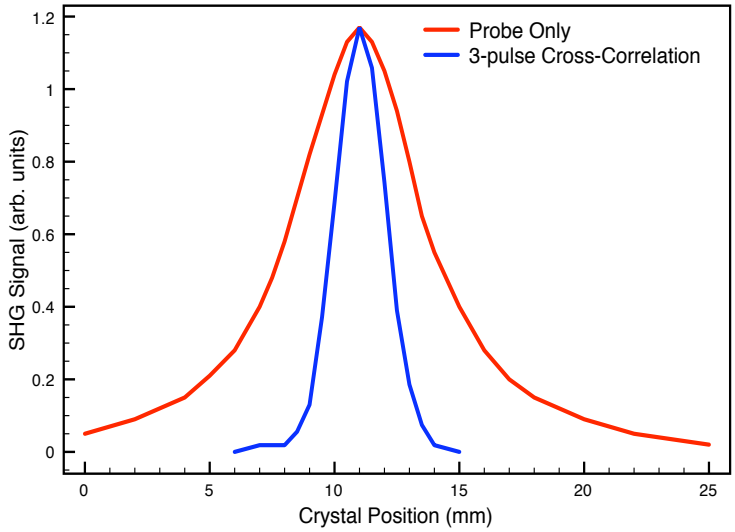

Figure 3.11: Focal characterization using the 100 μm SHG crystal outside the chamber. The red curve maps out the probe's longitudinal confocal parameter, and the blue curve represents the overlap signal between the probe and two pumps.

of interest, below the saturation intensity for a given ionization channel, ions are only produced at the highest intensities very near the center of the focus. Thus, the factor of 1/3 represents a lower limit on the fraction of aligned molecules that contribute to the ionization yield.

3.2.4 Revival Temporal Characteristics

Incoherent Alignment

As shown in Fig. 3.7 on page 51 with nitrogen, there is a noticeable baseline shift of the alignment signal around the $T = 0$ overlap delay. The laser-molecule interaction depends on θ, but not the azimuthal ϕ, so only the J populations are redistributed by the Raman excitations, while the m_j values are untouched. Initial populations have $|J\rangle$ states populated according to a Boltzmann distribution, with m_j values evenly spread

out for each $|J\rangle$. If the initial population is entirely in the $J = 0$ state, then the m_j values remain at 0 after the kick, resulting in a time-independent cigar-shaped angular probability distribution along the field polarization axis, known as incoherent alignment. The initial Boltzmann distribution washes out incoherent alignment, as there are higher initially populated m_j's. Laser impulses must be of sufficient intensity to populate high $|J\rangle$ states relative to the preexisting m_j, thereby creating the asymmetric angular probability distributions. Detecting this incoherent alignment with the qualitative method is also sensitive to the choice of boxcar-gate sizes and positions, so this feature does not appear in all of the alignment data plots in this report.

Nuclear Statistics

From the previous data in Figs. 3.3, 3.7, and 3.8, there is a noticeable difference between the revival structures within a full molecular rotation. These differences arise from the nuclear spin statistics of each molecule. As shown by Corkum *et al*, the even and odd $|J\rangle$ states in the wavepacket separately form oppositely-localized wavepackets at the quarter revival times, $T_1/4$ [5]. These opposing wavepackets cancel each other out, depending on the proportion of even to odd $|J\rangle$ states overall. This proportion can be evaulated by examing the entire molecular wavefunction.

The Born-Oppenheimer approximation decouples the various elements of motion (electronic, vibrational, rotational) within a diatomic molecule. This allows the complete diatomic wavefunction to be written as [56]

$$\Psi_{tot} = \Psi^{electron}\Psi^{vibrational}\Psi^{rotational}\Psi^{nuc.spin}\Psi^{elec.spin} \tag{3.1}$$

When a homonuclear diatomic molecule is rotated 180°, the nuclei (A, B) exchange posi-

tions, and the total wavefunction undergoes a change in parity given by

$$\Psi_{tot}(\mathbf{r}_B, \mathbf{r}_A) = (-1)^{\kappa+J+s+\pi}\Psi(\mathbf{r}_A, \mathbf{r}_B) \tag{3.2}$$

where κ is the nuclear spin symmetry parameter, J is the rotational quantum number, s refers to the symmetry of the electronic wavefunction relative to the plane containing the nuclei, and π arises from the inversion of the electrons relative to the nuclei. For the $^{16}O_2$ molecule, each nucleus is a spin-0 boson, therefore the Pauli principle requires that the total molecular wavefunction is fully symmetric under nuclear exchange, or

$$(-1)^{\kappa+J+s+\pi} = +1 \tag{3.3}$$

The ground state of O_2 is expressed as $^3\Sigma_g^-$. Here, "-" describes the symmetry of the electronic wavefunction, implying that $(-1)^s = -1$ or $s = 1$. The "g" indicates that the electron wavefunction is symmetric with respect to the inversion of of the electrons, and so $\pi = 0$. The total spin quantum number of O_2 is $I = 0$, so the nuclear spin parity constraint becomes

$$(-1)^{\kappa} = +1 \tag{3.4}$$

When these limitations are applied to equation 3.3,

$$(-1)^{J+1} = +1 \tag{3.5}$$

and therefore O_2 is limited to having only odd $|J\rangle$ states populated. The wavepacket produces transient alignment at the quarter-revival times, and there is no wavepacket from the even $|J\rangle$ states. Figure 3.3 on page 48 demonstrates these strong quarter-revival

features.

For the $^{14}N_2$ molecule, the ground state electronic wavefunction is labeled as $^1\Sigma_g^+$, which automatically determines $s = \pi = 0$ by an analogous argument to that of oxygen. The nuclei are both spin-1 bosons, and the total nuclear spin quantum number can be $I_{tot} = 0, 1$, or 2. Applying these constraints on equation 3.3 again will determine that for $I_{tot} = 0, 2$, the J values are even, and for $I_{tot} = 1$, only odd J's are allowed. Each possible nuclear spin state is $(2I_{tot} + 1)$-degenerate, and from nuclear statistics it follows that the ratio of odd:even $|J\rangle$ states is given by [33]

$$\frac{g_{odd}}{g_{even}} = \frac{I}{I+1}. \tag{3.6}$$

For nitrogen, this ratio is 1:2. This implies that the wavepacket quarter-revivals generated by the even $|J\rangle$ states are only partially cancelled out by the wavepacket from the odd $|J\rangle$ states. The quarter-revival structures are partially suppressed as a result, which is seen in Fig. 3.7 on page 51. For heteronuclear diatomics like CO, the Pauli conditions are not imposed, since identical nuclei are not exchanged after a 180° rotation. Therefore, even and odd $|J\rangle$ states are equally populated, and the quarter revivals are completely suppressed, as shown in Fig. 3.8 on page 52.

3.3 Results

3.3.1 Room Temperature

In this section we focus primarily on the level of alignment achieved with CO, in order to study its ionization rate anisotropy in chapter 4. We implement the double-alignment-pulse scheme described above for CO in Chamber # 1 in the Chemistry Lab, with the

second alignment pulse arriving 8.664 psec (approx. one full rotational period) after the first pulse. In spite of the fact that the molecules enter the chamber at room temperature, and the focused alignment beams do not fully overlap the probe volume, we are still able to detect alignment variations with both the qualitative and quantitative methods. After extracting the full 3-D momenta of the fragments, we observe a variation $0.31 \leq \langle \cos^2 \theta \rangle \leq 0.36$ between times of maximum parallel and maximum perpendicular alignment.

The degree of alignment we observe is consistent with a quantum simulation that models our CO sample as a thermal ensemble of nearly rigid rotors with a polarizability anisotropy $\alpha_0 = \alpha_{\parallel} - \alpha_{\perp} = 6.5$ (a.u.), where $\alpha_{\parallel}$ and $\alpha_{\perp}$ are the molecular polarizabilities parallel and perpendicular to the molecular axis, respectively [57]. Rotor eigenenergies are corrected for lowest-order centrifugal distortion, $E_J = B_0 J(J+1) - D_e J^2 (J+1)^2 (B_0 = 8.79 \times 10^{-6}$ a.u., $D_e = 2.79 \times 10^{-10}$ a.u.) and our numerical approach is nearly identical to one reported by Corkum *et al* in 2003 [5]. We utilize a second-order Runge-Kutta algorithm to solve the time-dependent Schroedinger equation for a rigid-rotor (two angular dimensions) under the influence of an induced dipole interaction potential, $V(\theta, t) = \frac{1}{4} F^2(t) \alpha_0 \cos^2 \theta$a.u., where F(t) is the combined electric field envelope for the two alignment pulses, and θ is the angle between the molecular axis and the alignment lasers' polarization direction. This procedure is outlined more in detail in Appendix A. The alignment pulses are assumed to be Gaussian with peak intensities, durations, and relative delays that match, within our experimental uncertainties, those used in the experiments. We compute, individually, the time-dependent angular probability distribution created from initial rotational levels $|\mathrm{J_0 M_0}\rangle$ that have thermal populations greater than 10^{-5}. These probability distributions are added to simulate the angular distribution of the ensemble. The Fourier transform of the time-dependent expectation value, $\langle \cos^2 \theta \rangle$ identifies the J-states in the coherent wave packet. The best agreement between the mea-

sured (Fig. 3.10b) and simulated (Fig. 3.12 inset) spectra is obtained by assuming an initial rotational temperature of 200K. This temperature is not unreasonable given the presence of the large liquid-nitrogen trap at the gas inlet to the chamber and the fact that the gas is being continuously pumped by a large-volume turbo. However, this choice is not critical, and similar results are obtained over a range of temperatures.

Assuming a rotational temperature of 200 K, very good agreement between the measured and simulated delay-dependent variations in $\langle \cos^2 \theta \rangle$ is obtained after the imperfect experimental overlap between the pump and probe beams is taken into account (see Fig. 3.12). The solid curve in Fig. 3.12 is computed under the assumption that half of the ionized molecules have been coherently prepared by exposure to the full intensity of the alignment beams while the other half of the ions originate from outside of the aligned volume. This estimate of a 50% aligned fraction is reasonable given the focal characterization and the nonlinear intensity dependence of the multiple-ionization process that is responsible for Coulomb explosion. This room temperature setup is exploited in the following chapter to examine the ionization rate anisotropy of CO.

3.3.2 Supersonic Molecular Beam Cooling

When the experiment is transported over to the physics lab to be used with a supersonic expansion molecular beam with skimmer, we attempt to extract the temperature attainable with CO. The optics setup is essentially the same, with a noncollinear pump-probe focal overlap within the interaction region. Without the position-sensitivity in the TOF spectrometer, we utilize the qualitative alignment method solely to determine the molecule's temperature. Due to the 15 Hz repetition rate, we only record the alignment dynamics of CO over one revival, seen in Figure 3.13. This gives us information regarding the spread of J-values within the rotational wavepacket. We compare the $|J\rangle$ state

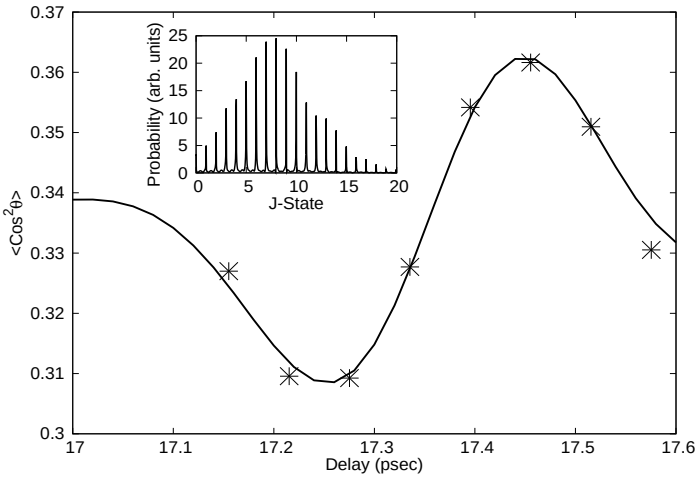

Figure 3.12: Variation in $\langle \cos^2 \theta \rangle$, over a range of delays near the second full wavepacket revival, for an ensemble of coherently prepared CO molecules. The delay scale is relative to the first of two alignment pulses and the laser pulse parameters are identical to those described in Figure 1. Data points (*) are extracted from the angular distributions of C^{3+} fragments obtained via Coulomb explosion of the CO molecules. The simulation calculated the angular distribution over the full 4π steradians. In order to match this with our data, the experimental values of $\langle \cos^2 \theta \rangle$ calculated within the polarization plane were extrapolated to the full angular sphere. The alignment process has cylindrical symmetry, so the planar alignment can just be rotated through the azimuthal angle, $P(\theta, \phi) = (1/2\pi)P(\theta)$ [6]. The solid curve is the result of a numerical simulation of the alignment as described in more detail in the text. The inset shows the simulated J-state composition of the angular wavepacket and should be compared with the experimental distribution shown in Figure 3.10b.

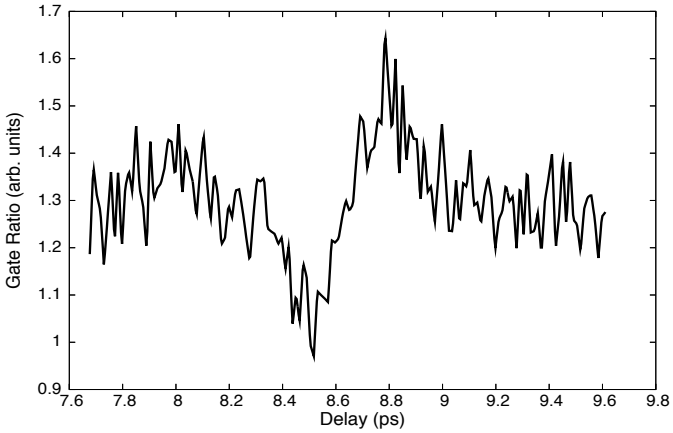

Figure 3.13: Transient alignment of CO cooled with a supersonically expanded gas jet.

envelope of a measured CO revival (Fig. 3.14a) with the $|J\rangle$ state distribution from the rigid rotor simulation (Fig. 3.14b). After visual comparison between the simulated J-state spectra, it is evident that the CO molecules have been cooled to 15 ± 5 K rotationally. Given the homebuilt nature of the skimmer, and the limitations of the turbopump capability in the skimmer region, it is not surprising that we don't get significantly more rotational cooling.

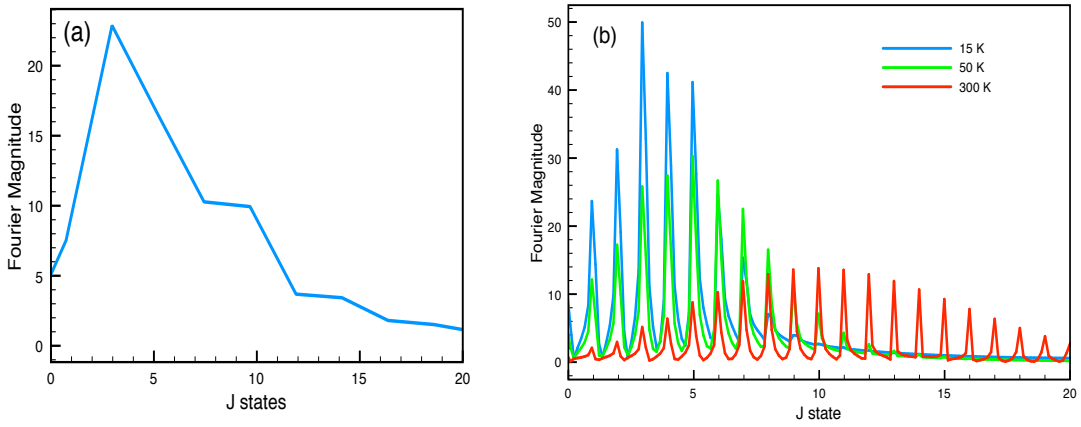

Figure 3.14: (a)The FFT J-state envelope of Fig. 3.13 is compared with (b) Fourier transforms of the rigid rotor dynamics simulation for a few rotational temperatures. Simulations between 10 K and 20 K produced $|J\rangle$ state spectra which aligned visually with the envelope seen in the left plot.

Chapter 4

Strong-Field Ionization of Transiently Aligned CO

4.1 Introduction

The availability of aligned rather than randomly oriented molecular samples now allows us to perform more sophisticated strong-field molecular physics experiments with higher precision. Understanding the ionization process is critical for the measurement of various complex phenomena, such as high-harmonic generation and tomographic imaging of molecular orbitals [8, 10]. Preparing partially aligned samples of molecules can significantly reduce the uncertainties associated with measurements of isotropically distributed molecules.

Regarding the ionization rates of some diatomic molecules, discrepancies still exist between theory and experiment [1–4]. The models generated so far have expressed the molecular strong-field ionization process as a quasistatic tunneling phenomenon as well as an interference between emitted electron waves. Recent calculations using time-dependent

density functional theory have also illustrated the ionized electron does not always originate from the highest-occupied molecular orbital (HOMO). This further verifies that the ionizing dynamics of molecules in strong fields requires continued study.

In this chapter, we explore transient alignment of CO with laser intensities near its ionization threshold. As described in chapter 3, the time-dependent angular distributions of the coherently prepared molecular samples are experimentally analyzed via Coulomb explosion of the molecules using an intense circularly polarized probe. We now utilize a less intense linearly polarized time-delayed ionization pulse for the probe and exploit the well-characterized temporal behavior of these rotational wave packets to measure the ionization yields of preferentially aligned CO molecules relative to Kr atoms. From these measurements, we extract an experimental determination of strong-field ionization rates in CO as a function of the relative angle between the ionizing field and molecular axis. Our results, including the coarse intensity dependence of the ionization anisotropy, are in qualitative agreement with the predictions of molecular orbital Ammisov-Delone-Krainov (MOADK) theory [3, 58].

4.2 Experimental Method

This experiment is performed in Chamber # 1 in the Chemistry Lab, using the output of the 30 fsec Ti:sapphire laser system. The amplified pulses here have energies as high as 1.6 mJ and are split into a probe pulse and two aligning-pump pulses. Instead of using a zero-order quarter-wave plate for the probe beam, a half-wave plate is incorporated, producing a probe beam that is linearly polarized parallel to the spectrometer axis, as well as to the aligning pulses. The probe beam intensity is also lowered from the high-intensity Coulomb-explosion regime (10^{15} W/cm^2) to a less intense single-ionization regime (10^{14} W/cm^2).

Iris diaphragms reduce the diameter of the alignment beams to approximately one-third that of the ionization beam. This ensures that the probe's focal volume is roughly 1/3 the size of either alignment beam. As detailed in section 3.2.3, the pump and probe beams cross at an angle of approximately 2° in the interaction region. The relative pump-probe delay is controlled with translation stages. A 30 cm, 2" diameter lens focuses the parallel, but noncollinear, laser beams into the TOF spectrometer.

4.2.1 Ratiometric Comparison

Precise measurements of atomic/molecular ionization rates are difficult to obtain because the ion yields vary nonlinearly with shot-to-shot laser pulse intensity fluctuations. DeWitt *et al* introduce a ratiometric technique of mixing a diatomic molecule with an atomic species with a similar IP [2]. Using this method, we leak a mixture of CO and Kr gas into the vacuum chamber for this experiment. CO and Kr have similar ionization rates over a range of intensities [1] and the alignment pulses have a negligible impact on the Kr ionization yield. By measuring the $[CO^+]$:$[Kr^+]$ yield ratios, we normalize out the influence of laser intensity fluctuations on the ionization signal at each delay.

Partial pressures of the two gases are measured with the SRS Residual Gas Analyzer. These must be corrected for 70 eV electron impact ionization cross sections (σ) to generate a true 50/50 mixture. The scaled partial pressure (PP) of a constiuent gas is given by

$$(PP)_{actual} = (PP)_{RGA}/\sigma \tag{4.1}$$

where $(PP)_{RGA}$ is the partial pressure measured by the RGA electron bombardment. An

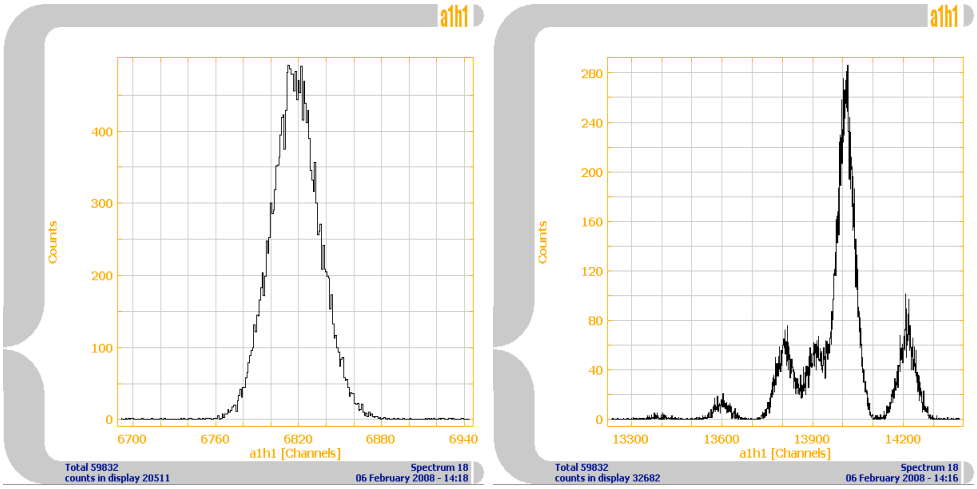

Figure 4.1: Ion spectra for CO+ (left plot) and Kr+ (right plot). The structure in the Kr+ spectrum arises from the abundance of the different isotopes of Kr. The x-axis is measured in Cobold channels, which each correspond to 0.5 nsec of ion time-of-flight.

even mixture is obtained by balancing the formula

$$\frac{(PP)_{CO}}{(PP)_{Kr}} = \frac{(PP)_{CO,RGA}}{\sigma_{CO}} \Big/ \frac{(PP)_{Kr,RGA}}{\sigma_{Kr}} \tag{4.2}$$

where the cross sections for CO and Kr are available from the literature ($\sigma_{CO} = 1.73$ Å^2 and $\sigma_{Kr} = 4.2$ Å^2) [59, 60].

We count the two separate ion species simultaneously with the CoboldPC software, exploiting the 15-hit detection capability of the apparatus. Typical ion spectra are shown in Fig 4.1. By counting the two separate ion species simultaneously with the CoboldPC software, we detect their relative ionization rates. We record the ionization yield over a range of delays spanning the maximum parallel (along the laser polarization) and perpendicular (in a plane normal to the laser polarization) alignment times during the first full revival after the second alignment pulse. Any delay-dependent changes in the [CO]:[Kr] ionization ratio indicate an alignment sensitivity in the CO ionization rate.

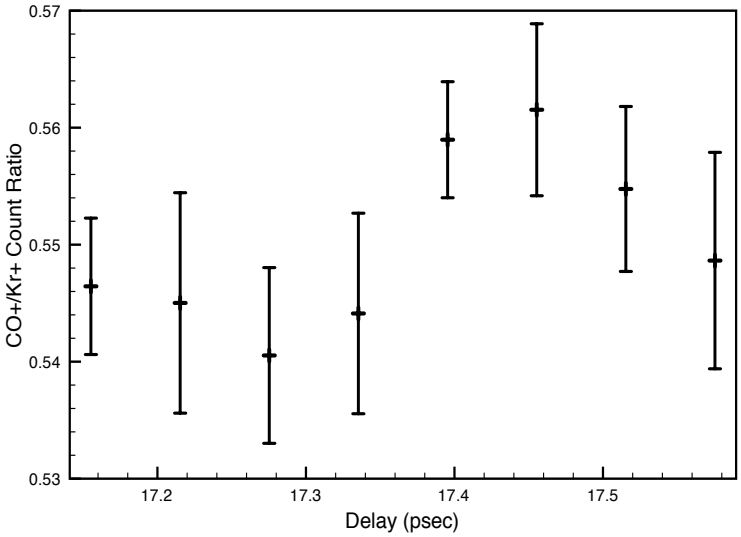

Figure 4.2: Variation in the $[CO^+]$:$[Kr^+]$ ionization yield ratio as a function of delay between the alignment and ionization pulses. The data points are the mean values of 13 different measurement sets and the error bars reflect the standard deviations of those measurements.

4.3 Results

The alignment phenomenon is clearly visible in the ratiometric data scans. The data points shown in Fig. 4.2 are the averages of 13 different measurement sets collected on six different days under essentially identical conditions. We find that the average value $\langle R \rangle$ of the CO:Kr ionization-rate ratios obtained at maximum parallel and perpendicular alignment times is equal to the rate ratio for an unaligned sample, $R_0 = 0.55$. This is in agreement with the previous measurement taken by Wells *et al*, where they found that the average ionization rate ratio between the two species was ~ 0.5 over a wide range of intensities [1]. Accordingly, systematic errors caused by small changes in the relative partial pressures of Kr and CO for different data sets are eliminated by individually normalizing each data set such that $\langle R \rangle = 0.55$. Analogous measurements were also

made for ionizing laser intensities a factor of 1.14× lower and 1.25× higher than those used to obtain the data show in Fig. 4.2. Within the experimental error bars, the rate ratios at lower intensity are identical to those in Fig. 4.2. However, significantly reduced (3× smaller) variations are observed at higher intensities.

4.4 Discussion

The relatively small delay-dependent variation in the measured ionization yield ratios can be attributed to the limited macroscopic alignment achieved in the experiments. This is due, primarily, to the high initial rotational temperature of the sample and the imperfect spatial overlap between the pump and probe beams. Nevertheless, our detailed Coulomb explosion measurements enable us to extract the functional form of the angle-dependent ionization rate P(θ) for CO. Specifically, P(θ), or any positive definite θ-dependent observable with symmetry about $\theta = \pi/2$, can be expanded in moments $\langle \cos^{2N}\theta \rangle$ of the molecular angular distribution for N=0, 1, 2, ... These moments are evaluated based on the extracted momenta from the molecular fragment distribution at the 2nd full revival (see Fig. 4.3). The delay-dependent ionization yield ratio is therefore expressed as

$$R(t_i) = \sum_{N=0}^{\infty} \alpha_N \langle \cos^{2N}\theta \rangle_i \tag{4.3}$$

This can alternatively be written as

$$\vec{R} = \mathbf{M}\vec{\alpha} \tag{4.4}$$

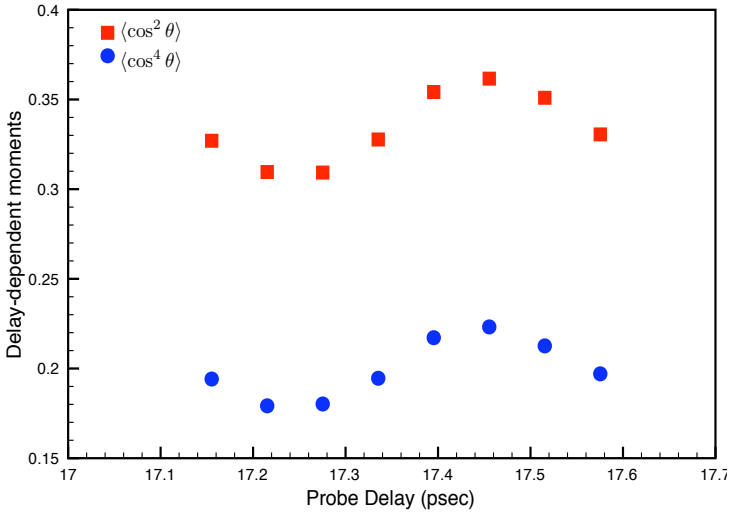

Figure 4.3: Plot of the first two delay-dependent moments extracted from the delay-line fragment momenta (not counting the N=0 term).

where $\mathbf{M}$ is the full array of N moments evaluated at each delay. From this, it follows that

$$\begin{aligned} \mathbf{M}'\mathbf{M}\vec{\alpha} &= \mathbf{M}'\vec{R} \\ \vec{\alpha} &= (\mathbf{M}'\mathbf{M})^{-1}\mathbf{M}'\vec{R} \end{aligned} \tag{4.5}$$

where $\mathbf{M}'$ is the transpose of $\mathbf{M}$.

This produces the least-squares fit of the measured ionization yield ratios to the delay-dependent moments obtained from the experimental CO distributions. This best fit is shown in Fig. 4.4 overlaid onto the previous data. We find that the χ^2 value for the fit is not improved by including terms beyond N=0, 1 in the expansion in Eq. 4.3. Thus, the best-fit function has the form $P(\theta) = A + B\langle\cos^2\theta\rangle$, with A=0.43 and B=0.36. From this expression, we obtain the ionization anisotropy for molecules aligned parallel or perpendicular to the ionizing field, $P_\parallel/P_\perp = 1.9 \pm 0.6$, by setting $\langle\cos^2\theta\rangle$=1 and 0 for $P_\parallel$

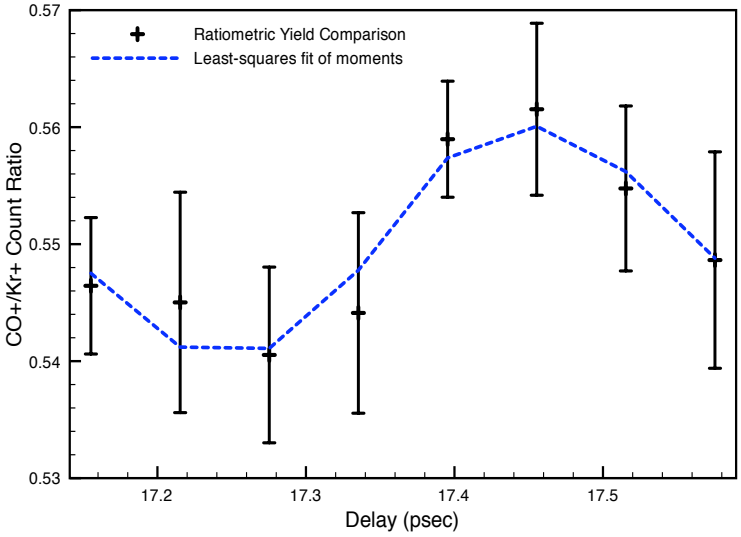

Figure 4.4: Variation in the $[CO^+]$:$[Kr^+]$ ionization yield ratio from Fig. 4.2. As described in the text, the dashed curve is a fit to the data in terms of measured delay-dependent moments $\langle \cos^{2N} \theta \rangle$. Specifically, we find that the angle-dependent ionization ratio has the form $P(\theta) = 0.43 + 0.36 \langle \cos^2 \theta \rangle$.

and $P_\perp$, respectively.

Our ionization measurements are in qualitative agreement with recent theoretical results based on a molecular-orbital ADK tunneling (MOADK) model [58, 61]. For ionization with low-intensity 8 fsec, 800-nm laser pulses, the MOADK calculations predict an ionization anisotropy $P_\parallel/P_\perp = 4.7$. This value is nearly constant for intensities up to 8×10^{13} W/cm^2 but then decreases rapidly with increasing intensity such that $P_\parallel/P_\perp \simeq 3.4$ and 1.5 at 1.6×10^{14} and 3.2×10^{14} W/cm^2, respectively [58]. More generally, $P(\theta)$ has a functional dependence which is indistinguishable from $A + B\cos^2\theta$ for intensities above 10^{14}W/cm^2, with only a slight variation from this form at lower intensities. The prediction of a constant ionization anisotropy at low intensity and nearly isotropic ionization rate at higher intensities is consistent with our results. While our measured value $P_\parallel/P_\perp \simeq 1.9$ is approximately a factor of 2 lower than predicted for an intensity of 10^{14}W/cm^2, quantitative agreement is obtained if we increase our experimental intensity estimate by a factor of 2. Another possible source of the discrepancy is the MOADK approximation itself. We note that for 100 fsec, 800 nm pulses, MOADK calculations underestimate the $[CO^+] : [Kr^+]$ yield ratio by a factor of 2.5 [3]. In addition, while the change in molecular alignment during an 8 fsec ionization pulse should be negligible, our Coulomb explosion measurements indicate that partial alignment does occur during our 30 fsec ionization pulses. Thus, we expect that the theoretical predictions for 8 fsec pulses will overestimate the ionization anisotropy for the 30 fsec case.

4.5 Conclusion

In conclusion, we have prepared aligned samples of CO to probe their inherent properties. The preferentially aligned targets have been used to determine, for the first time, the

angular dependence of the ionization rate for CO molecules exposed to 30 fsec, 780 nm laser pulses. We find that below the saturation intensity, the ionization probability is two times larger for molecules aligned parallel rather than perpendicular to the laser polarization direction. These results are in qualitative agreement with MOADK predictions.

Chapter 5

Polarizability Anisotropy of HBr

5.1 Introduction

The alignment phenomenon is a useful tool for probing properties of diatomic molecules. As described previously, it enables the measurement of the alignment-dependence of the molecular tunneling-ionization probability. We now show how it can be used to extract the polarizability anisotropy $\Delta\alpha$. This quantity expresses how easily the molecule's electronic cloud is distorted by an applied electric field. It is a quantity for which accurate measurements are not always available in the literature.

$\Delta\alpha$ has wide-ranging usefulness in molecular physics and has been extensively studied in the last few decades. It determines the relative intensities of rotational Raman transitions, plays an important role in the evaluation of intermolecular forces, and is required for the calculation of molecular quadrupole moments [62]. Typically this anisotropy is calculated using an *ab initio* quantum chemistry tool known as the Hartree-Fock method, which is a version of the quantum mechanical variational principle that accounts for the exact interactions between the electrons and nuclei, and approximates the interactions be-

tween electrons [56]. Of particular relevance to the measurements reported here, Bishop and Norman have applied this technique to calculate values of $\Delta\alpha$ for the hydrogen halides [63].

Experimentally only a few techniques have been employed to measure the polarizability anisotropy in diatomic molecules. One of the earliest methods involved molecular-beam electric-resonance spectroscopy, in which molecular energy level transitions are studied at a fixed rotational level [64]. Johnson and Ramsey examined the Stark hyperfine structure of DBr and were able to express the anisotropy as a function of the Stark parameter [65],

$$\alpha_{\parallel} - \alpha_{\perp} = \frac{3\mu_{\nu}^2(X_1 - X_2)}{4hB_{\nu}(3X_1 - X_2)}, \;\; X_J \equiv \frac{\mu_{eff}^2 E_{dc}^2}{hB_{\nu}} \tag{5.1}$$

where B_ν is the rotational constant and μ_{eff} is an effective dipole moment which depends upon the rotational quantum number. They concluded that more work was necessary to account for a significant discrepancy between two independent measurements (results tabulated on page 87). We note that this measurement of the polarizability arises from the direct coupling of adjacent rotational states by a static electric field, whereas the coupling of rotational states leading to alignment arises from nonresonant rotational Raman transitions at optical frequencies.

With this in mind, another way to extract $\Delta\alpha$ experimentally is by studying the rotational behavior of the diatomic species under the influence of a laser field. This can be accomplished by a direct analysis of the rotational Raman transition intensities [66]. Another method, closely related to the technique described here, was recently demonstrated by Sakai *et al.*[67]. They inferred values for $\Delta\alpha$ from the maximum degree of achievable *adiabatic* alignment. We demonstrate that comparing the *transient* alignment efficiency of a diatomic species with a known $\Delta\alpha$, to that of other diatomic species with unknown

$\Delta\alpha$, is an effective way to determine the unknown anisotropies.

In our method, we inspect the temporal alignment dynamics using the single-stage TOF spectrometer, and we compare the revival structures of transiently aligned HBr, with those of our reference molecule N_2. Sakai *et al.* also utilized a reference molecule, I_2, when evaluating the alignment in rare gas dimers. We employ identical 40 fsec, 800 nm laser pulses to dynamically align the N_2 and HBr molecules. We utilize a rigid-rotor simulation combined with a χ^2 fitting routine, to extract the temperature and aligning pulse intensity from N_2 data, using the accepted value of $\Delta\alpha_{N_2}$. We then use this intensity determination in an analogous fit of the HBr alignment data, to extract $\Delta\alpha_{HBr}$ and the HBr beam temperature.

5.2 Experimental Method and Data

This experiment is performed in Chamber #2, with the supersonically expanded gas jet of HBr and N_2 molecules. The optics are again setup to perform a temporally-delayed pump-probe experiment, using a $\lambda/4$-waveplate to generate a circularly-polarized, unbiased probe. The pump and probe beams' foci are overlapped noncollinearly in the TOF extraction region. The near transform-limited pulse duration from the laser amplifier was measured to be 40 fsec with the SHG FROG apparatus. The spacing between the compressor gratings were adjusted to provide sufficient negative-GVD to the laser pulse so that its duration nears its transform-limit in the interaction region within the chamber (having passed through all optical components). This is accomplished by observing the single-ionization yield of N_2^+, and maximizing the ionization signal with the shortest possible pulse (highest intensity).

We utilize a gas mixture of 3% HBr-in-helium which enters the spectrometer through

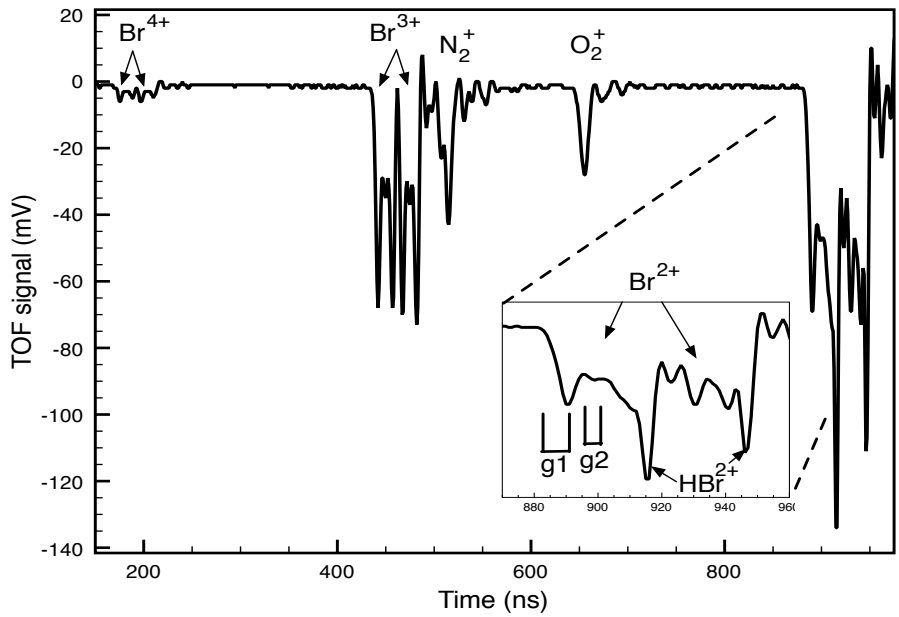

Figure 5.1: Time-of-flight spectrum for HBr gas with circularly polarized probe light. The isotope pair can be seen in all of the charge states. The inset illustrates how the gates were positioned to detect alignment qualitatively from the $^{79}Br^{2+}$ fragments.

the pulsed, skimmed, supersonic expansion described in section 2.3.4. The helium serves as a buffer gas which removes kinetic energy from the HBr molecules via collisions. Bromine has two stable isotopes, ^{79}Br and ^{81}Br, which are roughly equal in abundance. This results in isotopic pairs of peaks for every dissociation channel in the TOF spectrum, as seen in Fig. 5.1. For better resolution, we study the $^{79}Br^{2+}$ fragments arising from the dissociation of $(^{1}H^{79}Br)^{3+}$.

This chamber does not have a position sensitive detector, so all of the data are extracted from the TOF signal. We use the qualitative alignment detection method from section 3.2.2, to detect the delay dependent changes in the amount of parallel/perpendicular exploded fragments. The Data Collect program generates custom gates to overlap with the

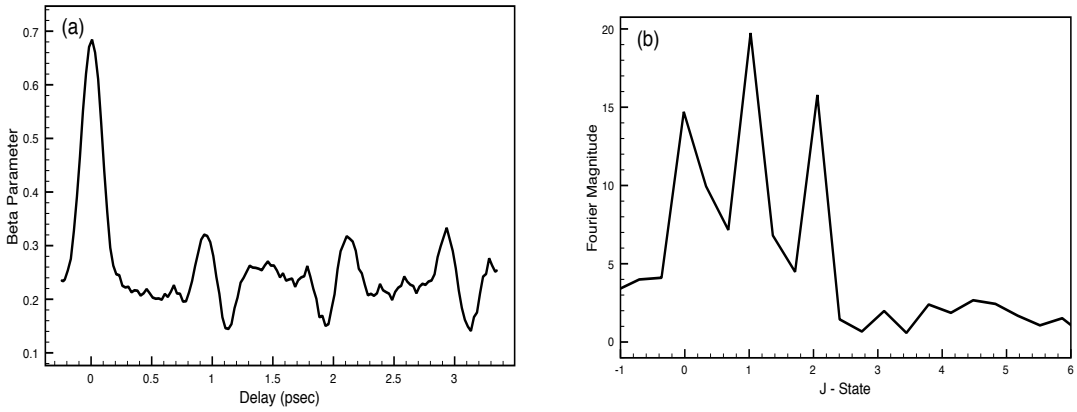

Figure 5.2: (a) Qualitative alignment scan of HBr at a source pressure of 80 psi. The full rotational period of HBr is $T_1 = 1.99$ psec. Its corresponding coherently populated $|J\rangle$ states are plotted in (b).

TOF spectrum, and it precisely steps the Burleigh inchworm motor (delaying the probe pulse) for each successive measurement. The probe is a circularly-polarized Coulomb-exploding pulse as in the previous chapters. One gate is placed at the edge of the $^{79}Br^{2+}$ peaks (shown in the Fig. 5.1 inset), and another is placed in the center. For analysis, we define a parameter β, where

$$\beta = \frac{gate_1 - gate_2}{gate_1 + gate_2}. \tag{5.2}$$

This has the advantage of being a bound function (unlike a simple ratio, which becomes erratic for small signal sizes).

The characteristic revival structure for HBr emerges as the probe is stepped through several picoseconds of delay. The rotational period for the ground vibronic state is 1.99 psec, as seen in Fig. 5.2a. The coherently populated $|J\rangle$ states for the alignment are shown in Fig. 5.2b. Only 3 states are significantly populated (compared to the CO results seen previously), as the molecular beam & skimmer apparatus helps to rotationally cool the

molecules. Also, the rotational energy levels of HBr ($\sim B_0 J(J+1)$) are separated roughly $4\times$ farther apart than the corresponding J-values in N_2 or CO, so the initial thermal distribution is restricted to low J.

5.3 Analysis

We utilize the rigid-rotor alignment simulation to evaluate our results. As the qualitative alignment detection scheme does not explicitly calculate $\langle \cos^2\theta \rangle$, we modify the output of the simulation to model the gates and also to generate the resultant β value. The approximated "gates" are formed by integrating over the angular probability distribution over angle ranges which correspond to the gate widths used by the Data Collect software. We seek to find the combination of laser intensity, rotational temperature, and $\Delta\alpha$ for the simulation that best mimics the temporal alignment dynamics.

5.3.1 Intensity Calibration from N_2 Alignment Data

The laser-molecule interaction term is expressed as $V(\theta, t) \propto I(t)\Delta\alpha \cos^2\theta$. Selection of the optimal anisotropy depends directly on the choice of peak laser intensity, as they both factor into the interaction term equally. We therefore utilize alignment scans for nitrogen, a molecule whose anisotropic polarizability is well-documented in the literature ($\Delta\alpha = 4.67$ a.u.) [62, 66, 68], to determine the alignment laser intensity used to acquire the HBr data.

The output from the rigid rotor simulation, f(t), is first overlaid with the experimental data, y_t. This is accomplished by subtracting off a linear fit term from both data sets (which centers both plots about y=0) and scaling their maximum value to y=1. This preserves the temporal revival structure, so that the simulation may be overlapped on

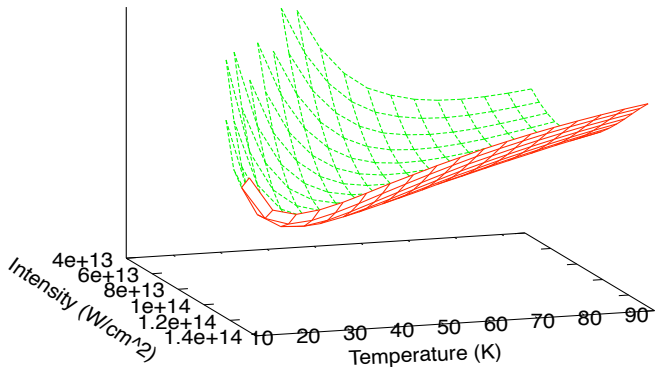

Figure 5.3: χ^2 fitting surface for nitrogen alignment data. The x- and y- axes are the initial parameters input into the rigid rotor simulation for nitrogen.

equal footing with the experimental data. This data/theory comparison process is shown (for N_2 and HBr) in Figs. 5.5 and 5.7.

The goodness-of-fit is measured by

$$\chi^2 \equiv \sum_t \left(\frac{f(t) - y_t}{\sigma_t} \right)^2 . \tag{5.3}$$

where σ_t is the standard deviation of the measured β parameters at a particular pump-probe delay. A typical χ^2 surface for N_2 is plotted as a function of the intensity and temperature parameters in Fig. 5.3. Values for laser intensity and rotational temperature are obtained from the minimum of the surface.

We observe that the best intensity fit for the nitrogen alignment scans is $I = 1.05 \times 10^{14}$ W/cm^2 with a rotational temperature of 35K. This extracted intensity is reasonable given the measured average power and beam focusing characteristics. With a 35 cm lens, and

assuming a perfect Gaussian-profile beam, the pump laser beam has an upper intensity limit of $\sim 2 \times 10^{14}$ W/cm^2. The actual intensity could easily be 2 $\times$ smaller than this maximum due to non-Gaussian features in the beam, lens aberrations, and the possibility that the probe could be fragmenting molecules at a location away from the pump beam waist.

Quantifying the goodness-of-fit for χ^2

In order to quantify our fitting method, appropriate error bars need to be placed on the parameters of interest. We define a confidence region based on constant-χ^2 cuts through the fitting surface [69]. Parameter sets which place χ^2 beneath a given confidence level are indicative of an optimal fit. To quantify these confidence levels, so we incorporate a statistical tool known as the F distribution [70]. F is defined as

$$F = \frac{\chi^2_{\nu_1}}{\chi^2_{\nu_2}} \tag{5.4}$$

where $\chi^2_\nu = \chi^2/\nu = \chi^2/(N-m-1)$ is the reduced χ^2 value, and N is the number of data points, and m is the number of fitting parameters. The F distribution is given by

$$P_{_F}(F,\nu_1,\nu_2) = \frac{\Gamma(\frac{\nu_1+\nu_2}{2})}{\Gamma(\frac{\nu_1}{2})\Gamma(\frac{\nu_2}{2})}\left(\frac{\nu_1}{\nu_2}\right)^{\nu_1/2}\frac{F^{\frac{1}{2}(\nu_1-1)}}{(1+F\nu_1/\nu_2)^{\frac{1}{2}(\nu_1+\nu_2)}}. \tag{5.5}$$

It determines when a variation between two χ^2 calculations is statistically significant.

For nitrogen, we evaluate the F-values as the ratio of χ^2 between the minimum of the fitting surface and everywhere else on the surface, and with ~ 100 data points and 2 fitting parameters (intensity and temperature). The intersections of constant-χ^2 planes with the fitting surface form ellipses over the fitting parameters. We utilize the following confidence

levels which determine the likelihood that the "true" parameter set falls within the given boundary: 68% (one standard deviation), 80%, 90%, 95%. The confidence limits are each equated to the F probability distribution P_F, and the limiting F value is extracted. From F, the constant χ^2 ellipses are quantified, as shown in Fig. 5.4. Error bars in the parameters can be drawn by taking the projection of the confidence-limit ellipses onto either parameter's axis.

Adequacy of fitting technique

Given the crossing intersection between pump and probe beams, it is possible that the alignment data are obtained over a range of alignment intensities throughout the overlap region. One might even question the utility of defining a laser intensity. Therefore, we need to determine if the shallow curvature along the intensity coordinate near the minimum in the χ^2 surface is characteristic of the alignment itself, or is the result of an effective range of alignment intensities in the experiments. To this end, we compare the χ^2 surface obtained from the experimental data with one constructed, numerically, at a single laser intensity. At temperatures near 30 K, the fitting routine finds the absolute best fit to the constructed data with $\chi^2 = 0$, but there is a significant breadth about the minimum along both axes (comparable to the uncertainties seen in Fig. 5.4). Only when the rotational temperature (used to create the numerical data) falls below 10 K does the fitting routine find a more sharply defined minimum. Thus, it appears that the extraction of parameters from the fit is not limited by the experiment.

5.3.2 $\Delta\alpha$ Calibration from HBr Alignment Data

The χ^2 fitting routine is then applied to HBr alignment data obtained at a gas source pressure of 100 psi. The best intensity extracted from N_2 is held fixed in the simulation,

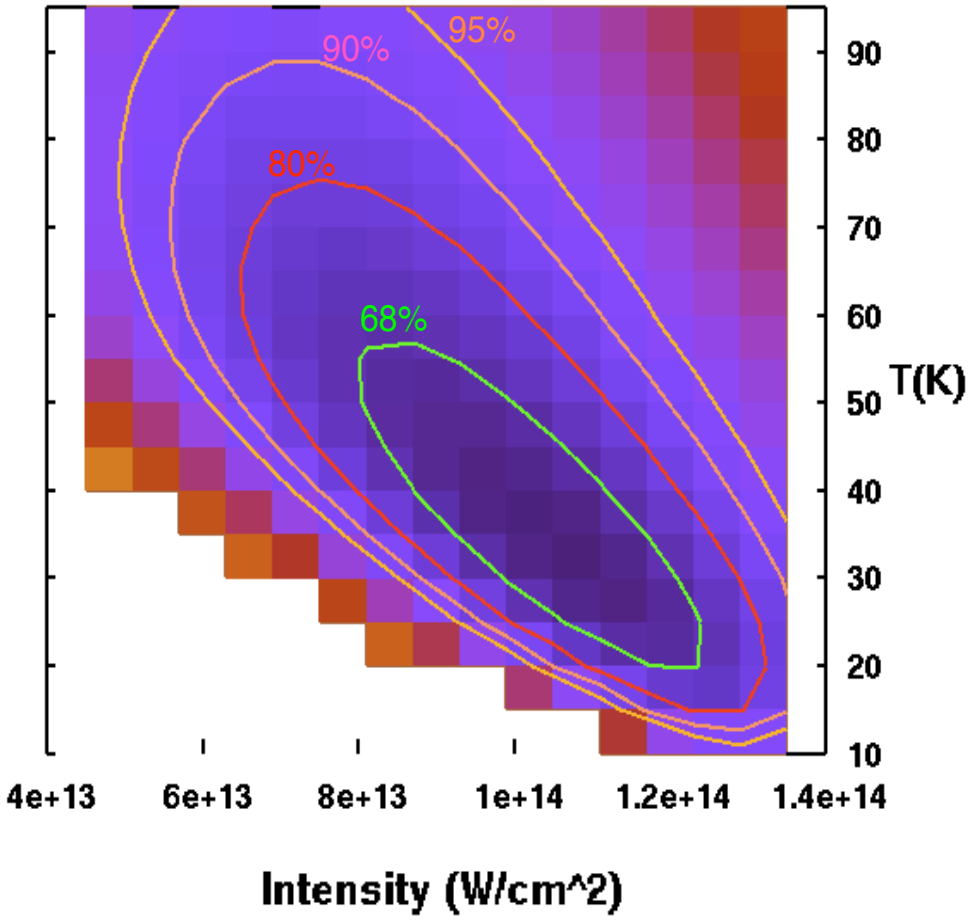

Figure 5.4: Confidence limits on the χ^2 fitting routine for the N_2 alignment data. Ellipses drawn represent the confidence boundaries and are estimators for the likelihood that the true parameter set lies within the enclosed area. Error bars in the individual parameters can easily be obtained by projecting the 68% ellipse (standard deviation) onto either axis [69].

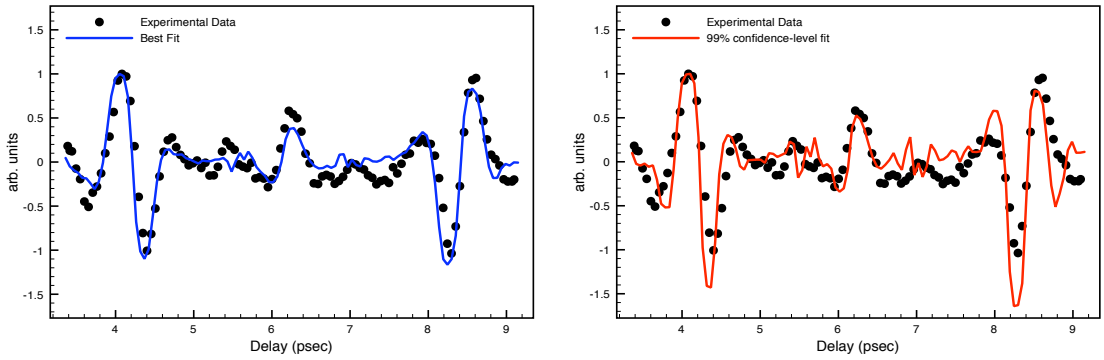

Figure 5.5: Illustration of the nitrogen χ^2 curve fitting. To calibrate the intensity of the aligning pulse, we fix the value of nitrogen's $\Delta\alpha = 4.67$ from accepted experimentally-obtained values in the literature. The left plot shows the best-fitting theoretical alignment curve (blue) for I=1.04×10^{14} W/cm^2 and the right plot is an example of a poorer fit (red) that falls near the 99% confidence-level ellipse (used I = 1.6×10^{14} W/cm^2, and T= 30 K).

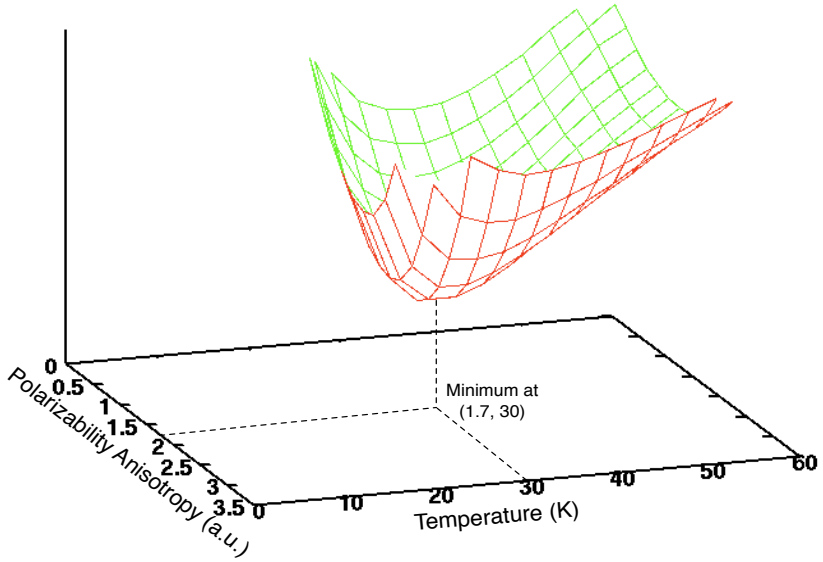

Figure 5.6: The fitting surface for the HBr $\Delta\alpha$ calibration. This χ^2 curve is based on an aligning pulse intensity of 1.05×10^{14}W/cm^2.

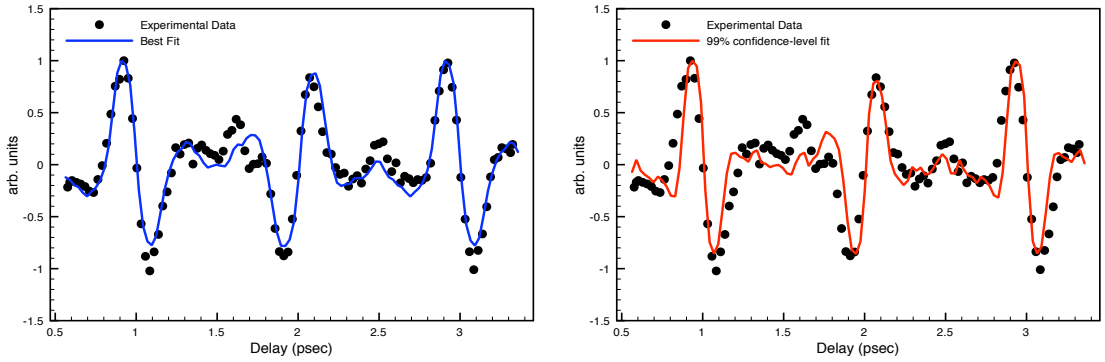

Figure 5.7: Illustration of χ^2 curve fitting for HBr using the optimal intensity found in section 5.3.1. Similar to Fig. 5.5, the optimal fit is plotted (blue) next to a fit with a parameter set from the 99% confidence-level ellipse extracted from Fig. 5.6.

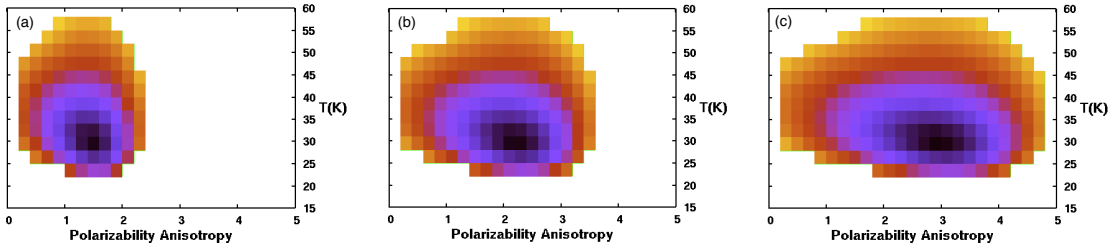

Figure 5.8: χ^2 fitting surfaces for the HBr alignment data set shown in Fig. 5.7. The minima are found for initial intensities input into the simulation at (a) 1.2×10^{14} W/cm^2, (b) 8×10^{13} W/cm^2, and (c) 6×10^{13} W/cm^2. The optimal simulated rotational temperature was consistently extracted to be 30K over a wide range of input intensities.

and the $\Delta\alpha$ value and rotational temperature are raster scanned over reasonable ranges. The fitting surface is shown in Fig. 5.6. Analogous to the nitrogen fitting routine, we illustrate the data-theory comparison of revival structures for HBr in Figure 5.7.

The fitting procedure for HBr is repeated for several intensities, in order to span the uncertainty in the extracted value from the nitrogen scans. Over this range, the temperature parameter was consistently minimized near 30K (see Fig. 5.8). Subsequent optimization is therefore limited to the pairing of the peak intensity and $\Delta\alpha$ parameters, which are

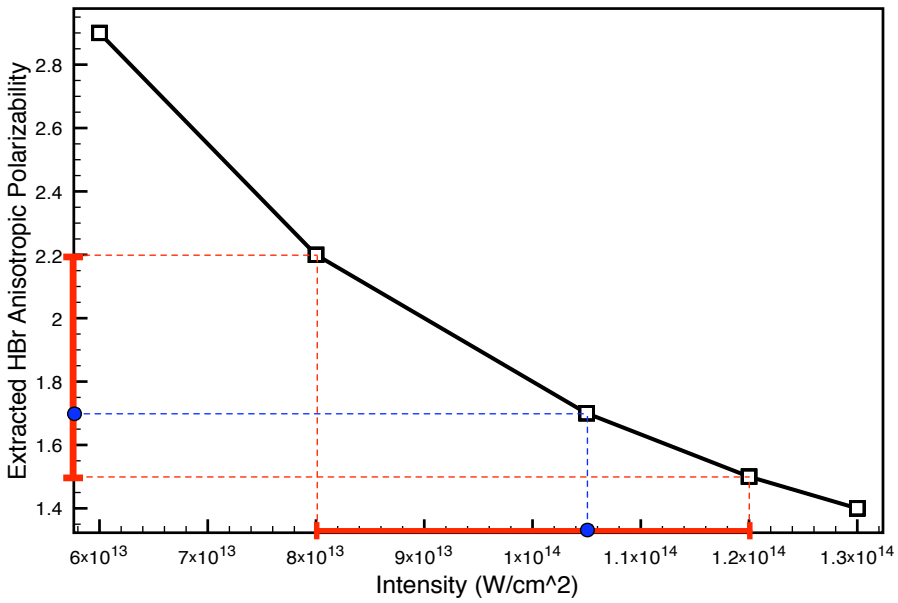

Figure 5.9: The extracted values of $\Delta\alpha_{HBr}$ for various intensities. The χ^2 fit for the HBr alignment data was minimized at $\sim$ 30K for all combinations of intensity and $\Delta\alpha$. Therefore, we obtain the error bars in $\Delta\alpha$ directly from the uncertainty in the intensity parameter.

related inversely in the laser-molecule interaction term. We extract an anisotropy value of $\Delta\alpha = 1.7$ a.u with error bars running from 1.5 to 2.2, resulting from the nitrogen intensity calibration (see Fig. 5.9). The error bars in $\Delta\alpha$ are obtained directly from the uncertainty in the estimated intensity. The precision of this measurement is comparable to that achieved by Sakai *et al.* for the anisotropy of the Van der Waals dimers. Our measurement agrees with previously calculated values for HBr (shown in Table 5.1), but is somewhat lower than the values previously obtained for DBr using other techniques.

We perform a quick consistency check illustrated in Fig. 5.10, by fitting the rigid rotor simulation to two alignment data sets, each taken at two different aligning pulse intensities (1.5×10^{14} and 1.1×10^{14} W/cm^2) and with a HBr source pressure of $\sim$ 115 psi. The

Table 5.1: Extracted $\Delta\alpha$ for HBr compared to previously obtained values

	$\Delta\alpha$ (a.u.)
Previous Theory [63]	2.25, 2.01
Prev. Experiments (DBr)[65]	3.89, 2.55
Current Experiment	1.7
Current Exp. Error	$\sigma_+ = 0.5, \sigma_- = 0.2$

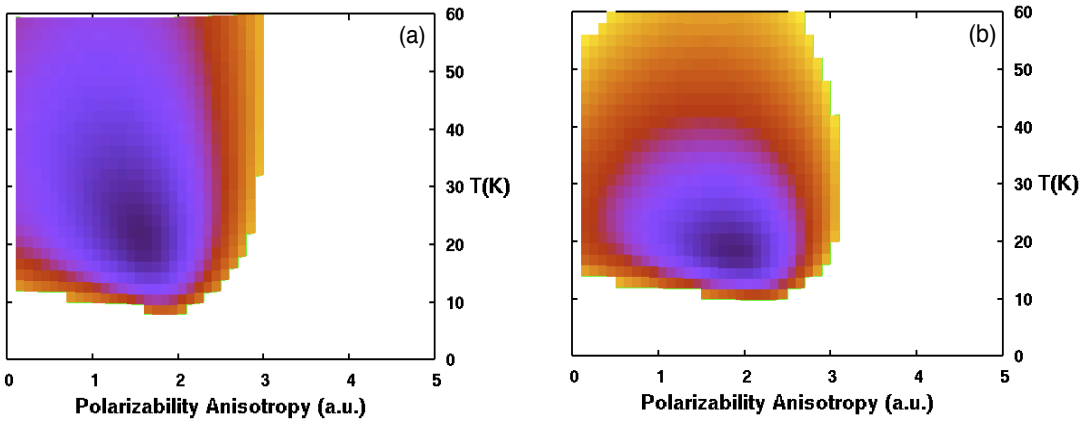

Figure 5.10: χ^2 fit consistency check with two experimental data sets taken at aligning pulse peak intensities of (a) I = 1.5×10^{14} W/cm^2 and (b) I = 1.1×10^{14} W/cm^2. The source pressure for the supersonic beam was $\sim$ 115 psi.

relative intensity was changed between the two scans by a combination of a zero-order half-waveplate and a thin-film polarizer. The actual intensity values were obtained by a relative comparison to the best intensity extracted in section 5.3.1. We find that the χ^2 routine found a consistent optimal temperature around 20K, and we extracted optimal values of $\Delta\alpha$ at 1.6 and 1.9 a.u., both of which fall well within the error bars noted above.

5.4 Conclusion

We have demonstrated a new technique for extracting anisotropic polarizabilities for diatomic molecules by inspecting their transient alignment dynamics. This method comple-

ments, but is distinct from, a technique based on adiabatic alignment used by Sakai *et al.* In particular, the necessary apparatus is considerably simpler, with pump and probe pulses derived from a single amplified laser. We perform our analysis purely on the time-domain transient alignment data taken from a single-stage time-of-flight spectrometer, without the need for a 2-D phosphor screen or delay-line anode. We utilize a χ^2 optimization routine which verifiably obtains the most probable values of the rotational temperature and intensity for an alignment scan. We extract a value for $\Delta\alpha_{HBr}$ which is in good agreement with existing predictions, and which we believe to be the first experimental measurement of the electronic $\Delta\alpha$ of hydrogen bromide. This technique is readily applicable to other diatomic molecules as well.

Chapter 6

Optimizing Dynamic Alignment

6.1 Introduction

The advent of laser-induced field-free molecular alignment has enabled measurements of molecular dynamics with unprecedented precision. The ability to produce spatially aligned gas-phase molecules has numerous applications in laser-pulse shaping, high-harmonic production, and chemical reaction dynamics [71]. This versatility begs for methods for improving the attainable degree of alignment in a molecular sample, particularly at room temperature.

The mechanism behind transient alignment is well understood [30] and has been detailed in Chapter 1. It has been established that the degree of alignment can be improved by increasing the alignment pulse energy, provided that the pulse duration remains much shorter than the fundamental rotational period of the molecule [5, 7, 30, 72]. Ultimately, however, ionization limits the maximum alignment pulse intensity. I show in Section 3.2.3 that laser pulse trains with pulse separations that are commensurate with the rotational revival period can be used to enhance the degree of alignment without increasing ioniza-

tion rates. Such pulse trains make it possible to increase the net angular impulse imparted to the molecule while keeping the peak intensity well below the ionization threshold. However, this technique is not necessarily the only option for improving alignment. At laser intensities sufficiently large to induce nonresonant multiphoton or tunneling ionization, dynamical variations in the molecular polarizability could have a significant effect on alignment. Thus, the shape of the temporal intensity profile of an aligning laser pulse(s) might be an important parameter for optimizing alignment. Unfortunately, a rigorous time-dependent treatment of the molecular dynamics in the presence of an intense laser field is prohibitively difficult. Thus, we cannot determine *a priori* for a given molecule what pulse shapes (if any) might perform more effectively than transform limited pulses. Instead, we explore the utility of laser pulse shaping [73–76] for improving alignment using a feedback-optimized closed-loop algorithm [77] to search for laser pulses which are more effective than transform limited laser pulse shapes for inducing transient alignment in room temperature CO. For convenience and to aid in interpretation, we limit our search to a class of shapes that are readily described by a two- or three-pulse time-domain parameterization [78] and use phase-only pulse shaping to preserve the pulse energy. We use principal control analysis to determine which pulse characteristics, in theory and experiment, are most important for the alignment control we observe. We find that, although the aligning laser intensities ($\sim 10^{14}$ W/cm^2) are large enough to produce ionization, a simple rigid-rotor model is still sufficient to describe the molecular dynamics.

6.2 Experimental Setup

This experiment is performed in Chamber #1 using the two available ultrafast laser systems detailed in Chapter 2. The 100 fsec laser pulses are used to align the CO molecules,

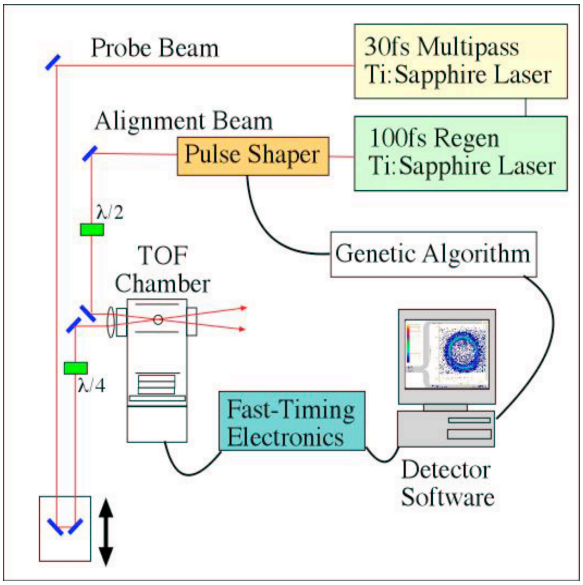

Figure 6.1: Experimental schematic for alignment optimization. The genetic algorithm uses experimental feedback from the detector to direct the pulse shaping of the 100 fsec laser pulses. Although the DLA is used to verify that optimal alignment is achieved with a single pump pulse, we employ the qualitative scheme in this experiment for more rapid feedback about the molecular dynamics.

and the pulses from the 30 fsec system probe the aligned molecules. The two lasers must be synchronized in order to minimize the electronic jitter between the pump and probe pulses. The alignment pulses then travel through a pulse shaper containing a spatial light modulator (SLM). A genetic algorithm (GA) receives feedback from the experiment, in order to direct a pulse-shape optimization run. Figure 6.1 illustrates the closed-loop optimization scheme for this experiment.

6.2.1 Laser Synchronization

Synchronization of the two laser systems is accomplished both optically and electronically. The 30 fsec mode-locked pulse train supplies the seed light to both amplifier cavities, maintaining a constant center wavelength. The 100 fsec cavity was not initially designed

to handle the 30 fsec spectrum, so the bandwidth is clipped in the grating expander to spatially match the spectral distribution of the 100 fsec pulses. We employ a DG535 Digital Delay/Pulse Generator as the master Q-Switch timing control for both lasers. This significantly reduces any relative drift between the firing of the two Nd:YLF pump laser pulses. The photodiode in the 30 fsec mode-locked cavity guarantees that the 1 kHz seed light is switched into the amplifier cavity at the appropriate point in the mode-locked pulse train.

6.2.2 Pulse Shaper

Direct temporal pulse-shaping is not a feasible mechanism to alter the E-field profile of an ultrashort pulse. There are, however, many available shaping techniques which involve the tuning of individual frequency components inside an optical frequency synthesizer [79]. The pulse shaper used in this experiment has a 128-pixel liquid-crystal spatial light modulator situated between a pair of reflection gratings and collimating optics, as shown in Fig. 6.2. Each pixel is able to provide a known ($-\pi \leftrightarrow \pi$) phase lag in addition to amplitude attenuation. Pixel voltages and target pulse-shape modeling are controlled by the GAShaper5 software (created by Dr. Charles Conover) through a GPIB connector.

The pixels of the SLM are calibrated to accommodate the bandwidth of the input pulse [80]. We plot the total transmitted energy through the shaper (measured as light scattered into a photodiode) as a function of a variable-width square-pulse gate function across the pixels. This reveals the integral of the laser spectrum as a function of the pixel number, from which the calibrated spectrum is extracted (Fig. 6.3). Our shaper has a wavelength resolution of ~ 0.15 nm per pixel.

The shaper can be instructed to perform phase-only shaping, by imparting a phase

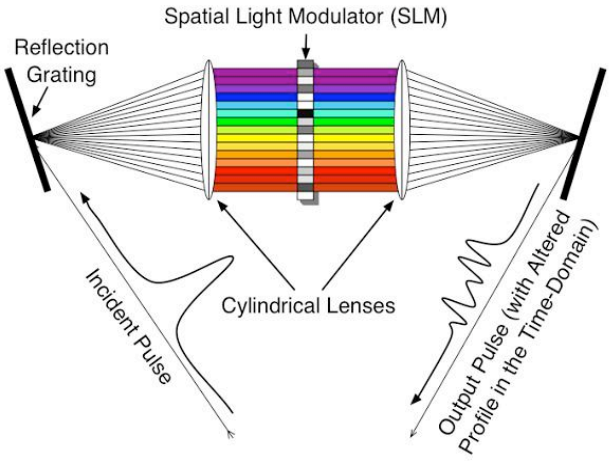

Figure 6.2: Schematic for liquid-crystal SLM pulse shaper. Applied pixel voltages control the amplitude and phase of up to 128 different spectral regions. The frequency-domain shaping is translated into the temporal domain via reflection gratings.

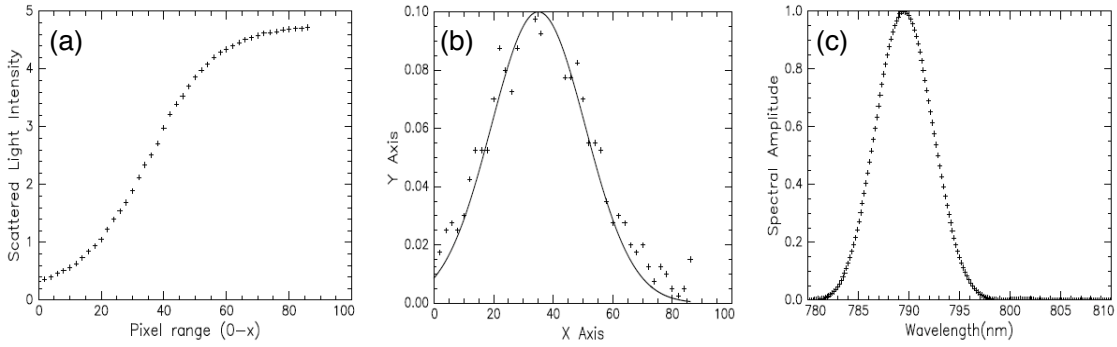

Figure 6.3: Calibration of the SLM pixels. (a) The integral of the frequency spectrum, mapped out by the gate window function. (b) The derivative of the data from (a), overlapped with a least-squares Gaussian fit for the spectrum. (c) The corresponding spectrum calculated for a transform-limited 100 fsec laser pulse.

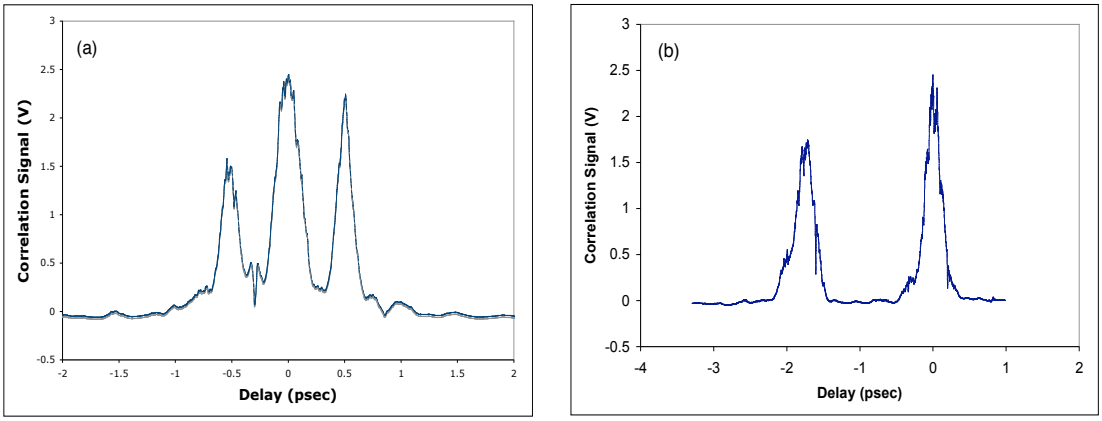

Figure 6.4: Sample cross correlations of shaped 100 fsec laser pulses with transform-limited 30 fsec pulse. The software was instructed to generate (a) 3 identical transform-limited pulses at $\tau = -500$ fsec, $\tau = 0$ fsec, $\tau = +500$ fsec, and (b) 2 identical transform-limited pulses at $\tau = -2$ psec & $\tau = 0$ psec. The pulse delay in (b) is the maximum achievable with the spatial resolution of the current 128-pixel pulse shaper.

shift function [81]

$$E_{out}(\omega) = E_{in}(\omega)e^{i\Delta(\omega)} \tag{6.1}$$

upon the incident light. As the total energy of the pulse is proportional to $\int_{-\infty}^{\infty} |E(\omega)|^2 d\omega$, this phase shifting process leaves the output pulse energy unchanged.

With the GAShaper5 program, the pulse can be divided into a train of up to 5 pulses by selective modulation of the spectral phases. The maximum temporal spread between the earliest and latest pulses is limited by the resolution of the SLM pixels, and it can therefore only generate pulses falling within a ± 2 psec time window. We verify in Fig. 6.4 that the actual output pulses exhibit the temporal characteristics programmed into the shaper. These are cross correlations of shaped pulses from the 100 fsec amplifier with transform-limited 30 fsec pulses from the other laser system. Although a δ-function is the ideal shape to cross-correlate with the phase-shaped pulse trains, the 30 fsec laser

pulse is short enough to adequately probe its shape. Additionally, after the laser beam travels through the interaction region of the spectrometer, it propagates directly into the PG FROG apparatus, so that images of the shaped pulses can be viewed in real-time. The beam's temporal profile at the FROG is not significantly affected by GVD from the chamber windows or by interactions with the ultrahigh vacuum target gas molecules.

The shaper is placed into the beam before the final pulse compression stage, to prevent damage to the liquid-crystals. By the time the shaped pulse is compressed, it can have energies up to 800μJ (40% of the light is lost on the compressor gratings). When focused, these aligning pulses have peak intensities as high as 2×10^{14}W/cm^2, which causes significant CO^+ ionization yield, but no dissociative ionization. The 300 K rotational temperature of the molecules necessitates a high aligning pulse intensity, as the angular impulse imparted by the laser must overcome the initial thermal rotational angular momentum of each molecule in the ensemble [82].

6.2.3 Genetic Algorithm

There are far too many parameters present with the full 128-pixel SLM array for most traditional search algorithms to converge in a useful amount of time (a few hours, in our case). We select a GA to perform this task, due to its relative robustness and ease-of-use. Genetic algorithms are based on ideas developed in evolutionary biology, where different solution methods are treated as competing individuals in an evolving population. Solutions with better outcomes are given a higher chance of surviving to a new generation of individuals. The algorithm (illustrated in Fig. 6.5) generates a new population from an old one by a set of standard evolutionary operators, such as tournament selection, single-point crossover, bitwise mutation, and cross-generational elitism [83]. We apply a two-pulse time-domain parameterization scheme to describe the profiles of the target

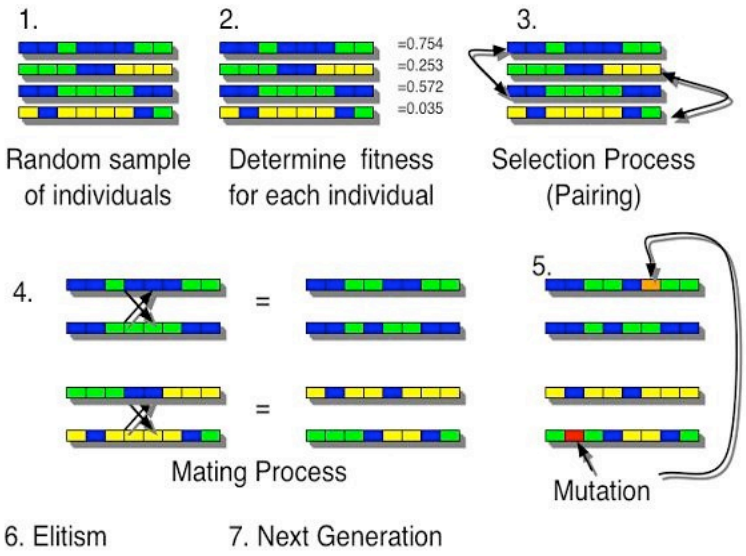

Figure 6.5: Schematic operation of a typical GA. A random population of individuals is generated with certain observable characteristics (phenotypes). Each of these individuals is given a fitness value corresponding to how effective they are at accomplishing a task (i.e. aligning molecules). Robustness arises from the fact that this algorithm applies to a broad range of multi-parameter search problems, and the only feature of the algorithm that needs to be altered is the decoding of the chromosome bit string into a phenotype for fitness evaluation (step 2 above).

pulse shapes with four parameters: (i) pulse-1 width, (ii) pulse-2 relative amplitude, (iii) pulse-2 relative delay, and (iv) pulse-2 width. For three-pulse shaping, three additional parameters analogous to (ii)-(iv) above are needed. As mentioned earlier, we restrict the laser energy to fall within a 4-psec window, due to the limitations of the frequency resolution of the SLM pixels. We also intentionally preclude the algorithm from finding known [55] impulsive solutions in which the molecule is periodically kicked at the revival time. The probe pulse delay is set at the first full alignment revival time (T=8.78 psec) for an unshaped alignment pulse. We fix the delay of a primary alignment pulse at T=0, while the second (and third) pulse delay varies from ± 2 psec. The target pulse's profile is then mapped onto the frequency domain to determine the required retardance for each pixel of the SLM. The control loop generates new pulse shapes by encoding the parameters as a binary string (i.e., an individual) and by allocating a user-defined fitness value generated from experimental feedback.

Thermal expansion of the table supporting the two laser systems alters the pump-probe laser delay, putting an acceptable upper limit of 2 h on the duration of any given GA run. In order to process a large number of pulse shapes within this time limit, we apply the qualitative TOF technique described in section 3.2.2. Due to the inherent time associated with the establishment of the correct retardance through each SLM pixel, 2 sec is an effective lower limit on the fitness evaluation time for a given individual.

At room temperature, only weak alignment is observed with the qualitative detection scheme. Therefore the difference in the fragment ratios R (i.e. the ratio between fragments ejected parallel vs. perpendicular to the spectrometer) for aligned versus unaligned samples is quite small. As a result, we use a nonlinear fitness function e^R, which amplifies the variations in R that are observed for different pulse shapes in each generation. This also tends to amplify the the noise with the signal, but it does not preclude the overall

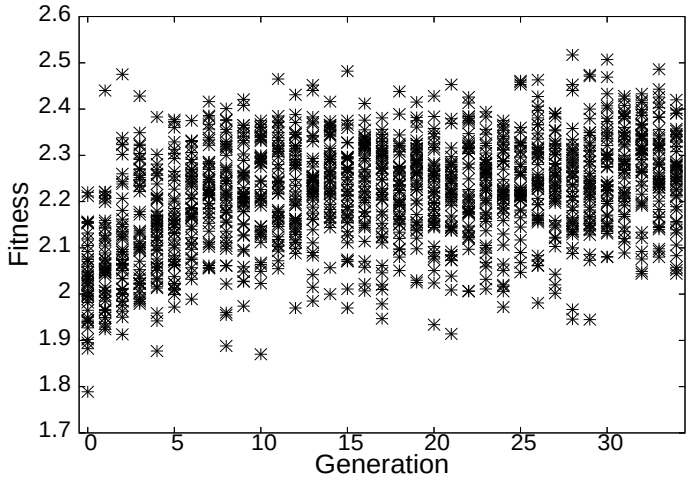

Figure 6.6: Individual fitness vs. generation for a typical experimental 2-pulse alignment optimization run. Here, fitness = e^R, where R is the ratio of fragments ejected parallel to the spectrometer axis to those ejected perpendicularly. Fitness plots such as these normally don't attain perfect convergence to a singular value, because every new generation has a finite mutation rate per individual, in addition to the experimental noise. Towards the latter generations, however, the population's FROG traces tend to converge to a smaller class of shapes (i.e. the transform-limit).

convergence of the algorithm.

6.3 Results

Figure 6.6 shows a plot of individual fitness versus generation for a typical two-pulse parameterization run. After about 30 generations, the average fitness per generation plateaus, and we observe that the algorithm searches a much narrower range of parameter space. This is evident in the frequent appearance of similar pulse shapes on the FROG in subsequent generations. The algorithm frequently converges on non-transform-limited pulse shapes. Following a GA run, the fittest individuals are reloaded onto the SLM and

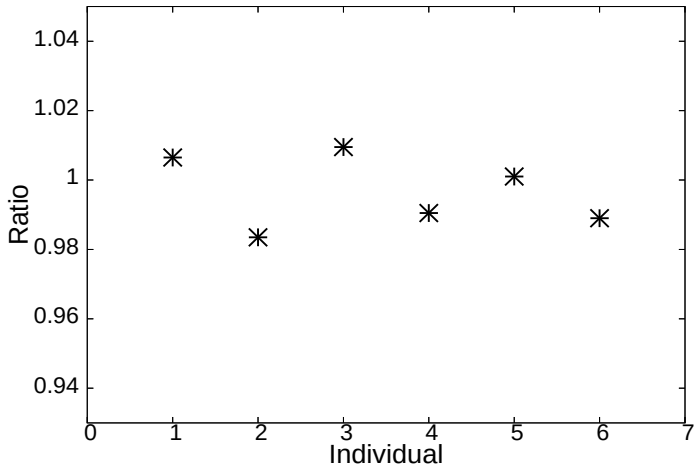

Figure 6.7: Ratio of fitnesses for selected shaped pulses to (near-)transform-limited pulses. Pulse fitnesses here are reevaluated separately from the GA. This illustrates the robustness of the algorithm in the face of laser noise.

their fitnesses are reevaluated in direct comparison with an unshaped, near-transform-limited pulse. We find that a number of complex pulses align the CO molecules just as well as the transform-limited pulses (see Fig. 6.7), verifying that the algorithm's convergence is not influenced significantly by experimental fluctuations. The FROG traces of a few of these high-performance pulses are shown in Fig. 6.8. Visual inspection is sufficient to tell that the pulse energy is spread out along the delay axis for a number of the converged pulse shapes. Further illustration of the GA's convergence is shown in Fig. 6.9. In this plot, the algorithm directed the SLM in a 3-pulse optimization scan (with 7 shaping parameters), and the pulses plotted are simulated based on the chosen pulse parameters.

We do not find laser pulse shapes that performed significantly better than transform-limited pulses for aligning room temperature CO. This is consistent with the results of other investigations of transient alignment using shaped laser pulses [74]. Nevertheless, it

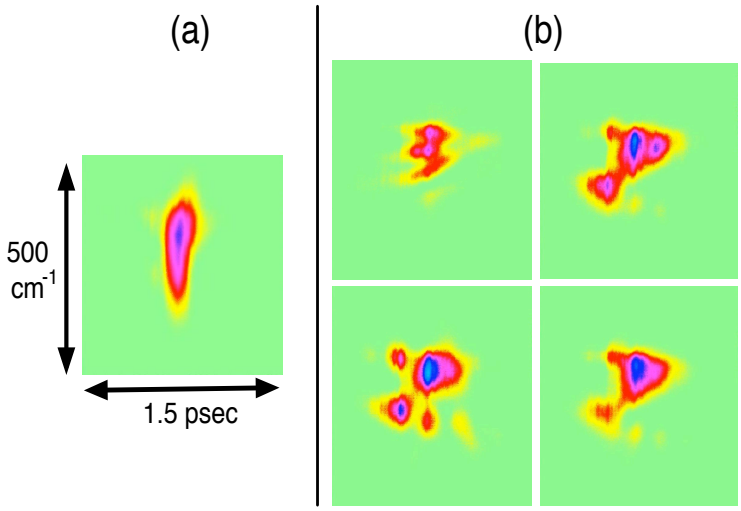

Figure 6.8: PG FROG traces of high-performance pulse shapes taken from the experimental GA search, using the two-pulse parameterization scheme. (a) A near-transform-limited pulse. (b) Non-transform-limited, nonimpulsive shapes which align CO as effectively as a transform-limited pulse. Color scale: green is lowest intensity and light blue is highest intensity

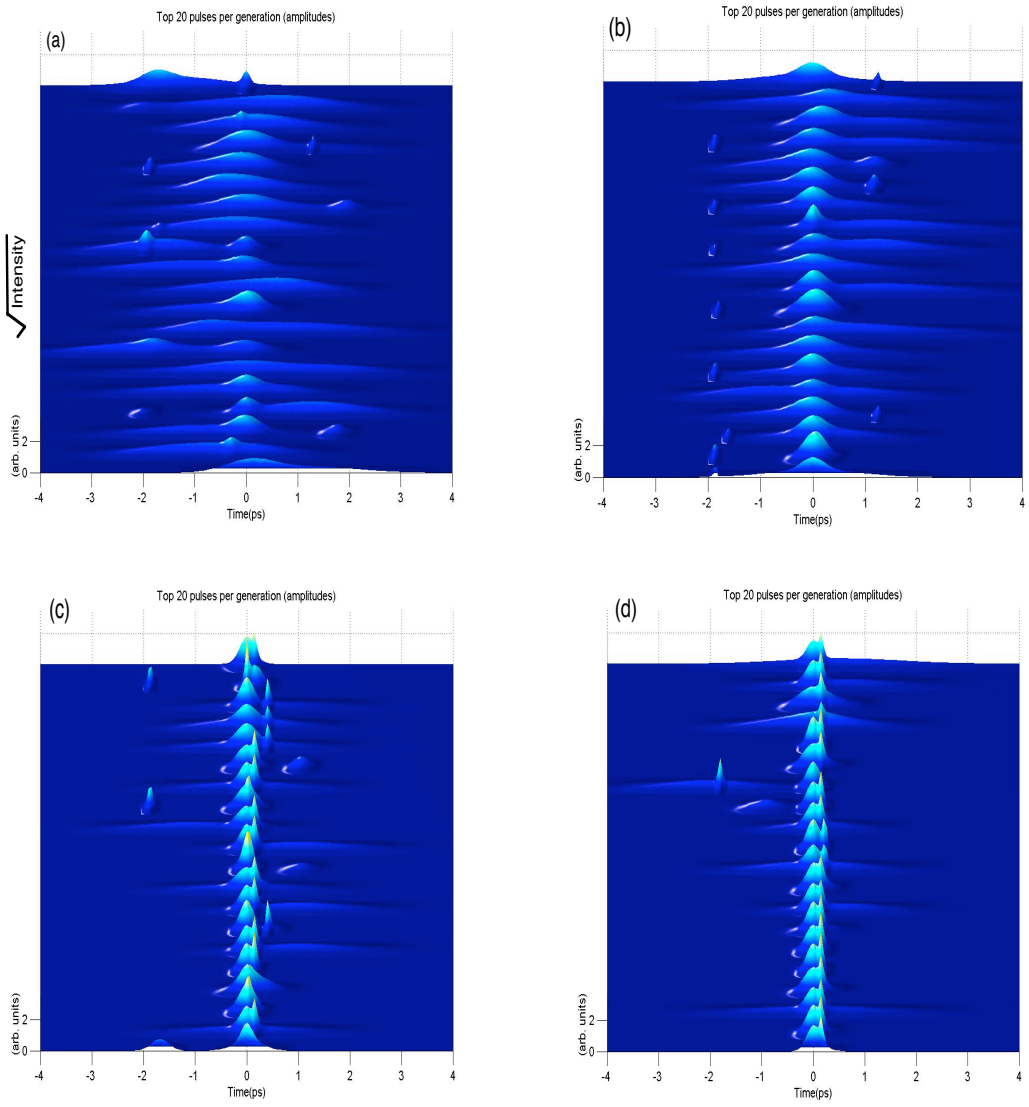

Figure 6.9: The phenotype optimization during a 3-pulse GA run for (a) generation 1, (b) generation 16, (c) generation 33, and (d) generation 41. The plots display the 20 best theoretical pulse shapes ($\sqrt{I(t)}$) for each generation. Although there is significant noise in the experimental fitness plot in Fig. 6.6, this arises from the experimental noise during the fitness evaluation.

is still interesting to consider why some pulse shapes perform at least as well as transform-limited, but others do not. For instance, Sakai *et al.* recently noted that single pulses with a "trough" in the middle had optimal fitnesses in their GA runs [76].

6.4 Discussion

Using a rigid rotor model, we can numerically compare the degree of alignment produced with near-transform-limited pulses to that achieved with pulse shapes corresponding to the best performing individuals found in the experiments. In most cases we find, as in the experiments, that the optimized pulse shapes performed approximately as well as transform-limited pulses - some slightly better, others not quite as well. In some cases, pulse shapes which appeared to work well in experiments result in significantly lower levels of alignment as compared to transform-limited pulses. This apparent inconsistency might be the result of small difference between the theoretical pulse shapes and those actually used in the experiments, small drifts in the relative delay between the alignment and probe pulses, or more interestingly, a break down of the rigid-rotor model which assumes constant polarizabilities even at intensities large enough to cause substantial ionization. We also note that while the time at which the maximum alignment revival occurs does vary slightly depending on the aligning pulse shape, it is typically within 30 fsec of the experimental revival time (8.78 psec). This temporal variation is comparable to the duration of the Coulomb explosion pulse and, therefore, would be difficult to observe experimentally. Moreover, the computed variation in $\langle \cos^2 \theta \rangle$ within a 30-fsec window is well below the experimental noise.

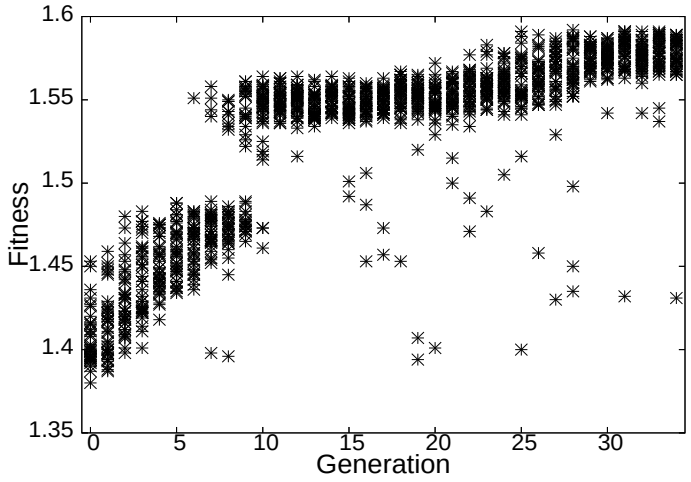

Figure 6.10: Individual fitness vs. generation number for a typical simulated two-pulse alignment optimization run. In order to model the experimental data more closely, fitness=$e^{\langle\cos^2\theta\rangle}$, where $\langle\cos^2\theta\rangle$ is determined from the calculated angular distribution for the molecular ensemble.

6.4.1 Theoretical Optimization

To better test the rigid-rotor model we performed numerical optimization runs with the two-pulse rigid-rotor simulation providing the feedback as to the fitness of individual pulse shapes. Noise ($\sim 5\%$) was added to the computed values of $\langle\cos^2\theta\rangle$ in accordance with the noise levels observed in the experiment. Figure 6.10 shows typical GA fitness convergence for a two-pulse simulation, analogous to the experimental results in Fig. 6.6. As in the experiment, the GA identifies more complex pulse shapes that perform as well as a transform-limited pulse, but none that surpass it. We also ran the GA simulation with the observation time as an additional variable parameter. As with the direct simulations for specific pulse shapes described previously, the optimal pulse shapes found by the GA produced alignment maxima within 20 fsec of the experimental revival time.

6.4.2 Principal Control Analysis

In both experiment and simulation, the characteristics of the "ideal" pulses and GA convergence trends are not evident by inspection. Therefore, we use principal control analysis (PCA) to understand the relative importance of these parameters [78, 84, 85]. In particular, we focus primarily on the two-pulse results. In this case, the pulse shapes in both experiment and calculation are characterized by only four parameters. PCA utilizes data from the entire set of pulse shapes used in a GA run, not just the fittest individuals, and this data is compiled into an $m \times n$ matrix $\mathbf{X}$, where m is the number of shaping parameters, and n is the total number of individuals (i.e. pulse shapes) employed in a single GA run. PCA utilizes the correlation (or covariance [86]) matrix, given by

$$C_{i,j} = \frac{\langle \delta_i \delta_j \rangle - \langle \delta_i \rangle \langle \delta_j \rangle}{\sigma_{\delta_i} \sigma_{\delta_j}}. \tag{6.2}$$

This is an $m \times m$ symmetric matrix which describes all the possible correlations between the various shaping parameters. We seek to transform this matrix such that it maps the correlations between a new set of prinicpal control parameters. This parameter set should ideally have strong variances and relatively weak covariances, which is analogous to diagonalizing $\mathrm{C}_{i,j}$. From linear algebra, a matrix comprised of the eignvectors of $\mathrm{C}_{i,j}$ is used to diagonalize it, and the eigenvectors themselves are called the principal control directions. Physically, we seek to find the best set of orthogonal "knobs" or pulse characteristics that are effective for maximizing alignment.

The fitness values are correlated both with the original basis vectors(δ_i) and with the projection of the pulse shapes onto the eigenvectors(η_i),

$$B_\delta = \frac{\langle \delta_i f \rangle - \langle \delta_i \rangle \langle f \rangle}{\sigma_{\delta_i} \sigma_f}, B_\eta = \frac{\langle \eta_i f \rangle - \langle \eta_i \rangle \langle f \rangle}{\sigma_{\eta_i} \sigma_f}. \tag{6.3}$$

We compared the PCA results for the experimental and simulated GA searches, as seen in Fig. 6.11, and note a striking similarity between the two. In both cases, the eigenvectors with the largest eigenvalue have the strongest correlation with the fitness values, as suggested by White et al [85]. It is apparent in this particular eigenvector that in both data sets, the parameters for the widths and the relative amplitudes of the shaped pulse pair have comparable weights, whereas the second pulse's relative delay is relatively insignificant. The signs of the strongly weighted elements within the primary principal control direction are also correlated, suggesting a likely pathway by which the pulse shape is optimized. When the algorithm is run, the evolution of the best pulses per generation approaches the transform-limited case, corresponding to a shrinking of the pulse widths and, in many cases, a reduction of the pulse-2 relative amplitude. In experiment and simulation, this quality emerges repeatedly over a series of GA scans with varying search parameters, indicating that the algorithm tends to search the parameter space similarly each time it is executed. In the case of 3-pulse shaping, similar features were observed, and these are shown in Figure 6.12. Again the eigenvector with the largest eigenvalue has the strongest correlation with the fitness, and its shape has similar features to the 2-pulse principal control vector. The similarity in the composition of the eigenvectors associated with the principal control directions for experiment and simulation provides strong support for the notion that the laser-molecule interaction responsible for alignment has been accurately simulated.

6.5 Conclusion

In summary we have explored the use of a closed-loop control scheme for optimizing transient laser alignment of room temperature CO. Specifically, we consider pulse shapes

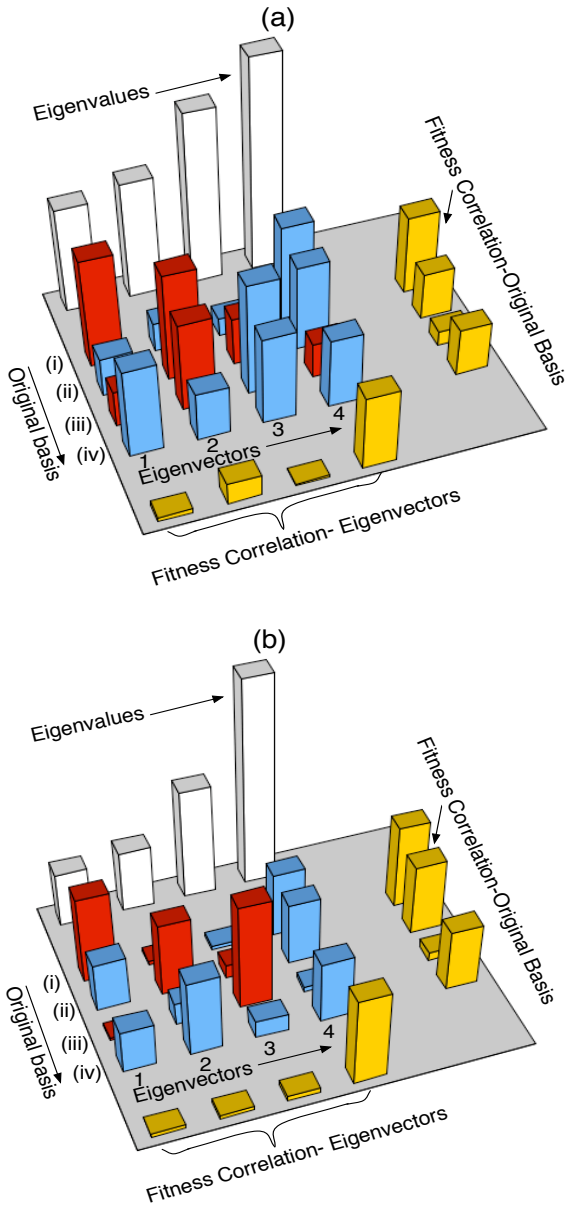

Figure 6.11: Principal control analysis results for (a) experimental data and (b) simulation. The four middle columns are the eigenvectors of the correlation matrix for all the pulse shapes within a GA scan, and they are ordered according to their corresponding eigenvalues. The eigenvectors are expressed as linear combinations of the original parameters: (i) pulse-1 width, (ii) pulse-2 relative amplitude, (iii) pulse-2 relative delay, and (iv) pulse-2 width. The signs of the eigenvector elements are indicated by light blue (+) and red (-). Fitness correlations for the eigengbasis and original basis vectors are also shown.

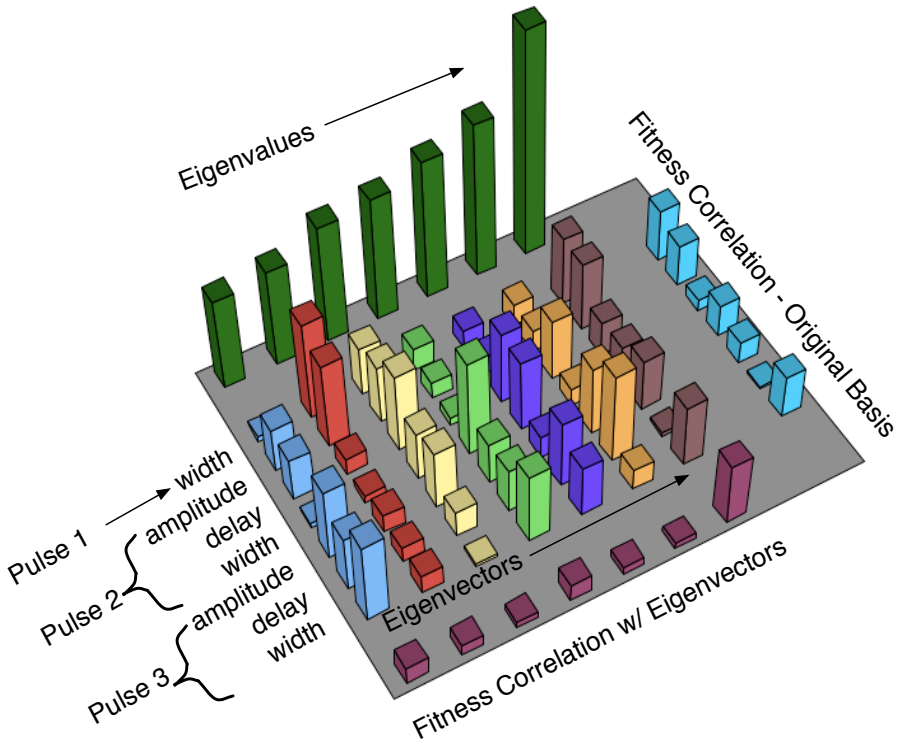

Figure 6.12: Principal control analysis results for a typical 3-pulse-shaping experimental GA scan. The color-coding is chosen differently from Figure 6.11 to illuminate the 7 eigenvectors of the correlation matrix. The correlation of the fitness with the original shaping parameters exhibits the same characteristics as the corresponding values for the 2-pulse case.

consisting of two- or three-component pulses with variable widths, relative amplitudes, and relative delays. Excluding pulse trains which periodically kick the molecules at integer or fractional revival times, we find no pulse shapes that perform substantially better than transform-limited pulses. Apparently the broad, incoherent initial rotational-state distribution that is present in the room temperature ensemble reduces any sensitivity of the maximum achievable alignment or alignment revival time to the details of the aligning pulse shape. From a practical perspective, however, we do find pulse shapes with durations that are a substantial fraction of the fundamental rotational period of the molecule, yet still produce alignment factors equivalent to that observed with shorter, near-transform-limited pulses with the same energy. Because the peak intensities of the shaped pulses are substantially lower, they can be used at higher pulse energies, providing larger degrees of alignment with reduced ionization levels. Also, principal control analysis of performance versus pulse shape parameters for entire optimization runs identifies the combination of characteristics that are most essential for alignment control. The fact that very similar principal control directions are found for experimental and simulated searches strongly suggests that, somewhat surprisingly, the essential features of the experiment are captured by a simple rigid-rotor model that assumes constant polarizabilities. Given the large parameter space surveyed in the optimization runs, PCA provides more evidence for the validity of the model than a simple comparison of the measured and predicted performance of individual pulses. Analogous comparisons of experimental and simulated closed-loop optimizations results from experiment and simulations might provide a powerful tool for evaluating the accuracy of approximate quantum dynamical models in other systems as well.

Chapter 7

Asymmetric Molecular Dissociation

7.1 Motivation

We delve further into the structure of diatomics by exploring methods to differentiate one end of the molecule from the other. The two atoms comprising a heteronuclear diatomic molecule have different electronic structures, and the electrons are unevenly shared between the two nuclei. The permanent dipole arises from this, and by tailoring a laser field to distinguish between the "head" and "tail" of such a molecule, we can exploit its inherent asymmetry. For example, researchers have recently shown [87, 88] that using ultrashort pulses with carrier-envelope phase stabilization, and with durations of only a few optical cycles, asymmetric fields can be generated. When applied to the D_2 molecule, this field was shown to selectively control the electron localization between the two nuclei as they dissociated.

Such a field is also readily produced by combining a fundamental laser field at ω and

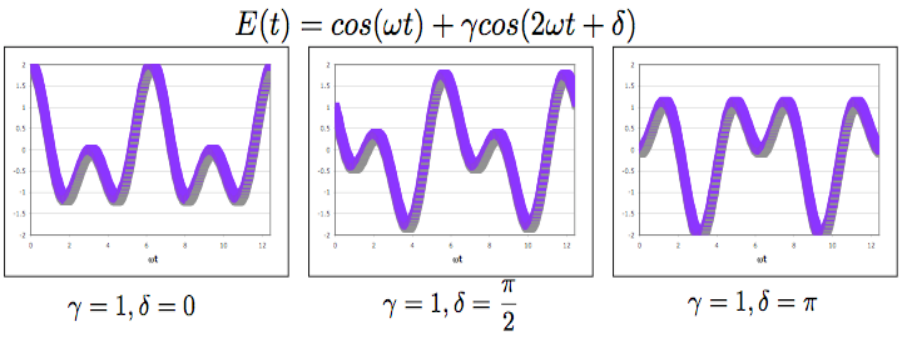

Figure 7.1: Field asymmetry that arises from the combination of two phase-shifted cosines at ω and 2ω.

its second harmonic 2ω. The resultant laser field has a peak E-field in one direction which is greater than the opposite direction (see Fig. 7.1). Usage of such a laser field was seen as early as 1990 when applied to the above-threshold ionization spectrum of krypton [89]. DiMauro *et al.* have also utilized this field combination to modulate the fragment directionality in the dissociated products, ($H + D^+$) or ($H^+ + D$) of HD^+, using such a tailored E-field [90]. More recently, Ohmura *et al.* incorporated such pulses to measure the selective ionization of non polar molecules [91]. T. Zuo *et al.* [92] proposed that, in order to produce even high-harmonics (which can only occur if the wavefunction symmetry is broken), only a relatively weak asymmetry is required, and the 2ω field can be much smaller than the ionizing field. Clearly, strong asymmetric fields have the potential to break the forward-backward symmetry of the molecular wavefunction.

In general, asymmetric fields can guide directional dynamics in any system. However, from a molecular control perspective, it is more interesting to have independent control over both the handedness (i.e., orientation) of the molecule and the field. While polar molecules can be oriented in strong static electric fields, the presence of these large fields can make some experiments difficult or impossible (e.g., electron spectroscopy). Moreover,

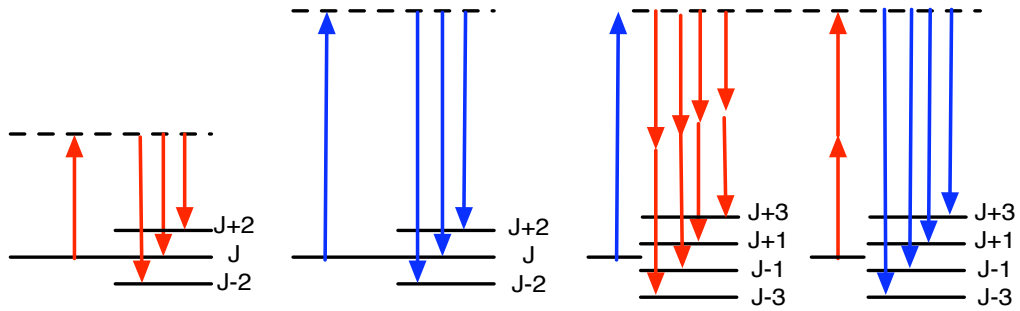

Figure 7.2: Quantum picture of the formation of a wavepacket without definite parity. The presence of the $\omega + 2\omega$ field allows both even and odd rotational transitions.

non-polar molecules cannot be oriented in this way. To this end, a number of groups are considering the use of asymmetric laser pulses to transiently orient molecules in analogy to the transient alignment previously described.

Single-color Raman scattering enables the redistribution of population from an initial rotational level J, to other rotational levels J' in the same electronic manifold. However, due to optical selection rules, J-J' = Δ J, must be even. The Raman process therefore conserves the parity of the rotational wavefunction [56], which is defined as $(-1)^J$. When two colors at ω and 2ω are mixed, however, scattering can also produce ΔJ = odd, as shown in Fig. 7.2. The presence of both types of interactions leads to a rotational wavefunction without definite parity, in principle allowing the molecule to be oriented in a head-over-tail manner [93]. Further references in this chapter to the term "orientation" describe the creation of this asymmetric molecular wavefunction. "Alignment" still refers to the symmetric narrowing of the wavefunction about the laser polarization axis. Field-free orientation has also been theoretically predicted by an application of a terahertz-regime half-cycle pulse [94] to directly torque a molecule with a permanent dipole moment. However, no experimental field-free orientation has been detected with that method, due

to the inherent difficulties with the production of high-intensity, purely half-cycle pulses.

We employ a two-color phase-sensitive pump pulse in combination with a linearly polarized probe pulse to explore the dissociation dynamics of diatomic molecules and to search for evidence for the creation of rotational wavepackets without definite parity. The experiments are performed both at room temperature and at $\sim$ 30 K. Fragmentation events are recorded solely with the MCP signal from the TOF spectrometers in both labs, and we show the results for 3 molecules. We detect a clear asymmetry in the fragment directionality, which only occurs during pump-probe overlap and appears to be independent of the laser pulse duration and the probe intensity. We determine that, rather than a laser induced orientation, this process is a product of enhanced ionization in the asymmetric field at a critical internuclear distance, R_C [20, 24].

7.2 Experimental Setup

In this experiment we explore the results of exposing diatomic molecules to an asymmetric E-field (this is performed with varying conditions in both chambers). To produce the field asymmetry, we need to temporally and spatially overlap the ω and 2ω beams and keep their relative phase stable to within $\lambda_{2\omega}/4$. We assemble a Mach-Zehnder interferometer with a 250 μm BBO doubling crystal in one of the arms, as shown in Fig. 7.3. The beam paths are recombined with a dichroic reflector for the 390 nm light, which also separates the probe beam. This setup produces the two-color collinearly overlapped pump beams, and a more intense Coulomb exploding probe beam. The field asymmetry is maximized when the quantity γ from Fig. 7.1 is approximately $\frac{1}{2}$. This is easily accomplished by either detuning the doubling crystal angle or by aperturing the red pump beam, as necessary.

A pair of thick quartz windows in a chevron pattern enables us to obtain coarse tem-

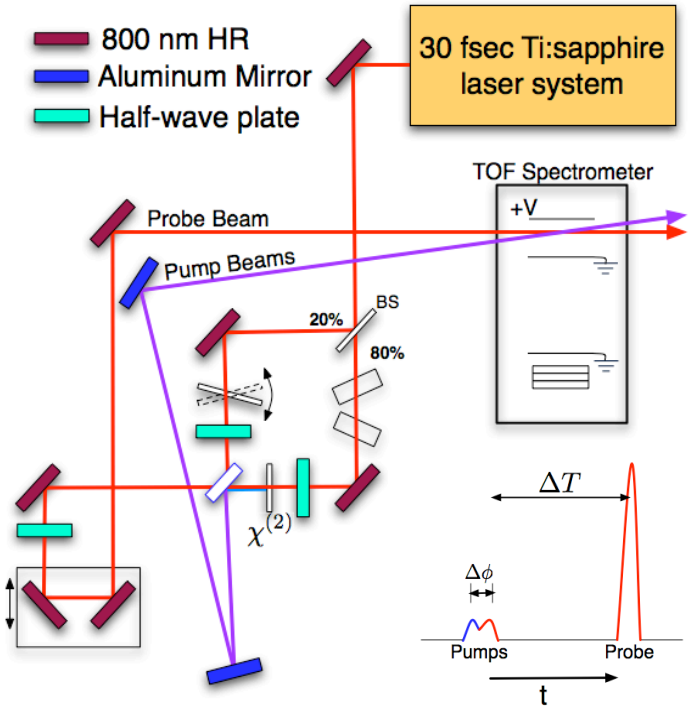

Figure 7.3: Experimental setup for the generation of an asymmetric field pulse. Two thick quartz windows are situated in one arm of the interferometer to enable coarse delay tuning with no transverse beam shift. A thin coverslip is dithered between two angles θ_1 and θ_2, to effect a change in the relative delay between the pumps.

poral overlap between the two pumps, and the alternating arrangement ensures no net transverse shift (see Appendix B). A small portion of the probe beam (at ω) is partially reflected by the recombining mirror. Tuning the quartz window pair by an appropriate delay, we can overlap the scattered probe beam with the red pump beam collinearly. The interference fringes are adjusted to be planar, to ensure that the $\omega + 2\omega$ interference proceeds similarly. An extra glass window is added to the red-pump beam path to ensure that both the pump and the probe receive an equivalent amount of positive-GVD from all the optics; the compressor gratings are then adjusted to compensate for the glass and to produce near-transform-limited pulses in the chamber interaction region. Pulse durations of ~ 40 fsec were measured with a FROG apparatus, and also with pulse overlap ionization signals in the chamber.

A glass 0.15 mm-thick coverslip inserted in one of the interferometer arms fine-tunes the relative phase between the two pump beams. The coverslip is set to a shallow angle to minimize the transverse shift of the relative foci (Appendix B), but with enough of an angle to provide up to 3 full red-wavelengths of temporal delay (~ 8 fsec). The data collection software dithers this angle periodically by coupling to the rotating motion of a stepper motor. The collinear pumps are focused with a f=35 cm, air-spaced achromatic lens, to ensure that their two focal volumes overlap sufficiently along the longitudinal direction. The intensities of the two beams are set to be approximately 1×10^{14} W/cm^2.

The asymmetry in the field-molecule interaction is detected with a similar scheme to the qualitative TOF alignment detection method described in Chapter 3. The target molecules are N_2, CO, and HBr with zero, small, and large dipole moments, respectively. The two pump beams are linearly polarized parallel to the spectrometer axis, and the probe pulse is non-collinearly overlapped with them. The non-collinear crossing ensures that the phase difference between the pump and probe beams varies continuously through

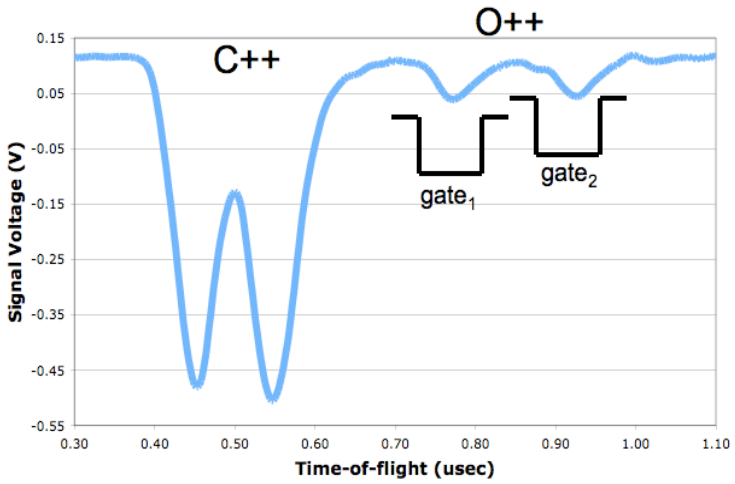

Figure 7.4: Using the TOF to detect the asymmetry in the fragment directionality. Gates are placed over forward and backward ion pairs, and the weighted difference, β, is plotted as a function of the relative phase between the ω and 2ω beams.

the sample. Thus, any observed phase variation in the signal is due to the phase difference between the two pump beams. The pump intensities are sufficient to singly ionize the molecules, and in some cases, generate singly-charged fragments, but they do not produce detectable quantities of the high-charge-state fragments in which we detect the asymmetry. On a related note, both the 800 nm and 400 nm pumps independently create rotational wavepackets and produce transient alignment in CO.

We look at the doubly-charged (or higher) fragments which are ejected towards and away from the detector. These fragments are detected in current mode with a probe pulse, which is polarized linearly and is parallel to the spectrometer axis. Using either the Data Collect program or the SRS Gated Integrators, we place gates over both the forward and backward peaks (shown in Fig 7.4 for CO fragments), and we map the fragment directionality with an asymmetry parameter, β, identical in form to the one used in section 5.2.

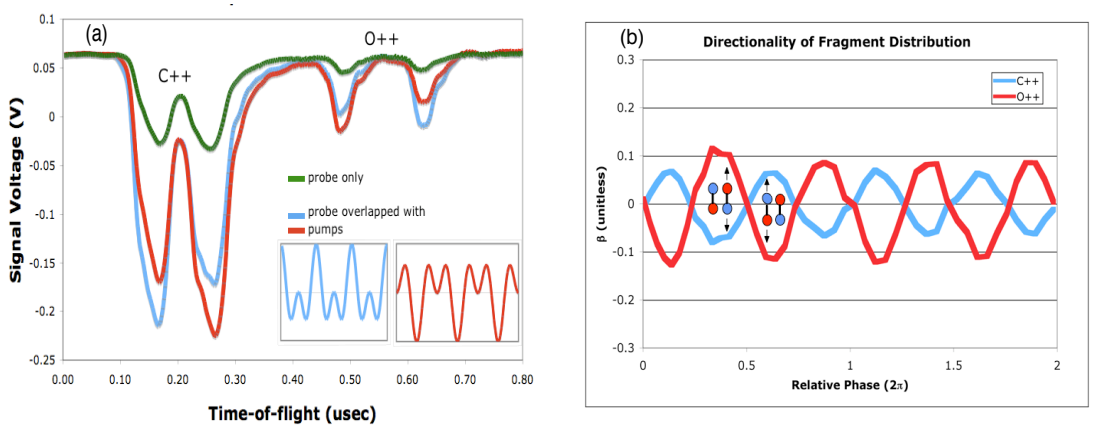

Figure 7.5: (a)Time-of-flight spectra from the Chemistry lab setup for the 3-beam overlap in which a dissociation asymmetry is detected. Note that the $\omega + 2\omega$ pumps do not produce doubly-charged fragments except when overlapped with the probe. The inset figures illustrate the field directionality which result from the pump beam being dithered at two phases. (b) Plot of the asymmetry seen in both the C^{2+} and O^{2+} fragments. The oscillation is shown as the β - parameter between a pair of gates, and there is a 180° phase shift between the two oscillations.

7.3 Results

For the first molecular species (CO), we find a clear asymmetry as the relative pump delay is dithered over several wavelengths. In Fig. 7.5, all three beams are temporally and spatially overlapped in the Chemistry lab spectrometer. There is a significant enhancement of the total probe fragmentation signal when the pumps are present. The signal oscillations shown in Fig. 7.5b arise as the adjustable coverslip sweeps through several red wavelengths of delay (note that "oscillations" and "asymmetry" are used interchangeably throughout the chapter). The probe has an intensity which is approximately an order of magnitude greater than that of the pumps combined. With approximately equal pump intensities, we estimate that (at the maximum field asymmetry) the pump+probe field parallel to the internuclear axis is 2% greater than the field antiparallel to it.

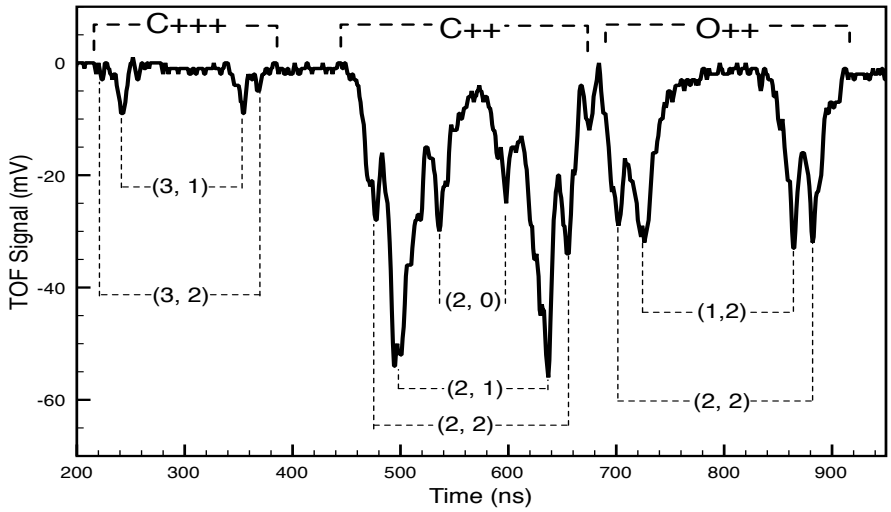

Figure 7.6: The CO time-of-flight spectrum taken from the Physics lab spectrometer, with several dissociation channels labeled. We found the asymmetry oscillations in the (2,0) channel were significantly suppressed relative to the other channels.

Using the physics lab spectrometer, we are able to resolve TOF peaks for CO into its individual dissociation channels, as shown in Fig. 7.6. The dissociation processes are mapped out by calculating fragments' kinetic energies (see Appendix C). For simplification, the dissociation channel $CO^{(A+B)+} \Rightarrow C^{A+} + O^{B+}$ will henceforth be described by the notation (A, B). We observe the asymmetry in nearly all of the highly-charged fragment dissociation channels for CO. Interestingly, however, the oscillation in the (2,0) channel is significantly suppressed compared to the (2,1) and (2,2) channels. We address this effect later in section 7.4.

It is important to mention that the size of our detected signal oscillation is influenced by a number of experimental limitations. The phase noise of the Mach-Zehnder interferometer is extremely sensitive to vibrations, since one full cycle of the 400 nm light is only ~ 1.3 fsec in duration. Temperature changes and air currents can also alter the relative beam

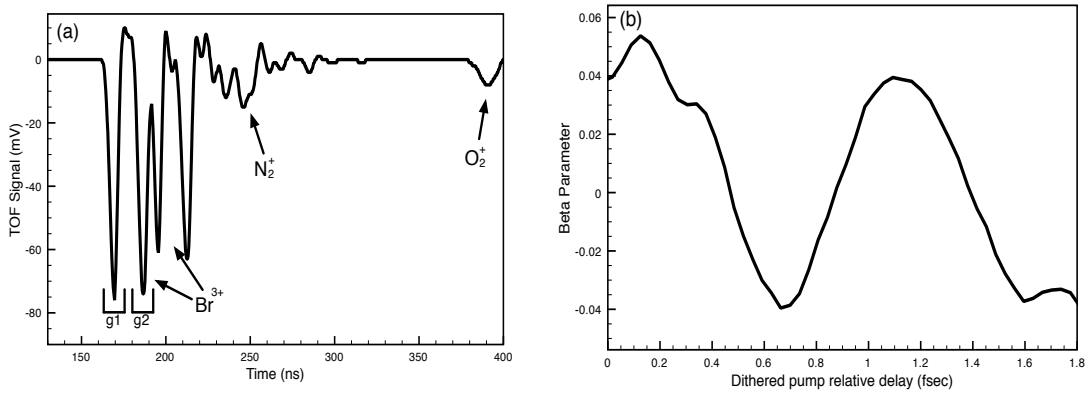

Figure 7.7: (a) TOF spectrum of HBr with an explosion pulse polarized parallel to the spectrometer axis. Gates were aligned with the $^{79}Br^{3+}$ fragments being ejected towards and away from the detector. (b) The resultant asymmetry is detected.

path lengths. Tunnel ionization saturation effects also tend to obscure the asymmetry, as does detector saturation (e.g. simultaneous measurement of the asymmetries of multiple charge states, like C^{2+} and C^+, are not always possible due to the often drastic difference in current mode signal size). Additionally, the probe beam likely overlaps a range of phases of the 2-color beam (due to their non-collinearity). The molecules might still be dissociating asymmetrically, but with equal and opposite contributions within the probe's focal volume. Despite these effects, we consistently are able to retrieve a clear asymmetry.

We then examined the influence of the asymmetric field on HBr dissociation. The molecules are rotationally cooled by the supersonically-expanded gas jet in the Physics lab. As with CO, we find a pronounced asymmetry, e.g. in the Br^{3+} fragments. We expect that the asymmetry parameter for the dissociation is maximized when the 2-color laser field has its maximum asymmetry. In an attempt to determine if this is indeed the case, the oscillation signal is compared to the total signal of the N_2^+ molecular ion which is collected simultaneously. The N_2^+ tunneling ionization yield is maximized at phases

which produce the largest peak field, i.e. maximum field asymmetry. Thus, maxima in the N_2^+ signal allow us to define the maximum pump field asymmetry. However the yield is independent of the sign of the field asymmetry. We therefore expect maxima in the N_2^+ yield to occur with twice the frequency of extrema in β as the phase is varied. Indeed, we find that the molecular ion signal oscillates at twice the frequency of the Br^{3+} asymmetry, and that the extrema in β occur at the same phase as maxima in the N_2^+ yield. Therefore, the peaks in the asymmetry signal correspond to the maxima in the laser field strength.

Nitrogen is used as the final sample molecule in the dissociation experiments. For this homonuclear molecule, we search for phase-dependent variations in the direction of ion fragments in different charge states produced via asymmetric dissociation (e.g. $N_2^{3+} \rightarrow N^{2+} + N^+$). We find a clear asymmetry in the (2,1) dissociation channel (using the same (A,B) notation), shown in Fig. 7.8. As expected, there is no variation in the symmetric (2,2) channel. We do not see this effect in either of the visible N^+ dissociation channels (the (1,2) peaks should exhibit the same asymmetry, but they are too close to the (1,1) channel to be resolved).

Once the asymmetry is observed in the three diatomic species, we scan the probe beam delay out to both the half and full rotational revival times to examine the TOF spectra for traces of field-free orientation. Similar to the signal at the T=0 overlap, if transient orientation occurs, we expect to see a fluctuation in the β parameter between the charge states as the phase between the two-color pumps is adjusted. No field free orientation is detected, however, at T_{rot} or $T_{rot}/2$, despite the distinctive asymmetry seen at T= 0. Nevertheless, the distinct directionality observed in the experimental fragmentation results has indicated that the field induced asymmetry is very pronounced. We attempt to observe dynamical behavior near the T=0 overlap, given that the detected asymmetry is limited to this region. As noted by Corkum *et al.* there is a characteristic alignment time T_0 after

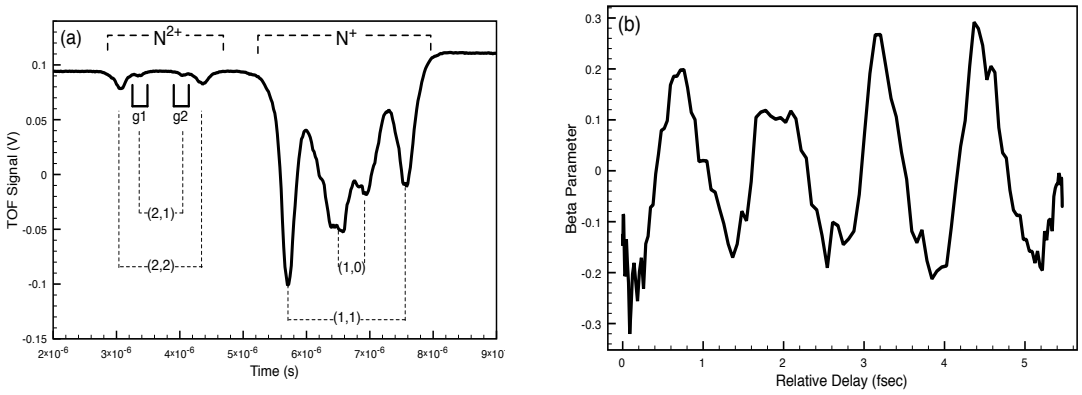

Figure 7.8: (a) TOF spectrum of N_2 (left) and dissociation asymmetry detected between the fragment peaks of the (2, 1) dissociation channel (shown by the two gates). (b) The resultant asymmetry from (a). No asymmetry is detected in the N^+ dissociation channels (1,0) or (1,1).

the peak intensity of a short laser pulse during which the rotational wavefunction initially aligns [5]. They note that for nitrogen, $T_0 \sim 65$ fsec. In Fig. 7.9 we plot the oscillation strength of the dithered two-color overlap signal in CO against the overlap enhancement signal from only a red pump and red probe. CO molecules are comparable in size to nitrogen molecules, and we expect that the transient orientation effect would exhibit a similar characteristic time (T_0). The detected asymmetry, however, does not appear to have any noticeable dynamic shift. Clearly the observed phase-dependent modulations in the direction of the ion fragments is due to strong-field dressing of the molecule.

7.4 Discussion

We now consider our results in terms of the numerous physical phenomena that can occur during a molecule's interaction with a strong field. While dissociating CO with the asymmetric field, we find that the (2,1) and (2,2) dissociation channels show a definite

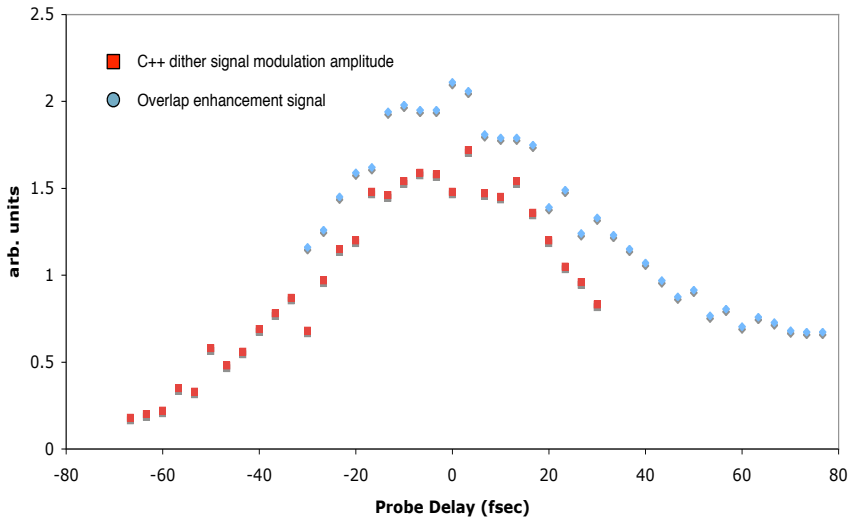

Figure 7.9: The lack of apparent dynamics around the temporal overlap of the two-color pumps and probe. The probe is scanned through the T=0 overlap with both pumps (and the asymmetry oscillations) present and with just the red pump. We anticipate a value of $T_0 \sim 65$ fsec for the molecule to initially orient to an applied laser field.

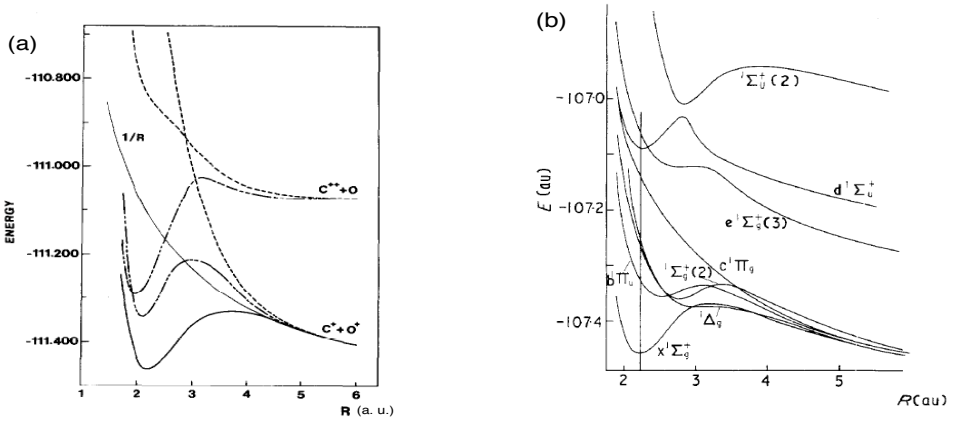

Figure 7.10: Calculated potential energy curves for the doubly-ionized $^1\Sigma^+$ states: (a) CO^{2+} and (b) N_2^{2+}. Calculations taken from [95] and [96]. Also shown in (a) is the pure Coulomb repulsion curve q1q2/R = 1/R.

asymmetry, while the (2,0) channel is strongly suppressed. At this point it is important to note that when two electrons are rapidly removed from a diatomic molecule (at least the molecules with many occupied inner shells) at its equilibrium internuclear distance, R_e, the molecular ion still retains a high degree of electronic sharing between the nuclei. This is evident in the calculated potential energy curves for the molecular dications CO^{2+} and N_2^{2+}, shown in Fig. 7.10 [95, 96]. CO and N_2 are isoelectronic counterparts, and their dicationic states exhibit complex structure, with the most notable features being the metastable bound states near R_e. Such structures are often brought about by an avoided crossing between an attractive (2,0) potential, caused by the charge-induced-dipole in the neutral fragment, and a (1,1) channel which is purely repulsive [97]. This can also be viewed as an asymmetrically dissociating channel (A+2, A) undergoing a charge transfer to a symmetric channel (A+1, A+1). Experimental evidence in support of this effect has been observed by Gibson *et al* [26]. To analyze the TOF spectra from these lower-charged dissociation channels, we use the potential energy curves (when possible) to infer

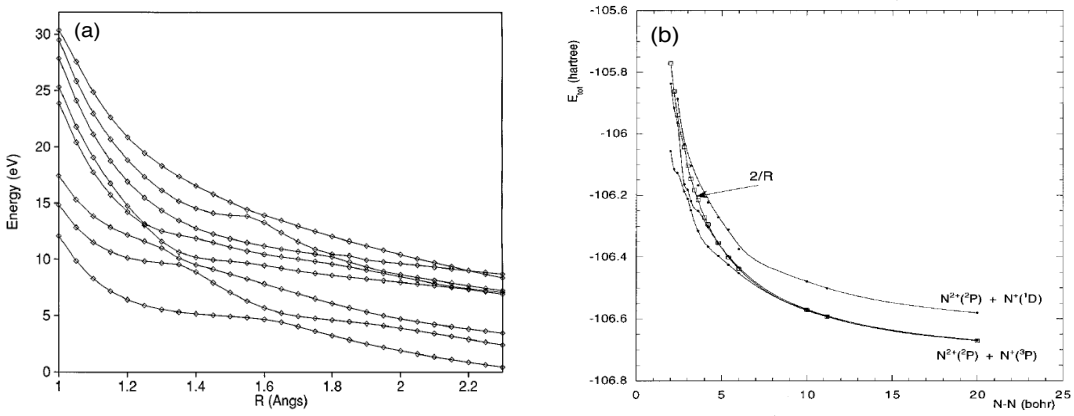

Figure 7.11: Calculated potential energy curves for the triply-ionized molecular states with $^2\Pi$ symmetry: (a) CO^{3+} and (b) N_2^{3+}. Calculations taken from [98] and [99]. Also shown in (b) is the pure Coulomb repulsion curve q1q2/R = 2/R.

the dynamics. For instance, we obtain the final kinetic energy of the CO (2,0) fragments from the TOF spectra, and by comparison with calculated plots (like 7.10a) of the lowest energy curves for the CO dication, we infer that the ion was likely formed near R $\sim$ 3 (a.u.). This is close to the equilibrium distance, $R_e = 2.1$ (a.u.), and noticeably less than the critical R_C for enhanced ionization (described in section 1.2.2) predicted by Chelkowski and Bandrauk [24], where

$$R_C \simeq \frac{4.07}{I_{p,CO}} = 7.9 \ a.u. \tag{7.1}$$

Only when a third electron is removed, does the molecular ion begin to represent two separate Coulomb potentials (see cartoon in Fig. 1.2). Numerically generated potential energy curves (seen in Fig. 7.11) also show that there are no bound states present in the tricationic states of either CO or N_2. Although there is some visible structure for small internuclear distances, the curves predominantly follow a near-Coulomb potential. In this particular molecular picture, the enhanced ionization model [20, 25] from section 1.2.2 becomes more relevant. We measure the kinetic energies of every charged fragment

CO Dissociation Channel (n,m)	$KE_{meas}(eV)$	R_C(basic) a.u.	R_C(pathway from i,j) a.u.
(1,1)	4.2	6.4	-
(1,2)	8.8	6.2	5.92 (1,1)
(2,1)	8.1	6.7	6.99 (1,1)
(2,2)	15.6	7.0	7.25 (2,1) , 8.0 (1,2)
(3,1)	12.4	6.6	6.32 (2,1)
(3,2)	22	7.05	8.49 (3,1) , 8.51 (2,2)

Table 7.1: Table of critical internuclear distances, R_C for various dissociation channels, derived from the measured fragment kinetic energies from Fig. 7.6. $R_{eq} = 2.1$ a.u. for CO. Values are first calculated by simply equating the measured final kinetic energies with the initial resting potential energy $q_1 q_2/R$. Secondary values of R_C are calculated by factoring in the kinetic energies obtained by previous ionization steps [26].

and determine the fragments' original internuclear distance at the moment the parent molecular ion is formed. This can be simply approximated by equating the final measured kinetic energy with the initial resting potential energy at the moment the ionic state is produced, and this is shown in Table 7.1. Also listed are calculations based on the inclusion of the kinetic energies accrued from all previous ionization steps. Gibson *et al.* state this equation in the form [26]:

$$R_{n,m}(a.u.) = \frac{nm - ij}{KE_{n,m} - KE_{i,j}} \tag{7.2}$$

where (n,m) is the final dissociation channel, and (i,j) is the immediately prior channel. We verify that subsequent fragmentation beyond the (1,1) channel occurs at a value of R= 7.1 ± 0.9 a.u., which agrees closely with the predicted value for R_C above.

Referring now to our experiment with CO, it is not surprising that the asymmetry in the (2,0) channel is suppressed, as the molecule cannot be simply treated as enhanced ionization from a pair of Coulomb potentials. Also, Figure 7.12 reveals the relative invariance of the dissociation asymmetry with respect to either the probe beam intensity or the

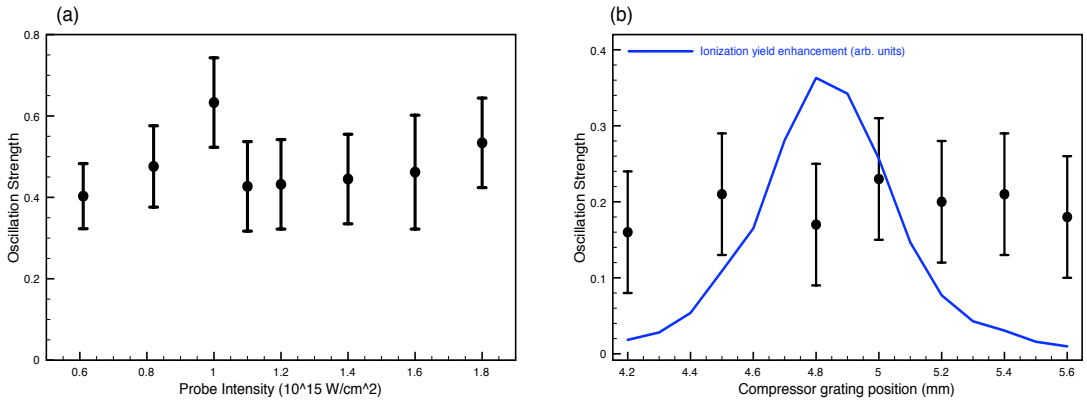

Figure 7.12: (a) Plot of the independence of the asymmetry in CO as a function of the probe intensity. (b) Plot of the dissociation asymmetry in CO vs. the pulse duration. In this plot, the compressor was adjusted to linearly chirp the laser pulses onto either side of the transform-limit. The maximum chirp shown here is approximately 250 fsec (from a minimum of 30 fsec).

laser pulse duration. This invariance was also seen by Corkum *et al.* when they explored the localization effect in a general diatomic Coulomb potential (A_2^{n+}). We believe this confirms that the detected asymmetry is a product of the enhanced ionization effect at R_C.

The oscillations seen in the N^{2+} fragments from the (2,1) channel of dissociating nitrogen were compared to the O^{2+} oscillations from CO. We see that their asymmetries are in phase in Fig. 7.13, which means that the N^{2+} fragments in the (2,1) dissociation channel will be ejected in the same direction as O^{2+} fragments from the (2,1) and (2,2) channels of CO. This can be expected, as both detected fragments tend to have higher IP's than their explosion partners (N^+ and C^+ or C^{2+}, respectively). Although this in-phase behavior is clearly visible, and though the HBr oscillation data allows us to correlate the peak field with the peak asymmetry, we are unable to currently detect the absolute phase of field oscillation at the laser focus. A measurement of this kind has been made before

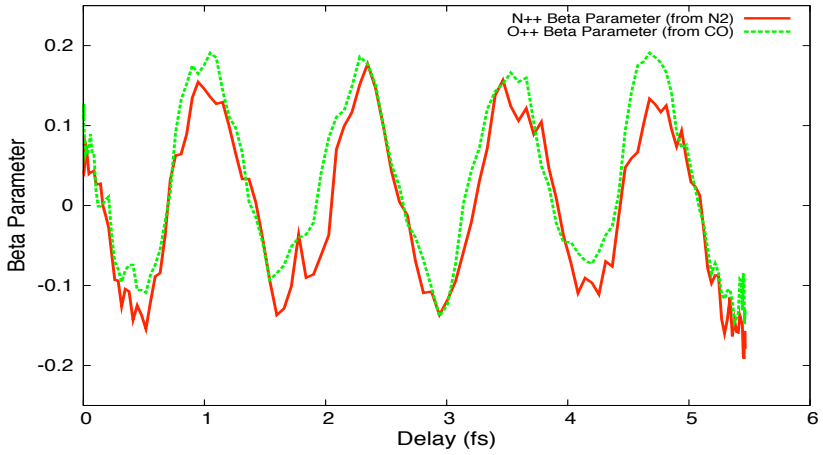

Figure 7.13: Measuring the dissociation asymmetry for two molecules in rapid succession (to minimize laser drift).

by Schumacher *et al* [100], but in general it is quite challenging, as the beam must be inspected interferometrically within the chamber near the laser focus. Additionally, the ω and 2ω pump beams both undergo a π phase shift through the focus, and the uncertainty in the location of the noncollinear pump-probe overlap makes it extremely difficult to know precisely which part of the two-color beam is responsible for the oscillation signal.

In any heteronuclear molecule, there is uneven charge sharing between the nuclei. In Fig. 7.14, we illustrate how a molecular ion with uneven charge sharing behaves when a static field is applied parallel or antiparallel to the dipole moment. The fields we generate have stronger peaks in one direction versus another, which can significantly affect the barrier heights for further tunneling. The intermediate and lower barrier heights show a distinctive asymmetry when the field points in either direction. Even though the relative change in barrier height is not large between the forward and backward directions, the

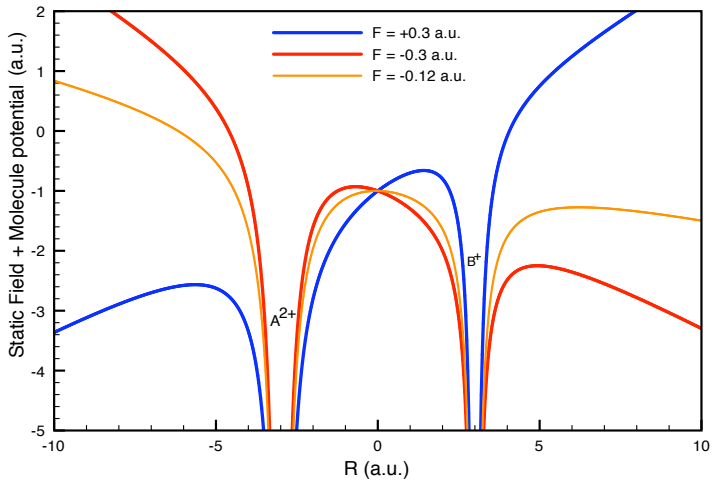

Figure 7.14: Picture of an electron in a double-Coulomb well potential, with a static electric field applied along either direction. Note the difference between the difference between the outer barrier heights in the blue vs. orange curve. This would surely result in a preferential dissociation.

tunnel-ionization effect is highly nonlinear. Therefore the asymmetry effect can still be quite large. Kamta and Bandrauk saw similar behavior when they studied this behavior of nonsymmetric molecules (in particular, HeH^{2+}) exposed to a few-cycle CE-phase stabilized pulse [88]. They represented molecules with weaker charge asymmetries than HeH^{2+} by incorporating non-integer values for the core charges Z_i. Strong dissociation asymmetries were still observed despite this, and we can infer that the asymmetric charge distributions we have accessed in homo- and heteronuclear molecules should exhibit a similar dissociation preference.

It is also worth noting that a recent paper [101] by C. Guo found that the presence of the metastable CO^{2+} likely results from nonsequential double ionization (NSDI), whereas processes which follow a purely dissociative path originate from a more sequential mechanism. NSDI is characterized as the ionization that occurs when an electron tunnels through

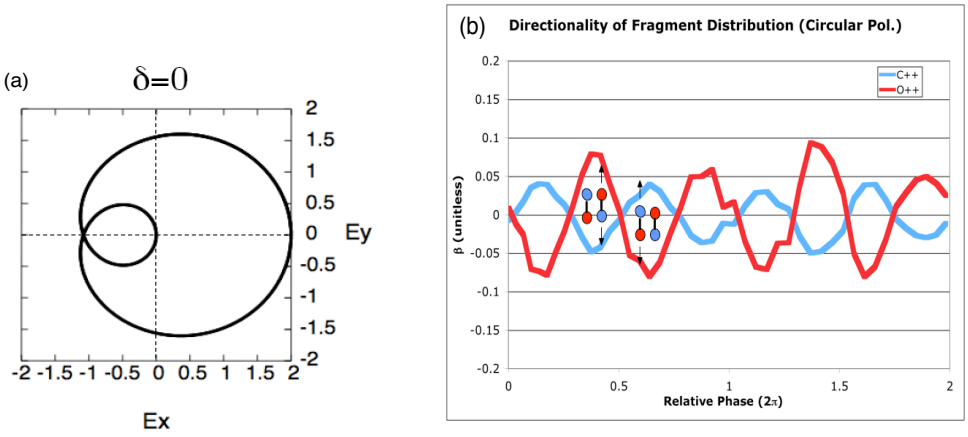

Figure 7.15: (a) E-field profile $\mathbf{E}_{tot} = \mathbf{E}_{780nm} + \mathbf{E}_{390nm}$ for circularly polarized pump light, where $\mathbf{E}_{780nm} = E_x \cos(\omega t)\hat{\mathbf{i}} + E_y \sin(\omega t)\hat{\mathbf{j}}$ and $\mathbf{E}_{390nm} = E_x \cos(2\omega t + \delta)\hat{\mathbf{i}} + E_y \sin(2\omega t + \delta)\hat{\mathbf{j}}$. (b) The resultant dissociation asymmetry from the overlap of the circularly-polarized pumps with a linearly-polarized probe.

a field-induced potential barrier, and then recollides with the molecular ion core due to the field swinging in the opposite direction, removing another electron in the process. If the field is not linearly-polarized, then the first electron cannot recollide with the core, and the NSDI process cannot occur. To examine the possibility that non-sequential processes play a role in the asymmetric dissociation, we repeat the measurement of the asymmetry of room temperature CO, using two circularly-polarized ω and 2ω beams. The combined pump field vector follows a path illustrated in Fig. 7.15a. The oscillation strength detected with the circular pump beams (Fig. 7.15b) is just as large as the asymmetry shown in Fig. 7.5b with linear pump beams. Therefore, the asymmetry seen in the (2,1) and (2,2) channels of CO most likely is caused by the sequential ionization process described above.

7.5 Conclusion

We have achieved a pronounced degree of asymmetry in the dissociation of highly charged fragments of diatomic molecules. The pump field asymmetry can be generated by an interferometric overlap of laser fields at ω and 2ω, with linearly or circularly polarized light. The pump intensity contribution is relatively small, and is noncollinearly overlapped with the strong linearly polarized probe pulse to generate the high dissociation channels. We find that lower dissociation channels, which in general have more complicated structure in their potential energy curves, have significantly suppressed signal oscillations when compared to the higher channels with more Coulombic potential energy curves. Also, the asymmetry appears in dissociation channels which seem to be formed at approximately R_C, in agreement with the enhanced ionization picture of a strong quasistatic field along the direction of the internuclear axis. We determine with a delayed probe, that no field-free orientation has been occurring, an experimental result which others have only been able to infer [91].

Chapter 8

Simulation of Transient Orientation

It is instructive to consider why no transient orientation was induced by the 2-color field in the experiments described in Chapter 7. Using a modification of the alignment rigid-rotor simulation, the effects of the asymmetric E-field on HBr and CO have been calculated [102]. Previous simulations ascribed in this dissertation utilize a laser-molecule interaction potential purely based on the molecular polarizability. The code (to compute orientation) was altered to include the hyperpolarizability as well. A similar method was used by Kanai and Sakai [103] in the adiabatic regime ($\tau_p >> \tau_{rot}$). The field is assumed to be a two-color laser field,

$$E(t) = E_0(t)\left[\cos(\omega t) + \gamma\cos(2\omega t + \phi)\right] \tag{8.1}$$

At frequencies much greater than the molecular rotational constant, and for many field oscillations within the pulse duration, the permanent dipole interaction term averages to

zero. The remaining total time-averaged interaction potential is represented by

$$\begin{aligned} W_{tot} &= W_{pol} + W_{hyperpol} \\ &= -\frac{(E_0(t))^2}{2}(1+\gamma^2)\left[\alpha_\perp + \Delta\alpha\cos^2\theta\right] \\ &\quad -\frac{(E_0(t))^3}{8}\gamma\cos(\phi)\left[3\beta_\perp\cos\theta + (\beta_\parallel - 3\beta_\perp)\cos^3\theta\right] \end{aligned} \tag{8.2}$$

where we define:

$$\begin{aligned} \beta_\parallel &= \beta_{zzz} \\ \beta_\perp &= \beta_{zxx} = \beta_{xzx} = \beta_{xxz} \\ &= \beta_{zyy} = \beta_{yzy} = \beta_{yyz} \end{aligned} \tag{8.3}$$

with β_{ijk} as the elements of the rank-3 hyperpolarizability tensor, and z is chosen as the quantization axis.

The polarizability component couples states with $\Delta J = even$ (0, $\pm$2), as before. The hyperpolarizability term allows states with $\Delta J = odd$ ($\pm$1, $\pm$3) to be coupled as well, resulting in a wavepacket with indefinite parity. As with the alignment code (described in Appendix A), the coherent population redistribution from a single, initial rotational state is computed. The evolution of the rotational wavepacket is then computed for a range of time delays following the 2-color field pulse. Time-dependent expectation values for various moments of the angular distribution are computed and averaged over a Boltzmann distribution of initial states to simulate the thermal ensemble. In particular, the orientation parameter $\langle\cos\theta\rangle(t)$ is computed, as shown in Fig. 8.1. We note that there is a significant dependence of the degree of orientation on the rotational temperature, particularly at the half-revival times. The sensitivity of the half-revival structures to

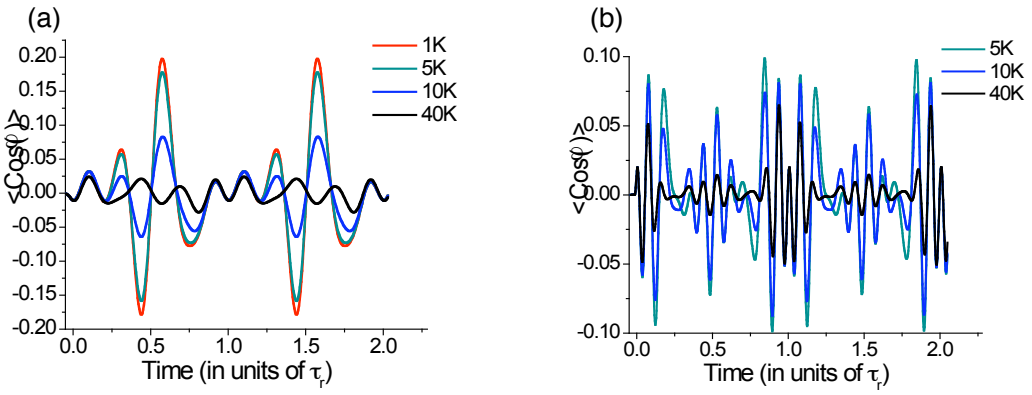

Figure 8.1: Calculations [102] of field-free orientation for (a) HBr and (b) CO with $\gamma = 1$. The degree of orientation is represented by $\langle \cos\theta \rangle(t)$. The delay axis is given in terms of the full rotational period, τ_{rot}. The temporal structure in the CO plot is more dense, because a broader range of $|J\rangle$ states is populated in CO (its rotational levels are much more closely spaced than HBr's).

the temperature likely arises from the interferences of the odd/even Raman transitions towards or away from each $|J\rangle$ state. As shown in section 3.2.4 for transient alignment, the rotational state distribution has a significant impact on the temporal revival structure.

In the experiment, although we utilized two pumps which could separately align the CO molecules, no transient orientation has been detected. It is not surprising that the room temperature molecules do not exhibit detectable orientation, in light of the temperature dependence seen in the simulations. For the molecules cooled by the supersonic expanding gas jet, the extracted values earlier in this thesis ranged from 15 K to 35 K. Based on Fig. 8.1, we are on the outer edge of orientation detection, and an improved molecular-beam cooling design could greatly improve our chances for observing it.

Chapter 9

Summary and Conclusions

We have observed the influence of intense, ultrashort laser pulses on diatomic molecules at room temperature and ∼25 K. In particular, we populate a coherent superposition of rotational states, study the resultant transient alignment dynamics, and extract information about the molecular electronic structure. After the laboratory equipment is detailed in Chapter 2, the techniques for generating and detecting transient alignment are described in Chapter 3. We observe the alignment using both (1) a quantitative technique with a helical delay-line anode and (2) a qualitative technique with temporal information from a single-stage time-of-flight spectrometer. Inspection of the coherently populated $|J\rangle$ states provides us with a good estimate of the rotational temperature of CO samples from the two experimental chambers, when compared with results from a rigid-rotor based simulation of the evolving rotational wavepacket.

In the next two chapters, we study the electronic response in a diatomic molecule to an applied intense laser field, by observing the transient alignment efficiency. In Chapter 4, we utilize a ratiometric technique to compare the alignment-dependent ionization rates of CO with those of its companion atom, Kr. We extract a functional form for the ionization

rate anisotropy by fitting the delay-dependent moments to the ratiometric data, and we determine that the ionization probability is 2× greater for CO molecules aligned parallel rather than perpendicular to the laser polarization axis. This result is in agreement with existing MOADK calculations. In Chapter 5, we focus our attention on the study of the polarizability anisotropy of diatomic molecules. Using an identical pump pulse, we compare HBr's alignment efficiency to that of N_2, whose $\Delta\alpha$ is more well-documented. A rigid-rotor model is incorporated again, and the alignment simulations are fitted to the experimental results. We then minimize the χ-square value for the fit to both molecules' alignment data. We extract a value for the polarizability anisotropy of HBr, which is in good agreement with previously calculated values.

In Chapter 6 we utilize the qualitative alignment technique in combination with a GA and pulse shaper, to optimize the degree of alignment in a room temperature CO sample. We find some non-transform-limited pulses which perform as well as a transform-limited pulse, but none that perform noticeably better. The optimization runs for the experimental pulse shaping closely resemble the simulation-based GA scans, and control "knobs" for our time-domain parameterization were found, as was seen with the application of PCA. We conclude that, although the intensities used were sufficiently strong to ionize the CO molecules, the rigid-rotor model with constant anisotropic polarizabilities is sufficient to describe the alignment process.

Chapter 7 described the asymmetry seen in the fragmentation directionality of several diatomic molecules. We observe that with a relatively small $\omega+2\omega$ pump field and a much more intense Coulomb exploding probe field, the asymmetry is still quite pronounced. There is a significant suppression of the asymmetry in the (2,0) dissociation channel of CO, relative to the (2,1) and (2,2) channels. This indicates that molecular structure for $R < R_C$ still plays a dominant role in the fragmentation of the molecular dication. The

asymmetry, therefore, appears to be a product of the enhanced ionization effect at R_C. With the two pump beams set to approximately the same intensity, we detect transient alignment from each beam separately, but no transient orientation has been observed yet. In Chapter 8, we observe that a high rotational temperature is most probable limitation which is preventing the detection of transient orientation.

The experiments presented in this dissertation examine strong-field phenomena which are still being actively pursued by numerous researchers. For instance, Corkum *et al.* have recently followed up on earlier work by examining (experimentally and numerically) the angle-dependent ionization rate of the linear triatomic molecule CO_2, as well as those of N_2 and O_2 [104]. Faucher *et al.* use a genetic algorithm to optimize the simulated field-free alignment in O_2 molecules. Sakai *et al.* explore the use of pulse shaping experimentally to optimize alignment in rotationally cold N_2 molecules [76]. There is also ongoing experimental work into the improvement of high harmonic generation by aligned molecules, both in the Chemistry laser lab at UVA and abroad [9, 105, 106].

Field-free orientation also remains a hot topic in the study of strong-field molecular interactions. Ohmura *et al.* continue to study the directionally asymmetric dissociation of molecules such as OCS and CH_3Br with two-color phase controlled laser fields [107]. Tehini and Sugny present new calculations which study field-free orientation effects as a result of two-color laser field interacting with the polarizability and hyperpolarizability of a heteronuclear molecule [108] following earlier work [103]. Sakai *et al.* have very recently proposed a new technique to achieve transient orientation using the combination of an electrostatic field and a rapidly shut-off laser field [109]. Experiments with ultrafast $\omega + 2\omega$ fields are continuing in both the Chemistry and Physics labs here at UVA.

We have thus demonstrated the tremendous versatility of ultrafast laser pulses when applied to the analysis or manipulation of diatomic molecules. The high intensities (I >

1×10^{15} W/cm^2) in ultrashort pulses also permit us to precisely probe the spatial alignment of the nuclei with Coulomb explosion. In the quantum picture, the broad bandwidth of the light allows us to create broad wavepackets of high-lying rotational states. The resultant alignment effect will continue to be a valuable tool for molecular physicists, since the preparation of anisotropic, field-free molecular samples now enables measurements with unprecedented precision. Further knowledge of a molecule's electronic, rotational, and vibrational dynamics can lead us to be able to selectively prepare desired quantum states or to force a molecule down a chosen dissociation pathway. Also, techniques like the genetic algorithm/PCA method from Chapter 6 can paint a unique picture of the underlying molecular dynamics, and it can be readily applied to numerous molecular physics experiments. Ideally, we hope that all the experiments presented here can serve as useful stepping-stones along the path to quantum control [110].

Appendix A

Rigid Rotor Simulation

A.1 Classical Rotor

A classical rigid rotor can be viewed as a dumbbell consisting of two atoms (m_1, m_2) joined along an axis. It has a moment of inertia given by I = $m_r R^2$, where m_r is the reduced mass and R is the internuclear distance. The magnitude of the rotor's angular momentum is defined as L=I$\omega_{_R}$, and its energy is

$$E_{rot} = \frac{1}{2} I \omega_{_R}^2 = \frac{L^2}{2I} \tag{A.1}$$

When a light wave of frequency ω_i is incident upon such a molecule, the polarizability appears to be time-dependent in the lab frame, with $\alpha(t) = \alpha_0 + \Delta\alpha \cos 2\omega_R t$. The induced dipole moment ($\mu = \alpha E$) can be expressed as [33],

$$\begin{aligned} \mu_{ind} &= (\alpha_0 + \Delta\alpha \cos 2\omega_{_R} t)(E_i \cos \omega_i t) \\ &= \alpha_0 E_i \cos \omega_i t + E_i \Delta\alpha \cos 2\omega_{_R} t \cos \omega_i t \\ &= \alpha_0 E_i \cos \omega_i t + \frac{1}{2} E_i \Delta\alpha [\cos(\omega_i + 2\omega_{_R})t + \cos(\omega_i - 2\omega_{_R})t] \end{aligned} \tag{A.2}$$

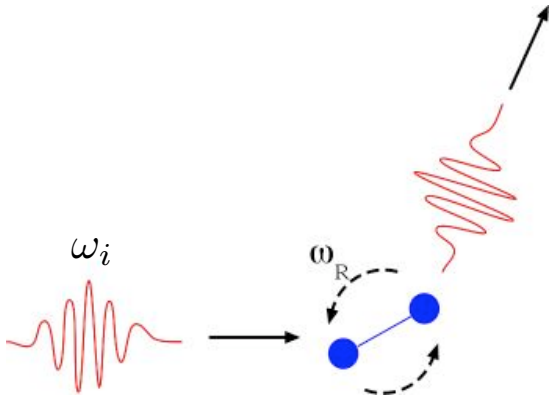

Figure A.1: Cartoon of a light wave scattering from a classical rigid rotor.

The induced dipole, having been created by the field, then receives a torque from the field,

$$|\tau| = |\vec{\mu} \times \vec{E}| \propto (E\cos\theta)E\sin\theta = \frac{E^2}{2}\sin 2\theta \tag{A.3}$$

For small angles, the molecule receives a torque $\tau \propto \theta$, and this increases as the molecules oriented closer to the plane perpendicular to the applied field.

A.2 Quantum Rotor Simulation

If we treat the molecule quantum mechanically, the solution of the Schrödinger equation for a rigid rotor gives the discrete energy levels

$$E_{rot} = \frac{\hbar^2}{2I}J(J+1) = B_0 J(J+1) \ \ (a.u.) \tag{A.4}$$

where B_0 is the ground state rotational constant. The relative population of initial rotational levels can be expressed as the ratio of the Boltzmann distribution over the partition

function over all the states,

$$Relative\ \ population = \frac{w_J(2J+1)e^{-B_0 J(J+1)/(k_B T)}}{Z} \tag{A.5}$$

where the $(2J+1)$ factor arises from the m values being equally populated for every J value, and the w_J accounts for the statistical weights of the even vs. odd J values, as described in section 3.2.4. The partition function can be written as

$$Z = \sum_{J=0}^{\infty}(2J+1)e^{B_0 J(J+1)/(k_B T)} \Rightarrow \int_0^{\infty}(2J+1)e^{-B_0 J(J+1)/(k_B T)}dJ = \frac{k_B T}{B_0} \tag{A.6}$$

The internuclear bond is allowed some flexibility (to provide a more realistic model), and an extra term is added to the rotation energy to account for the centrifugal distortion,

$$E_{rot} = B_0 J(J+1) - D_0 J^2(J+1)^2 \tag{A.7}$$

The Raman excitation process can be viewed as a photon scattering off a virtual state. The incoming and outgoing photon each exchange one unit of angular momentum with the molecule, resulting in $\Delta J = 0, \pm 2$ transitions. This is analogous to the classical result seen in Eq. A.2. The usual method for quantifying the spatial alignment of a diatomic molecule is by $\cos^2\theta$, where θ is the angle between the molecular axis and a fixed spatial axis, and this is typically the laser polarization direction. We simulate the Raman scattering by evaluating the matrix elements of the laser+molecule Hamiltonian time averaged over the rapid optical field oscillations,

$$\mathbf{H} = B\mathbf{J}^2 - \frac{1}{4}E(t)^2\Delta\alpha\cos^2\theta \tag{A.8}$$

where $E(t)$ is the E-field envelope of the laser pulse. The coupling coefficients between the

various rotational states therefore is expressed as $\langle J, M|\cos^2\theta|J', M\rangle$ (note that different M values are not coupled because of the cylindrical symmetry of the interaction potential). The rotational states $|J, M\rangle$ of a diatomic molecule are characterized by the spherical harmonics $Y_J^M(\theta, \phi)$, and $\cos^2\theta$ can be expressed similarly,

$$\cos^2\theta = \left(\sqrt{\frac{4\pi}{2J+1}}\right)\frac{2}{3}Y_2^0(\theta,\phi) - \frac{1}{3} \tag{A.9}$$

Calculation of the coupling proceeds by evaluating the integral,

$$\langle J, M|Y_2^0|J', M\rangle = \int\int Y_J^{M*}Y_2^0Y_{J'}^M d\theta d\phi. \tag{A.10}$$

This integral can be rewritten in terms of the Wigner 3-j symbols, which are tabulated in the literature [111]. By factoring the only allowed transitions, the relevant coupling coefficients become

$$V_{J,J} = \frac{2J(J+1) - 2M^2 - 1}{(2J+3)(2J-1)},\ \ V_{J,J-2} = \sqrt{\frac{(J^2-M^2)((J-1)^2-M^2)}{(2J+1)(2J-1)^2(2J-3)}} \tag{A.11}$$

After the superposition of $|J\rangle$ states has been populated during the interaction with the laser pulse, and the resultant wave packet is propagated in time by a 2nd-order Runge-Kutta algorithm [69]. The evolution of the alignment parameter is given by [5]

$$\begin{aligned}\langle\cos^2\theta\rangle(t) = \sum_J |a_J|^2\langle J|\cos^2\theta|J\rangle + |a_J||a_{J-2}|e^{-i(E_J-E_{J-2})\Delta t}\langle J|\cos^2\theta|J-2\rangle \\ +|a_J||a_{J+2}|e^{-i(E_J-E_{J+2})\Delta t}\langle J|\cos^2\theta|J+2\rangle\end{aligned} \tag{A.12}$$

where $|a_J|$ are the $|J\rangle$-state amplitudes in the wave packet. This alignment parameter is averaged over the weighted Boltzmann distribution of incoherent initial states. The time-dependent angular probability distribution of the molecular wavefunction can also

be generated by the superposition of the spherical harmonics for the various states in the wavepacket.

Appendix B

Temporal Delays in a Glass Slab

This appendix presents some of the algebra involved in the calculation of the spatial and temporal shifts that occur when a rectangular shaped (parallel surfaces) piece of glass is inserted into a laser beam path. Figure B.1 and the following definitions apply:

d = thickness of individual glass piece

d'(θ) = thickness of glass through which light travels

a(θ) = transverse beam shift

b(θ) = longitudinal distance traveled in glass

y = arbitrary length enclosing the glass piece

θ = incident angle (relative to surface normal)

θ_r = refracted angle (relative to surface normal)

n = n(λ) = index of refraction of glass

n_g = $n_g(\lambda)$ = group index

First, beginning with Snell's law,

$$\sin\theta = n(\lambda)\sin\theta_r. \tag{B.1}$$

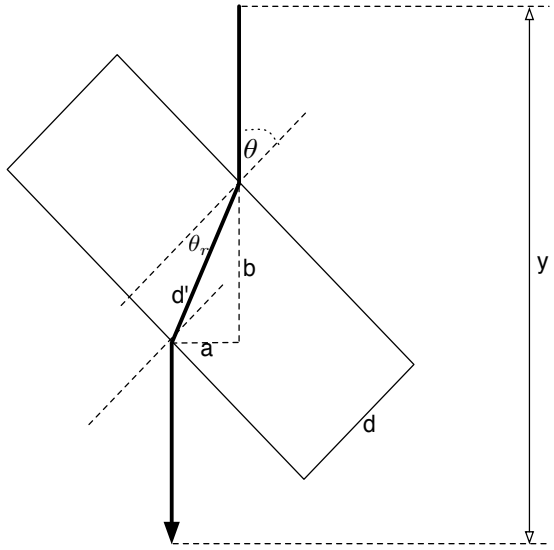

Figure B.1: The laser beam shift due to the insertion of a piece of glass.

For simplification, we define:

$$\gamma \equiv \gamma(\theta, \lambda) = \cos\theta_r = \cos\left(\sin^{-1}\left(\frac{\sin\theta}{n(\lambda)}\right)\right) \tag{B.2}$$

the total time to traverse the distance, y, with the tilted glass is,

$$t_{tot} = t_{air} + t_{glass} = \frac{y - b(\theta)}{c_0} + \frac{n_g d'(\theta)}{c_0} \tag{B.3}$$

where

$d'(\theta) = d/\cos\theta_r = d/\gamma(\theta, \lambda)$ and the group velocity is calculated by

$$n_g(\lambda) = n(\lambda) - \lambda\frac{dn}{d\lambda} \tag{B.4}$$

where values of $n(\lambda)$ and $\frac{dn}{d\lambda}$ can be obtained from the optical Sellmeier equation and

Table B.1: Table of Sellmeier equation coefficients (assuming λ is expressed in μm)

Material	B_1	B_2	B_3	C_1	C_2	C_3
BK7	1.0396E+0	2.318E-1	1.011E+0	6.001E-3	2.002E-2	1.036E+2
Fused Silica	6.962E-1	4.079E-1	8.975E-1	4.679E-3	1.351E-2	9.793E+1
CaF_2	5.676E-1	4.711E-1	3.848E+0	2.526E-3	1.008E-2	1.201E+3

its derivative,

$$\begin{aligned} n^2(\lambda) &= 1+\sum_{i=0}^{3}\frac{B_i\lambda^2}{\lambda^2-C_i} \\ \frac{dn}{d\lambda} &= \sum_{i=0}^{3}\left[\frac{B_i\lambda(\lambda^2-C_i)^{-1}-B_i\lambda^3(\lambda^2-C_i)^{-2}}{\sqrt{1+\sum_{j=0}^{3}B_j\lambda^2(\lambda^2-C_j)^{-1}}}\right] \end{aligned} \tag{B.5}$$

and the Sellmeier coefficients for a few commonly-used materials is given in Table B.1 [112].

From this information, the spatial and temporal shifts may be calculated.

$$\begin{aligned} a(\theta) &= d'\sin(\theta-\theta_r) \\ &= d'(\sin\theta\cos\theta_r-\sin\theta_r\cos\theta) \\ &= \frac{d}{\gamma}\left(\gamma\sin\theta-\frac{\sin\theta\cos\theta}{n(\lambda)}\right) \\ &= d\sin\theta\left(1-\frac{\cos\theta}{\gamma n(\lambda)}\right) \end{aligned} \tag{B.6}$$

We note that one can compensate for $a(\theta)$ using two identical slabs placed at angles θ and $-\theta$, respectively. The longitudinal distance traveled within the glass is,

$$\begin{aligned} b(\theta) &= d'\cos(\theta-\theta_r) \\ &= d'(\cos\theta\cos\theta_r+\sin\theta\sin\theta_r) \\ &= \frac{d}{\gamma}\left(\gamma\cos\theta+\frac{\sin^2\theta}{n(\lambda)}\right) \end{aligned}$$

$$= \quad d\cos\theta\left(1+\frac{\sin\theta\tan\theta}{\gamma n(\lambda)}\right). \tag{B.7}$$

The relative delay associated with a piece of glass at angle θ versus no glass at all (the delay imposed by inserting glass into the beam path)

$$\begin{aligned} t(\theta)-t_0 &= \left(\frac{y-b(\theta)}{c_0}+\frac{n_g d'}{c_0}\right)-\frac{y}{c_0} \\ &= \frac{1}{c_0}\left(n_g(\lambda)d'(\theta,\lambda)-b(\theta,\lambda)\right) \end{aligned} \tag{B.8}$$

The relative delay between two angles for a piece of glass can be calculated (at fixed wavelength) where $\gamma \equiv \gamma(\theta)$ with $\theta_2 > \theta_1$ and using equation B.8:

$$\begin{aligned} t(\theta_2)-t(\theta_1) &= \frac{1}{c_0}\left(n_g d'(\theta_2)-b(\theta_2)\right)-\frac{1}{c_0}\left(n_g d'(\theta_1)-b(\theta_1)\right) \\ &= \frac{1}{c_0}\left[b(\theta_1)-b(\theta_2)+n_g d\left(\frac{1}{\gamma(\theta_2)}-\frac{1}{\gamma(\theta_1)}\right)\right] \end{aligned} \tag{B.9}$$

The delay for a piece of glass at fixed angle θ between two frequencies can also be obtained from equation B.8, where $\mathrm{n}(\lambda_2) > n(\lambda_1)$ and noting also that $\gamma \equiv \gamma(\lambda)$

$$\begin{aligned} t(\lambda_2)-t(\lambda_1) &= \frac{1}{c_0}(n_g(\lambda_2)d'(\lambda_2)-b(\lambda_2))-\frac{1}{c_0}(n_g(\lambda_1)d'(\lambda_1)-b(\lambda_1) \\ &= \frac{1}{c_0}\left[b(\lambda_1)-b(\lambda_2)+d\left(\frac{n_g(\lambda_2)}{\gamma(\lambda_2)}-\frac{n_g(\lambda_1)}{\gamma(\lambda_1)}\right)\right] \end{aligned} \tag{B.10}$$

Appendix C

Time of Flight

This chapter serves as the basic theory for the operation of a single-stage time-of-flight mass spectrometer. The layout is shown in Figure C.1, a laser beam focuses onto a molecular sample in the interaction region at a position, x.

The newly formed ion with mass m and charge q is accelerated towards the detector by an amount

$$a = \frac{F}{m} = \frac{qE}{m} = \frac{qV}{ml_1} \tag{C.1}$$

Assuming the ion has an initial velocity, v_{0x}, along the spectrometer axis, its equations of motion in the first region are,

$$x = v_{0x}t_1 + \frac{1}{2}at_1^2, \;\; v_{fx}^2 = v_{0x}^2 + 2ax \tag{C.2}$$

where t_1 and t_2 are the times required to traverse the distances x and l_2, respectively. Solving this for t_1 and with $t_2 = l_2/v_{fx}$,

$$t = t_1 + t_2 \;\; = \;\; \frac{-v_{0x} + \sqrt{v_{0x}^2 + 2ax}}{a} + \frac{l_2}{\sqrt{v_{0x}^2 + 2ax}}$$

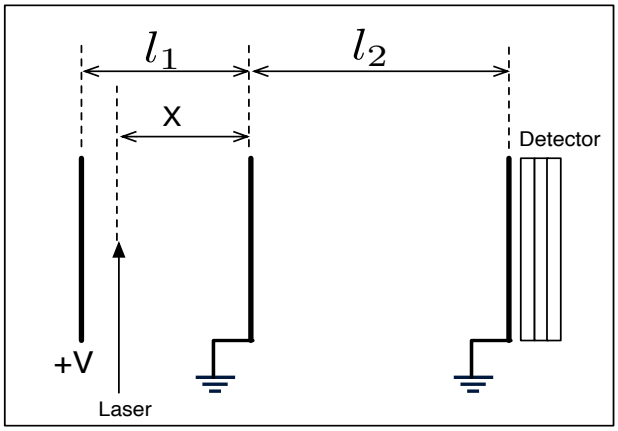

Figure C.1: Schematic side-view of a single stage time-of-flight mass spectrometer. An applied voltage, V, is placed on the first plate, while the two others are grounded.

$$= \frac{-v_{0x} + \sqrt{v_{0x}^2 + \frac{2qVx}{ml_1}}}{\frac{qV}{ml_1}} + \frac{l_2}{\sqrt{v_{0x}^2 + \frac{2qVx}{ml_1}}} \tag{C.3}$$

and for $v_{0x} = 0$ this reduces to:

$$t_0 = \sqrt{\frac{2x}{a}} + \frac{l_2}{\sqrt{2ax}} = \sqrt{\frac{2ml_1x}{qV}} + \frac{l_2}{\sqrt{\frac{2qVx}{ml_1}}} \tag{C.4}$$

The accuracy of these equations is verified by comparing the measured TOF values with the predicted ones. This is shown in Fig. C.2, where the TOF peaks for several ions are plotted for the two experimental chambers. The measured TOF values match well with the calculated curves, indicating that the ions see a nearly uniform static field throughout the spectrometer apparatus.

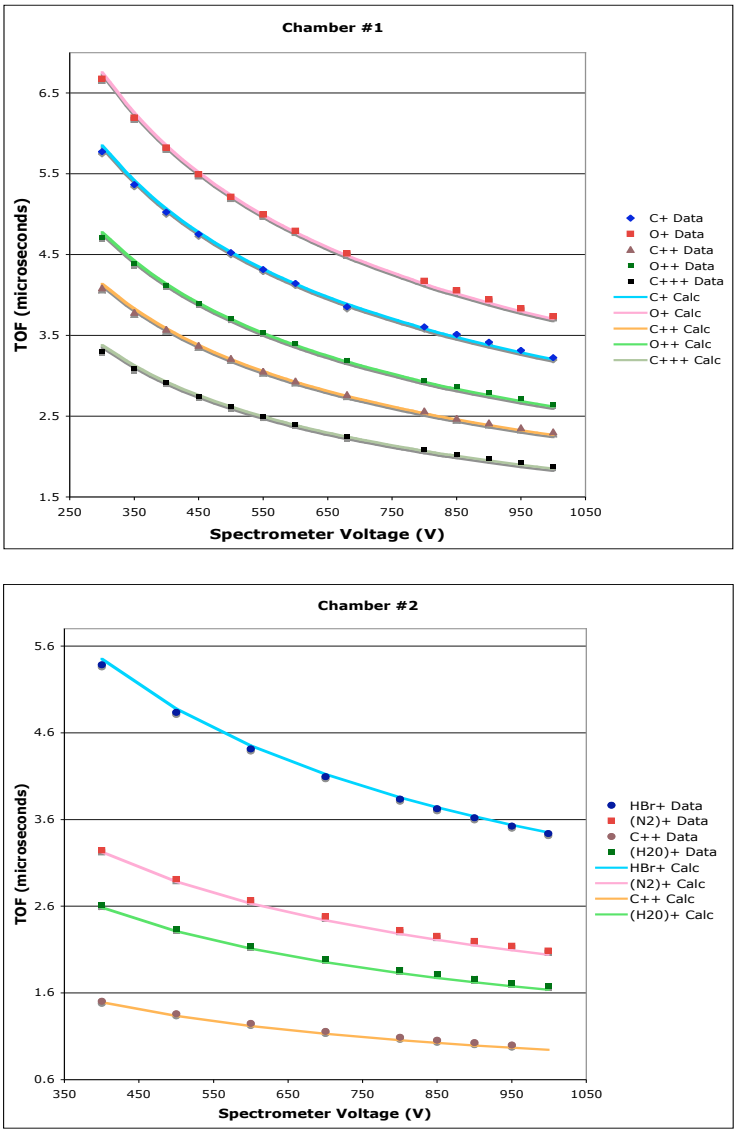

Figure C.2: The calibration curves for both experimental chambers.

C.1 Space Focusing

The TOF spectrometer is set up to achieve a basic level of spatial focusing. In other words, the spectrometer will compensate for ions produced over a range of positions (Δx) in the laser beam waist. This is accomplished by inspecting the variation in the time-of-flight about a fixed location x_0 [113],

$$\Delta t = t(x_0) - t(x_0 - \Delta x) = \sum_{n=1}^{\infty} \left(\frac{d^n t_0}{d(x)^n} \right)_{x-\Delta x} \frac{(\Delta x)^n}{n!} \tag{C.5}$$

Using equation C.4, we force the first term in this series to zero, which gives $x = l_2/2$, the required geometry to achieve first-order space focusing. Both TOF spectrometers used in our experiments are assembled with this condition in mind.

C.2 Fragment Kinetic Energies

When a diatomic molecule is fragmented along the spectrometer axis, the dissociation products have initial velocities towards, and away from, the detector. This manifests itself as a clear double peak for most of the dissociation channels in the TOF spectrum. This provides a way to calculate the kinetic energy of the fragments in that channel:

$$\begin{aligned} &t(+v_0) - t(-v_0) = \\ &\quad \frac{-v_{0x} + \sqrt{v_{0x}^2 + \frac{2qVx}{ml_1}}}{\frac{qV}{ml_1}} + \frac{l_2}{\sqrt{v_{0x}^2 + \frac{2qVx}{ml_1}}} - \frac{-(-v_{0x}) + \sqrt{(-v_{0x})^2 + \frac{2qVx}{ml_1}}}{\frac{qV}{ml_1}} + \frac{l_2}{\sqrt{v_{0x}^2 + \frac{2qVx}{ml_1}}} \end{aligned} \tag{C.6}$$

which reduces to

$$|\Delta t| = \frac{2v_{0x}ml_1}{qV} \tag{C.7}$$

and from this, the experimental fragment kinetic energy is calculated:

$$KE = \frac{1}{2}mv_{0x}^2 = \frac{q^2V^2\Delta t^2}{8ml_1^2} \tag{C.8}$$

This formula is useful to match up fragments from the same dissociation channel [114], particularly when the TOF spectra has numerous peaks, as in Fig. 2.8. It is critical that when measuring the energies of dissociation, the gas pressure in the interaction region should not significantly exceed 1×10^{-6} Torr in order to avoid space charge effects.

Bibliography

[1] E. Wells, M. J. DeWitt, and R. R. Jones. Comparison of intense-field ionization of diatomic molecules and rare-gas atoms. *Phys. Rev. A*, **66**:013409, (2002).

[2] M. J. DeWitt, E. Wells, and R. R. Jones. Ratiometric comparison of intense field ionization of atoms and diatomic molecules. *Phys. Rev. Lett.*, **87**:153001, (2001).

[3] X. M. Tong, Z. X. Zhao, and C. D. Lin. Theory of molecular tunneling ionization. *Phys. Rev. A*, **66**:033402, (2002).

[4] Xi Chu and Shih-I Chu. Role of the electronic structure and multielectron responses in ionization mechanisms of diatomic molecules in intense short-pulse lasers: An all-electron ab initio study. *Phys. Rev. A*, **70**:061402R, (2004).

[5] P. W. Dooley, I. V. Litvinyuk, K. F. Lee, D. M. Rayner, M. Spanner, D. M. Villeneuve, and P. B. Corkum. Direct imaging of rotational wave-packet dynamics of diatomic molecules. *Phys. Rev. A*, **68**:023406, (2003).

[6] I. V. Litvinyuk, K. F. Lee, P. W. Dooley, D. M. Rayner, D. M. Villeneuve, and P. B. Corkum. Alignment-dependent strong field ionization of molecules. *Phys. Rev. Lett.*, **90**:233003, (2003).

[7] D. Pinkham and R. R. Jones. Intense laser ionization of transiently aligned CO. *Phys. Rev. A*, **72**:023418, (2005).

[8] J. Itatani, J. Levesque, D. Zeidler, Hiromichi Niikura, H. Pepin, J. C. Kieffer, P. B. Corkum, and D. M. Villeneuve. Tomographic imaging of molecular orbitals. *Nature*, **432**:867, (2004).

[9] B. Sickmiller and R. R. Jones. High harmonic generation: Quasi-phase matching via transient molecular alignment. Doctoral Proposal, 2007.

[10] N. Hay, R. Velotta, M. Lein, R. de Nalda, E. Heesel, M. Castillejo, and J. P. Marangos. High-order harmonic generation in laser-aligned molecules. *Phys. Rev. A*, **65**:053805, (2002).

[11] T. Kanai, S. Minemoto, and H. Sakai. Quantum interference during high-order harmonic generation from aligned molecules. *Nature*, **435**:470, (2005).

[12] R. A. Bartels, T. C. Weinacht, N. Wagner, M. Baertschy, C. H. Greene, M. M. Murnane, and H. C. Kapteyn. Phase modulation of ultrashort light pulses using molecular rotational wave packets. *Phys. Rev. Lett.*, **88**:013903, (2002).

[13] V. Kalosha, M. Spanner, J. Herrmann, and M. Ivanov. Generation of single dispersion precompensated 1-fs pulses by shaped-pulse optimized high-order stimulated Raman scattering. *Phys. Rev. Lett.*, **88**:103901, (2002).

[14] B. Friedrich and D. Herschbach. Alignment and trapping of molecules in intense laser fields. *Phys. Rev. Lett.*, **74**:4623, (1995).

[15] J. J. Larsen, I. Wendt-Larsen, and H. Stapelfeldt. Controlling the branching ratio of photodissociation using aligned molecules. *Phys. Rev. Lett.*, **83**:1123, (1999).

[16] R. R. Jones. Atomic physics. Class Notes.

[17] M. V. Ammosov, N. B. Delone, and V. P. Krainov. Tunnel ionization of complex atoms and of atomic ions in an alternating electromagnetic field. *Sov. Phys. JETP*, **64**:1191, (1986).

[18] N. B. Delone and V. P. Krainov. *Multiphoton Processes in Atoms*. Springer Verlag, Berlin, Germany, 2000.

[19] K Codling and L. J. Frasinski. Dissociative ionization of small molecules in intense laser fields. *J. Phys. B.*, **26**:783, (1993).

[20] T. Seideman, M. Y. Ivanov, and P. B. Corkum. Role of electron localization in intense-field molecular ionization. *Phys. Rev. Lett.*, **75**:2819, (1995).

[21] C. Guo. Multielectron effects on single-electron strong field ionization. *Phys. Rev. Lett.*, **85**:2276, (2000).

[22] J. Muth-Bohm, A. Becker, and F. H. M. Faisal. Suppressed molecular ionization for a class of diatomics in intense femtosecond laser fields. *Phys. Rev. Lett.*, **85**:2280, (2000).

[23] L. J. Frasinski, K. Codling, P. Hatherly, J. Barr, I. N. Ross, and W. T. Toner. Femtosecond dynamics of multielectron dissociative ionization by use of picosecond laser. *Phys. Rev. Lett.*, **58**:2424, (1987).

[24] S. Chelkowski and A. D. Bandrauk. Two-step Coulomb explosions of diatoms in intense laser fields. *J. Phys. B*, **28**:L723, (1995).

[25] E. Constant, H. Stapelfeldt, and P. B. Corkum. Observation of enhanced ionization of molecular ions in intense laser fields. *Phys. Rev. Lett.*, **76**:4140, (1996).

[26] J. P. Nibarger, S. V. Menon, and G. N. Gibson. Comprehensive analysis of strong-field ionization and dissociation of diatomic nitrogen. *Phys. Rev. A*, **63**:053406, (2001).

[27] A. Zavriyev, P. H. Bucksbaum, H. G. Muller, and D. W. Schumacher. Ionization and dissociation of H_2 in intense laser fields at 1.064 microns, 532nm, and 355 nm. *Phys. Rev. A*, **42**:5500, (1990).

[28] A. Saenz. Behavior of molecular hydrogen exposed to strong dc, ac, or low-frequency laser fields. I. bond softening and enhanced ionization. *Phys. Rev. A*, **66**:063407, (2002).

[29] A. Zavriyev, P. H. Bucksbaum, J. Squier, and F. Saline. Light-induced vibrational structure in H_2^+ and D_2^+ in intense laser fields. *Phys. Rev. Lett.*, **70**:1077, (1993).

[30] H. Stapelfeldt and T. Seideman. Colloquium: Aligning molecules with strong laser pulses. *Rev. Mod. Phys.*, **75**:543, (2003). and references therein.

[31] D. A. Baugh, D. Y. Kim, V. A. Cho, L. C. Pipes, J. C. Petteway, and C. D. Fuglesang. Production of a pure, single ro-vibrational quantum state molecular beam. *Chem. Phys. Lett.*, **219**:207, (1994).

[32] J. Ortigoso, M. Rodriguez, M. Gupta, and B. Friedrich. Time evolution of pendular states created by the interaction of molecular polarizability with a pulsed nonresonant laser field. *J. Chem. Phys.*, **110**:3870, (1999).

[33] P. Atkins. *Physical Chemistry: Fifth Edition.* W. H. Freeman and Co., 1994.

[34] T. Seideman. Revival structure of aligned rotational wave packets. *Phys. Rev. Lett.*, **83**:4971, (1999).

[35] F. Rosca-Pruna and M. J. J. Vrakking. Revival structures in picosecond laser-induced alignment of I_2 molecules. II. numerical modeling. *J. Chem. Phys.*, **116**:6579, (2002).

[36] M. Leibscher, I. Sh. Averbukh, and H. Rabitz. Molecular alignment by trains of short laser pulses. *Phys. Rev. Lett.*, **90**:213001, (2003).

[37] C. Z. Bisgaard. *Laser induced alignment.* PhD thesis, University of Aarhus, 2006.

[38] Spectra-Physics, Mountain View, CA. *Millennia Vs: User's Manual*, 2001.

[39] Positive Light, Inc., Los Gatos, California. *Evolution-30 User Manual*, 2001.

[40] Kapteyn-Murnane Laboratories L.L.C., Boulder, Colorado. *Model MTS Mini Ti:Sapphire Laser Kit, Instruction Manual*, 2001.

[41] W. T. Silfvast. *Laser Fundamentals: 2nd Edition.* Cambridge University Press, 2004.

[42] R. L. Fork, O. E. Martinez, and J. P. Gordon. Negative dispersion using pairs of prisms. *Optics Letters*, **9**:150, (1984).

[43] J. Diels and W. Rudolph. *Ultrashort Laser Pulse Phenomena*. Academic Press, Inc., San Diego, CA, 1996.

[44] R. Trebino and D. J. Kane. Using phase retrieval to measure the intensity and phase of ultrashort pulses: frequency-resolved optical gating. *J. Opt. Soc. Am. A*, **10**:1101, (1993).

[45] K. W. Delong, R. Trebino, and D. J. Kane. Comparison of ultrashort-pulse frequency-resolved-optical-gating traces for three common beam geometries. *J. Opt. Soc. Am. B*, **11**:1595, (1994).

[46] Varian, Inc., Torino, Italy. *Turbo-V 1000HT pumps: technical information*, 1997.

[47] Stanford Research Systems, Sunnyvale, CA. *Model RGA200 Residual Gas Analyzer: Operating Manual*, 1996.

[48] A. Kantrowitz and J. Grey. A high intensity source for the molecular beam. part I. theoretical. *Rev. Sci. Inst.*, **22**:328, (1951).

[49] F. B. Dunning and R. G. Hulet, editors. *Atomic, Molecular, and Optical Physics: Atoms and Molecules*. Academic Press, 1996.

[50] W. C. Wiley and I. H. McLaren. Time-of-flight mass spectrometer with improved resolution. *Rev. Sci. Inst.*, **26**:1150, (1955).

[51] J. L. Wiza. Microchannel plate detectors. *Nuclear Instruments and Methods*, **162**:587, (1979). and references therein.

[52] M. B. Williams. *A photon counting imaging detector using MCP's with delay line readout*. PhD thesis, University of Virginia, 1990.

[53] Stanford Research Systems, Sunnyvale, CA. *Fast Gated Integrators and Boxcar Averagers*, 1993.

[54] Roentdek Handels GmbH, Frankfurt, Germany. *CoboldPC User Manual*, 2002.

[55] K. F. Lee, I. V. Litvinyuk, P. W. Dooley, M. Spanner, D. M. Villeneuve, and P. B. Corkum. Two-pulse alignment of molecules. *J. Phys. B*, **37**:L43, (2004).

[56] H Haken and H. C. Wolf. *Molecular Physics and Elements of Quantum Chemistry*. Springer-Verlag, 2004.

[57] H. F. Schaefer. *The Electronic Structure of Atoms and Molecules*. Addison-Wesley, Reading, Massachusetts, 1972.

[58] X.-M. Tong, 2005. Private Communication.

[59] R. S. Freund, R. C. Wetzel, and Shul. R. J. Measurements of electron-impact-ionization cross sections of N_2, CO, CO_2, CS, S_2, CS_2, and metastable N_2. *Phys. Rev. A*, **41**:5861, (1990).

[60] R. C. Wetzel, F. A. Baiocchi, T. R. Hayes, and R. S. Freund. Absolute cross sections for electron-impact ionization of the rare-gas atoms by the fast neutral-beam method. *Phys. Rev. A*, **35**:559, (1987).

[61] A. S. Alnaser, C. M. Maharjan, X. M. Tong, B. Ulrich, P. Ranitovic, B. Shan, Z. Chang, C. D. Lin, C. L. Cocke, and I. V. Litvinyuk. Effects of orbital symmetries in dissociative ionization of molecules by few-cycle laser pulses. *Phys. Rev. A*, **71**:031403R, (2005).

[62] M. P. Bogaard, A. D. Buckingham, R. K. Pierens, and A. H. White. Rayleigh scattering depolarization ratio and molecular polarizability anisotropy for gases. *J. Chem. Soc. Faraday Trans.*, **74**:3008, (1978).

[63] D. M. Bishop and P Norman. Effects of vibration on the polarizability and the first and second hyperpolarizabilities of HF, HCl, and HBr. *J. Chem. Phys.*, **111**:3042, (1999).

[64] H. K. Hughes. The electric resonance method of radiofrequency spectroscopy: The moment of intertia and electric dipole moment of CsF. *Phys. Rev.*, **72**:614, (1947).

[65] D. W. Johnson and N. F. Ramsey. Stark hyperfine structure of hydrogen bromide. *J. Chem. Phys.*, **67**:941, (1977).

[66] C. Asawaroengchai and G. M. Rosenblatt. Rotational Raman intensities and the measured change with internuclear distance of the polarizability anisotropy of H_2, D_2, N_2, O_2, and CO. *J. Chem. Phys.*, **72**:2664, (1980).

[67] S. Minemoto, H. Tanji, and H. Sakai. Polarizability anisotropies of rare gas van der Waals dimers studied by laser-induced molecular alignment. *J. Chem. Phys.*, **119**:7737, (2003).

[68] S. R. Langhoff, C. W. Bauschlicher Jr., and D. P. Chong. Theoretical study of the effects of vibrational-rotational interactions on the Raman spectrum of N_2. *J. Chem. Phys.*, **78**:5287, (1983).

[69] W. H. Press, S. A. Teukolsky, W. T. Vetterling, and B. P. Flannery. *Numerical Recipes in C: The Art of Scientific Computing, 2nd edition.* Cambridge University Press, Cambridge, UK, 1997.

[70] P. R Bevington. *Data Reduction and Error Analysis for the Physical Sciences.* McGraw Hill Book Company, New York, 1969.

[71] V. Renard, M. Renard, A. Rouzee, S. Guerin, H. R. Jauslin, B. Lavorel, and O. Faucher. Nonintrusive monitoring and quantitative analysis of strong laser-field-induced impulsive alignment. *Phys. Rev. A*, **70**:033420, (2004).

[72] F. Rosca-Pruna and M. J. J. Vrakking. Experimental observation of revival structures in picosecond laser-induced alignment of I_2. *Phys. Rev. Lett.*, **87**:153902, (2001).

[73] M. Renard, E. Hertz, S. Guerin, H. R. Jauslin, B. Lavorel, and O. Faucher. Control of field-free molecular alignment by phase-shaped laser pulses. *Phys. Rev. A*, **72**:25401, (2005).

[74] C. Horn, M. Wollenhaupt, M. Krug, T. Baumert, R. de Nalda, and L. Bañares. Adaptive control of molecular alignment. *Phys. Rev. A*, **73**:031401, (2006).

[75] S. Zamith, T. Martchenko, Y. Ni, S. A. Aseyev, H. G. Muller, and M. J. J. Vrakking. Control of the production of highly charged ions in femtosecond-laser cluster fragmentation. *Phys. Rev. A*, **70**:11201R, (2004).

[76] T. Suzuki, Y. Sugawara, S. Minemoto, and H. Sakai. Optimal control of nonadiabatic alignment of rotationally cold N_2 molecules with the feedback of degree of alignment. *Phys. Rev. Lett.*, **100**:033603, (2008).

[77] B. J. Pearson, J. L. White, T. C. Weinacht, and P. H. Bucksbaum. Coherent control using adaptive learning algorithms. *Phys. Rev. A*, **63**:063412, (2001).

[78] E. Wells, K. J. Betsch, C. W. S. Conover, M. J. DeWitt, D. Pinkham, and R. R. Jones. Closed-loop control of intense-laser fragmentation of S_8. *Phys. Rev. A*, **72**:063406, (2005).

[79] A. M Weiner. Femtosecond pulse shaping using spatial light modulators. *Rev. Sci. Inst.*, **71**:1929, (2000).

[80] D. Pinkham. Calibration and testing of an ultrafast laser diagnostic/shaping apparatus. Senior thesis, 2002.

[81] M. Hacker, G. Stobrawa, and T. Feurer. Iterative Fourier transform algorithm for phase-only pulse shaping. *Optics Exress*, **9**:191, (2001).

[82] E. P*é*ronne, M. D. Poulsen, H. Stapelfeldt, C. Z. Bisgaard, E. Hamilton, and T. Seideman. Nonadiabatic laser-induced alignment of iodobenzene molecules. *Phys. Rev. A*, **70**:063410, (2004).

[83] D. E. Goldberg. *Genetic Algorithms in Search, Optimization and Machine Learning.* Addison-Wesley, Reading, Massachusetts, 1989.

[84] I. T. Jolliffe. *Principal Component Analysis.* Springer, New York City, NY, 2002.

[85] J. L. White, B. J. Pearson, and P. H. Bucksbaum. Extracting quantum dynamics from genetic learning algorithms through principal control analysis. *J. Phys. B*, **37**:L399, (2004).

[86] For our experimental parameters, the correlation matrix normalizes the data according to the standard deviations of each of the parameters. When the parameters are identical in type, the covariance matrix ($C_{i,j} = \langle\delta_i\delta_j\rangle - \langle\delta_i\rangle\langle\delta_j\rangle$) suffices. With our time domain parameterization, however, the correlation matrix is employed.

[87] M. F. Kling, Ch. Siedschlag, A. J. Verhoef, J. I. Khan, M. Schultze, Th. Uphues, Y. Ni, M. Uiberacker, M. Drescher, F. Krausz, and M. J. J. Vrakking. Control of electron localization in molecular dissociation. *Science*, **312**:246, (2006).

[88] G. L. Kamta and A. D. Bandrauk. Nonsymmetric molecules driven by intense few-cycle laser pulses: Phase and orientation dependence of enhanced ionization. *Phys. Rev. A*, **76**:053409, (2007).

[89] H. G. Muller, P. H. Bucksbaum, D. W. Schumacher, and A. Zavriyev. Above-threshold ionisation with a two-colour laser field. *J. Phys. B*, **23**:2761, (1990).

[90] B. Sheehy, B. Walker, and L. F. DiMauro. Phase control in the two-color photodissociations of HD^+. *Phys. Rev. Lett.*, **74**:4799, (1995).

[91] H. Ohmura, N. Saito, and M. Tachiya. Selective ionization of oriented nonpolar molecules with asymmetric structure by phase-controlled two-color laser fields. *Phys. Rev. Lett.*, **96**:173001, (2006).

[92] T. Zuo, A. D. Bandrauk, M. Ivanov, and P. B. Corkum. Control of high-order harmonic generation in strong laser fields. *Phys. Rev. A*, **51**:3991, (1995).

[93] M. J. J. Vrakking and S. Stolte. Coherent control of molecular orientation. *Chem. Phys. Lett.*, **271**:209, (1997).

[94] M. Machholm and N. E. Henriksen. Field-free orientation of molecules. *Phys. Rev. Lett.*, **87**:193001, (2001).

[95] N. Levasseur, Ph. Millie, P. Archirel, and B. Levy. Bond formation between positively charged species. Non-adiabatic analysis and valence-bond model in the CO^{2+} case. *Chemical Physics*, **153**:387, (1991).

[96] E. W. Thulstrup and A. Andersen. Configuration interaction studies of bound, low-lying states of N_2^-, N_2, N_2^+, and N_2^{2+}. *J. Phys. B*, **8**:965, (1975).

[97] P. M. W. Gill and L. Radom. A rationalization of unusually late transition structures for dication fragments. *Chem. Phys. Lett.*, **136**:294, (1987).

[98] G. Handke, F. Tarantelli, and L. S. Cederbaum. Triple ionization of carbon monoxide. *Phys. Rev. Lett.*, **76**:896, (1996).

[99] A. D. Bandrauk, G. M. Djamaladdin, and K. Morokuma. Electronic states of the triply charged molecular ion N_2^{3+} and laser-induced Coulomb explosion. *Phys. Rev. A*, **59**:4309, (1999).

[100] D. W. Schumacher, F. Weihe, H. G. Muller, and P. H. Bucksbaum. Phase dependence of intense field ionization: A study using two colors. *Phys. Rev. Lett.*, **73**:1344, (1994).

[101] C. Guo. Holding molecular dications together in strong laser fields. *Phys. Rev. A*, **73**:041401, (2006).

[102] T. Vogt and R. R. Jones. (unpublished) calculations of field-free orientation in co and hbr. 2007.

[103] T. Kanai and H. Sakai. Numerical simulations of molecular orientation using strong, nonresonant, two-color laser fields. *J. Chem. Phys.*, **115**:5492, (2001).

[104] D. Pavicic, K. F. Lee, D. M. Rayner, P. B. Corkum, and D. M. Villeneuve. Direct measurement of the angular dependence of ionization for N_2, O_2, and CO_2 in intense laser fields. *Phys. Rev. Lett.*, **98**:243001, (2007).

[105] R. Torres, N. Kajumba, J. G. Underwood, J. S. Robinson, S. Baker, J. W. G. Tisch, R. de Nalda, W. A. Bryan, R. Velotta, C. Altucci, I. C. E. Turcu, and J. P. Marangos. Probing orbital structure of polyatomic molecules by high-order harmonic generation. *Phys. Rev. Lett.*, **98**:203007, (2007).

[106] J. Levesque, Y. Mairesse, N. Dudovich, H. Pepin, J. Kieffer, P. B. Corkum, and D. M. Villeneuve. Polarization state of high-order harmonic emission from aligned molecules. *Phys. Rev. Lett.*, **99**:243001, (2007).

[107] H. Ohmura and M. Tachiya. Robust quantum control of molecular tunneling ionization in the space domain by phase-controlled laser fields. *Phys. Rev. A*, **77**:23408, (2008).

[108] R. Tehini and D. Sugny. Field-free molecular orientation by nonresonant and quasiresonant two-color laser pulses. *Phys. Rev. A*, **77**:23407, (2008).

[109] Y. Sugawara, A. Goban, S. Minemoto, and H. Sakai. Laser-field-free molecular orientation with combined electrostatic and rapidly-turned-off laser fields. *Phys. Rev. A*, **77**:031403, (2008).

[110] H. Rabitz, R. de Vivie-Riedle, M. Motzkus, and K. Kompa. Whither the future of controlling quantum phenomena? *Science*, **288**:824, 2000.

[111] R. N Zare. *Angular Momentum: Understanding Spatial Aspects in Chemistry and Physics*. Wiley-Interscience, 1988.

[112] CVI: Optical Components and Assemblies. Dispersion equations: Technical notes.

[113] D. P. Seccombe and T. J. Reddish. Theoretical study of space focusing in linear time-of-flight mass spectrometers. *Rev. Sci. Inst.*, **72**:1330, (2001).

[114] H. Ren, R. Ma, J. Chen, X. Li, H. Yang, and Q. Gong. Field ionization and Coulomb explosion of CO in an intense femtosecond laser field. *J. Phys. B*, **36**:2179, (2003).